TA [B] Predicting Microstructure-Creep Resistance Correlation in High Temperature Alloys over Multiple Time Scales

Final Technical Report

(Jul 13, 2013 to June 30, 2016)

Prepared By

Vikas Tomar, Ph.D.
Professor
School of Aeronautics and Astronautics
Purdue University
701 W. Stadium Ave.
West Lafayette, IN 47907-2045
Phone: 765-494-3423, 317-294-3251
Email: tomar@purdue.edu

Jian Luo, Ph.D.
Professor
Department of NanoEngineering
University of California, San Diego
9500 Gilman Drive, Mail Code 0448
La Jolla, CA 92093Phone: (858) 246-1203
Fax: (858) 534-9553
Email: jluo@ucsd.edu

Original Submission

September 21, 2016

Updated Submission

February 23, 2017

DoE Award Number: DEFE0011291

EXECUTIVE SUMMARY

DoE-NETL partnered with Purdue University to predict the creep and associated microstructure evolution of tungsten-based refractory alloys. Researchers use grain boundary (GB) diagrams, a new concept, to establish time-dependent creep resistance and associated microstructure evolution of grain boundaries/intergranular films GB/IGF controlled creep as a function of load, environment, and temperature. The goal was to conduct a systematic study that includes the development of a theoretical framework, multiscale modeling, and experimental validation using W-based body-centered-cubic alloys, doped/alloyed with one or two of the following elements: nickel, palladium, cobalt, iron, and copper—typical refractory alloys. Prior work has already established and validated a basic theory for W-based binary and ternary alloys; the study conducted under this project extended this proven work. Based on interface diagrams phase field models were developed to predict long term microstructural evolution. In order to validate the models nanoindentation creep data was used to elucidate the role played by the interface properties in predicting long term creep strength and microstructure evolution.

TABLE OF CONTENTS

NARRATIVE

The performed research had four tasks. In the following, results from each task are briefly described.

§ TASK 1. Fabrication and Characterization of Alloys

1.1 Fabrication of W-based Alloys

Binary W-based alloys, e.g. Zr-doped W, Ni-doped W, Co-doped W, Re-doped W and Cu-doped W, have been prepared by standard powder metallurgical methods, which included ball milling, cold pressing and pressureless sintering. For comparison, pure W samples were also prepared using the same route. 5 atomic percent of Zr, Ni, Co, Re and Cu was doped into W, respectively. The powder mixtures with 1 wt. % stearic acid (as the control agent) were added to tungsten carbide vial and ball milled for 6 hours. Green pellets were obtained by uniaxial pressing under a pressure of ~380 MPa for 3 minutes. Sintering was carried out at 1200°C (with the ramp rate of 5°C/min) for 5 hours purged with forming gas (Ar + 5 vol.% H_2) constantly. The ball milled powders and sintered samples were analyzed by X-ray diffraction (XRD) using a Rigaku RU-200BH (Tokyo, Japan) diffractometer operating at 40 kV and 100 mA. The crystallite sizes of ball milled powder were determined to be ~14 nm for pure W and ~16 nm for Zr-doped W according to the Scherrer equation (Fig. I-1(A) and (B)).

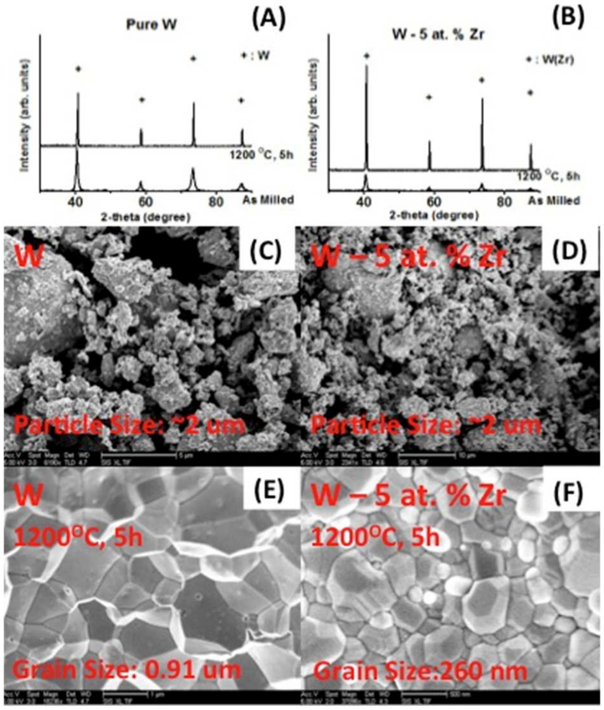

Fig. I-1: XRD patterns of ball milled powders and sintered pellets of **(A)** pure W and **(B)** Zr-doped W. SEM micrographs of the milled powders of **(C)** pure W and **(D)** Zr-doped W. **(E)** and **(F)** showed the fracture surfaces of sintered pure W and Zr-doped W pellets, respectively.

Scanning electron microscopy (SEM) images showed the characteristic morphologies of the ball milled powers in Fig. I-1(C) and (D); Strong tendency of agglomeration was occurred in ball-milled powders and the average particles are ~ 2 μm. Grain sizes of sintered pellets were determined to be 0.91 μm for pure W and 260 nm for Zr-doped W based on SEM images (Fig. I-1(E) and (F)) analyzing by a standard linear intercept method. Fig. I-2 illustrates the fracture surfaces of sintered pellets for Ni-doped W, Co-doped W, Re-doped W and Cu-doped W, respectively. The grain sizes of sintered pellets were determined to be 820 nm for Ni-doped W, 600 nm for Co-doped W, 210 nm for Re-doped W and 2.2 μm for Cu-doped W, respectively.

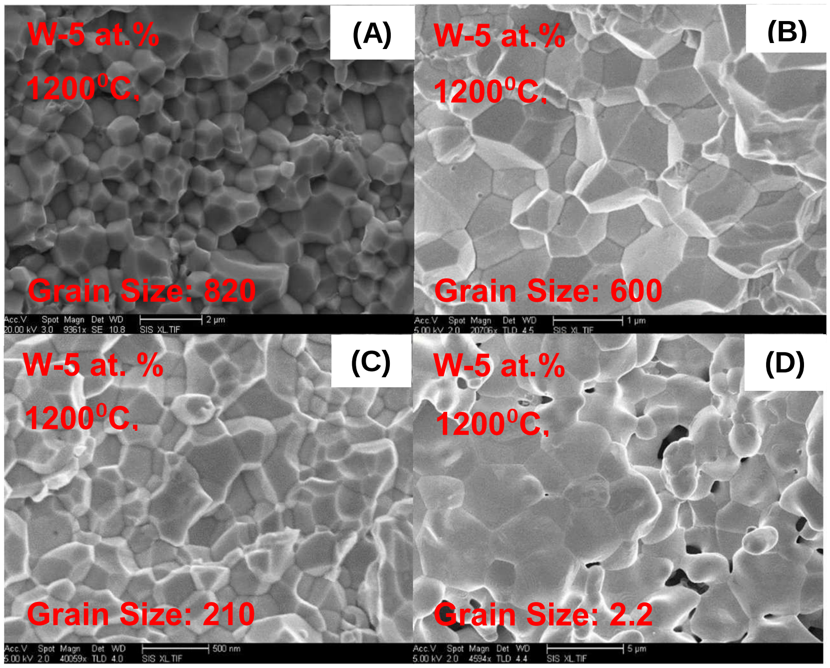

Fig. I-2: SEM micrographs of fractured surfaces of sintered pellets for **(A)** Ni-doped W, **(B)** Co-doped W, **(C)** Re-doped W and **(D)** Cu-doped W.

W-based binary and ternary alloys, e.g. W-Mn, W-Ni, W-Ti, W-Re and W-Re-Ni alloys was also prepared by the spark plasma sintering (SPS). The fractured surfaces of these W-based alloys were shown in Fig. I-3. The average grain size for the SPSed W-Mn, W-Ni, W-Ti, W-Re and W-Re-Ni alloys is 583nm, 410nm, 221nm, 180nm and 209nm, respectively.

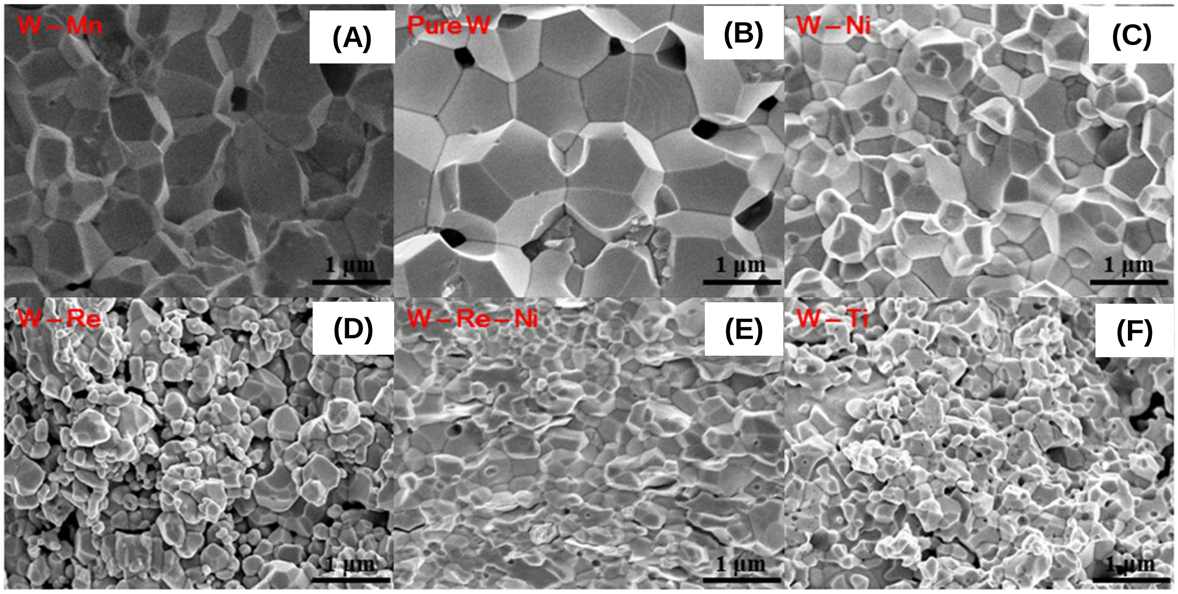

Fig. I-3: SEM micrographs showing the fracture surfaces of SPSed pellets for **(A)** Mn-doped W, **(B)** pure W, **(C)** Ni-doped W, **(D)** Re-doped W, **(E)** Re and Ni-codoped W and **(F)** Ti-doped W.

To investigate the dopant effect on the sintering ability and grain growth inhibiting, we selected Nb as a new doping element. W-5 at.% Nb was prepared via the identical processing route, e.g. high-energy ball milling and SPS. The mean grain size for W-5 at.% Nb is about 217 nm. The fracture surface and grain morphology can be found shown in Fig. I-4.

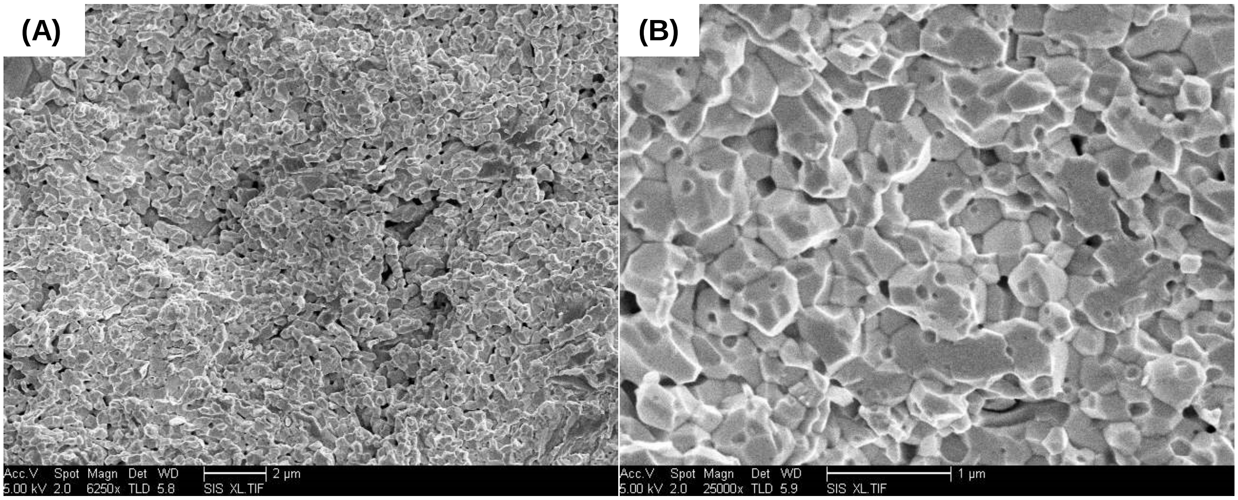

Figure I-4: SEM micrographs of fracture surfaces of SPSed pellets for Nb-doped W. The concentration of Nb is ~ 5 at.%.

To investigate the thermal stability of the W binary alloys, annealing was performed for pure W, as well as 5 at.% Zr and 10 at.% Zr doped W specimens at 1200 ℃ for 5h. The SEM images of the fractured surfaces in Fig. I-5 shows that Zr doping in W could inhibit the grain growth; the more Zr doped, the smaller grain size is. This set of specimens and SEM images were provided to Purdue team for creep testing as well as microstructure-dependent modeling of both sintering and creep. Annealing experiments for the same materials were also performed at 1200 ℃ for extended 10h. The SEM images of the fractured surfaces are shown in the Fig. I-5. It shows the consistent trend that of grain growth was suppressed by doping more Zr. No obvious change of fracture surface for pure W and 5 at.% Zr doped W specimens was found. However, the grain boundary faceting vanished in 10 at.% Zr doped W specimen after extended annealing duration as shown in Fig. I-5(F).

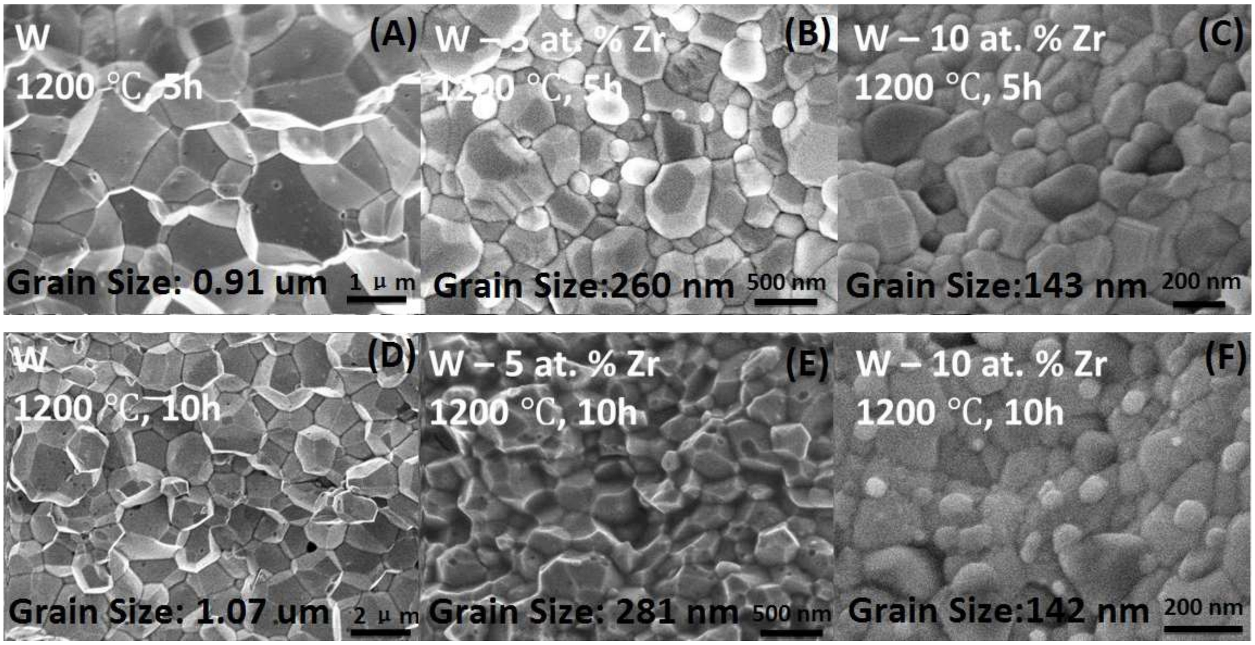

Figure I-5: (A-C) SEM images of fractured surfaces for tungsten doped 0, 5, and 10 atomic percent of zirconium, sintered at 1200 ℃ for 5h. **(D-F)** SEM images of fractured surfaces for tungsten doped 0, 5, and 10 atomic percent of zirconium, sintered at 1200 ℃ for 10h.

To further reveal the microstructure in Nb-doped W with enhanced density after sintering, transmission electron microscopy (TEM) characterization was conducted. We used dual beam FIB/SEM system to prepare the TEM sample from a bulk W-10 at.%Nb specimen as shown in Fig. I-6.

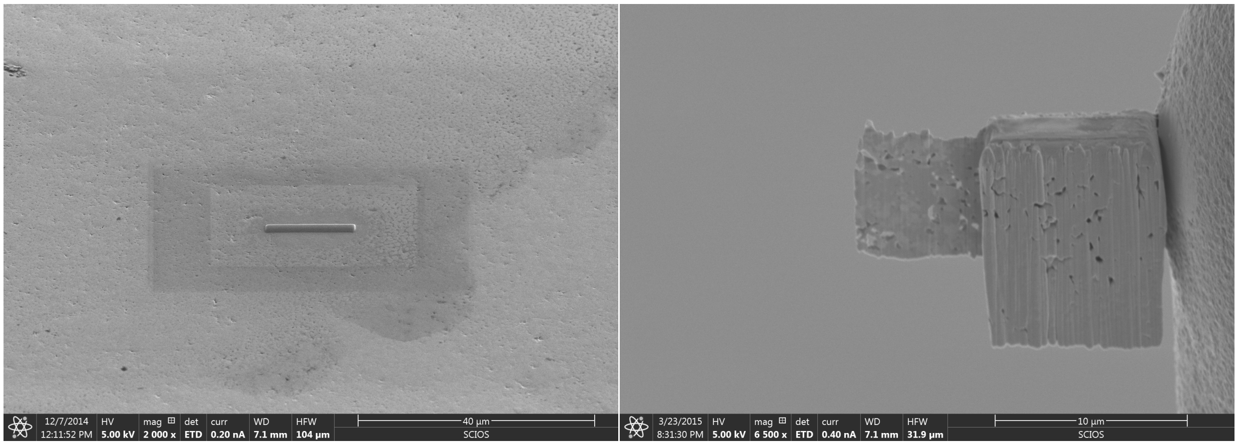

Figure I-6: TEM specimen of W-10 at.%Nb prepared by dual beam FIB/SEM system

The microstructure of W-10 at.%Nb was obtained by TEM studies as shown in Fig. I-7. Both crystalline regions and amorphous regions were observed in this specimen as depicted by Fig. I-7(A). The amorphous regions (indicated by yellow arrows) were homogeneously distributed among the crystalline grains. Fig. I-7(B) shows the morphology of the grains, of which the amorphous grains have curved boundaries. Fig. I-7(C) shows the boundary condition, in which the amorphous grain abutted on the crystalline grain. The diffraction pattern obtained from the circled area d in (B) confirming the presence of crystalline phase, whereas diffraction pattern obtained from circled area e in (B) indicating the presence of amorphous phase.

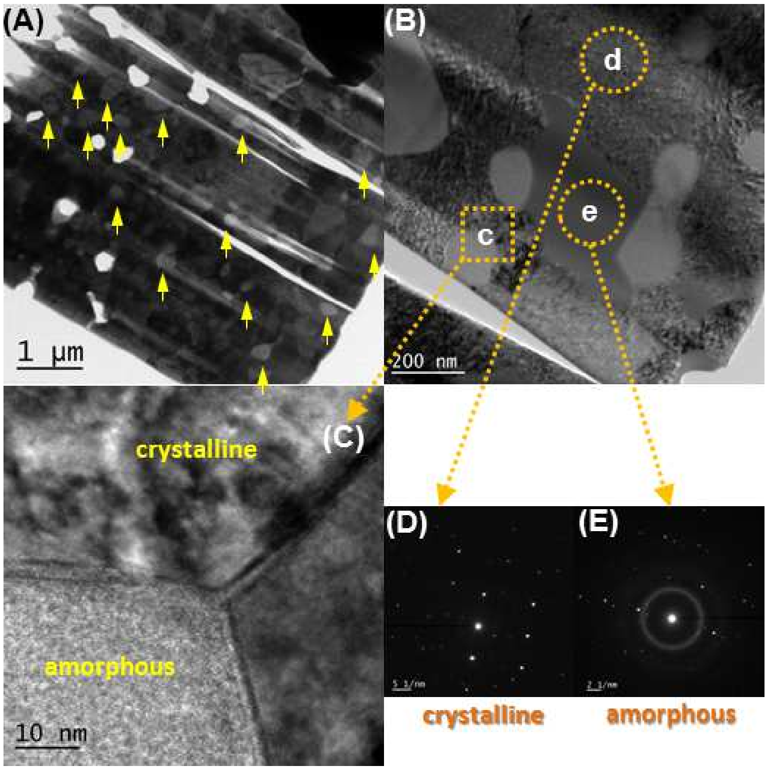

Figure I-7: Microstructure of W-10 at.% Nb specimen sintered via SPS at 1200 °C for 5 min. **(A)** TEM image at low magnification with yellow arrows showing the amorphous grains; **(B)** TEM image at high magnification; **(C)** TEM image obtained from the framed area in (B); **(D)** diffraction pattern obtained from the circled area d in (B); and **(E)** diffraction pattern obtained from circled area e in (B).

Table I-1 Relative density, grain size and hardness of pure W and doped W consolidated by spark plasma sintering

Composition	Relative Density	Grain Size (nm)	Hardness (HRC)
Pure W	**90± 1%**	**810 ± 230**	**42**
W – 5 at. % Ni	**95%**	**440±140**	**49**
W – 5 at. % Ti	**80%**	**145±40**	**42.5**
W – 5 at. % Mn	**85%**	**570±200**	**24.5**
W – 5 at. % Re	**84%**	**132±41**	**33**
W – 5 at. % Nb	**90%**	**202±64**	**44**

Table I-1 summarized the major binary W alloys with various doping elements in this project. It can be found that Ni assisted the sintering, and enabled the highest density. However, the grain size was about 440 ± 140 nm. Doping Nb enabled both relative high density and small grain size. Ti and Re have strong effect to suppress grain growth. However, the W-Ti and W-Re alloys have low density indicating that Ti and Re did not assist the sintering efficiently. Mn neither assisted the sintering nor suppressed the grain growth. We also measured hardness of these binary W alloys. W-Ni has the highest hardness, which is probably because of the density. W-Nb and W-Ti exhibited similar hardness, though the grain size and density are different. This indicated that the density and grain size both affect the hardness of the material.

1.2 Fabrication of nanocrystalline Ni foils

Nanocrystalline Ni foils were prepared following a pulsed electrodeposition procedure Elsherik and Erb (1995) with minor modifications. Prior to electrodeposition, the Cu substrates and Pt counter electrode were ground with SiC grinding papers (up to 800 grits), final polishing was performed by 1.0 μm Al_2O_3 colloidal suspensions and finally cleaned in acetone. A bath composed of $NiSO_4·6H_2O$ (300 g/L), $NiCl_2·6H_2O$ (45 g/L) and H_3BO_3 (45 g/L), with additives of saccharine (5 g/L) and sodium lauryl sulfonate (0.25 g/L) was used for electrodeposition. Each deposition was conducted for 30 min with continuous stirring while the bath temperature was maintained at 65 ± 1°C. The effective current density was kept at 0.1 A/cm^2 (by using an "on" time of 5 ms with the current density of 0.4 A/cm^2, followed by an "off" time of 15 ms, periodically).

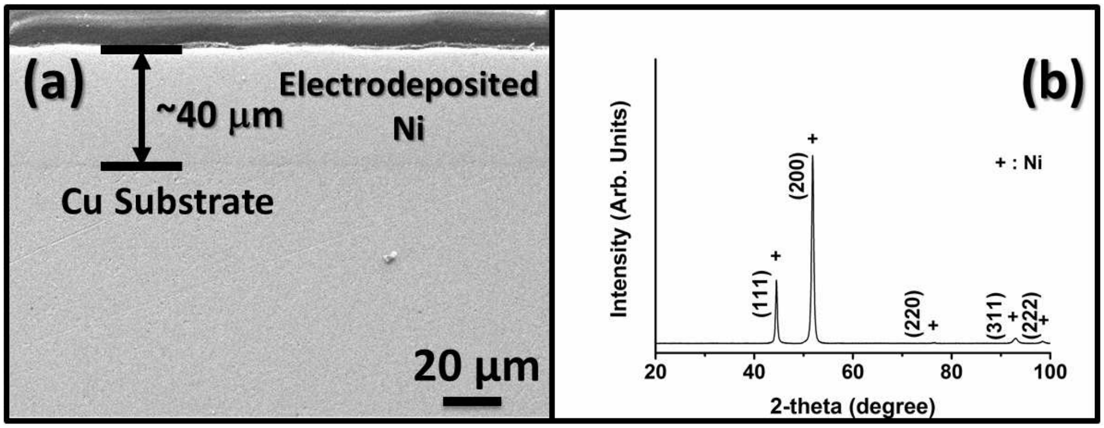

Figure I-8: (A) Cross-sectional SEM micrograph of electrodeposited Ni on a Cu substrate. **(B)** XRD pattern obtained on the electrodeposited Ni foil.

The electrodeposited Ni layer has a thickness of ~40 μm as shown in Fig. I-8(A). The as-deposited specimens were characterized by XRD. A NIST LaB_6 standard specimen was used to correct the effect of instrumental line broadening. The XRD pattern in Fig. I-8(B) showed that only fcc Ni phase existed (excluded impurity phases). The grain size of the as-deposited Ni foil was calculated to be ~18 nm based on XRD peak broadening using the Scherrer Equation.

After electrodeposition, Cu substrates were then dissolved in an aqueous solution containing CrO_3 (250 g/L) and sulfuric acid (15 cc/L) to obtain free-standing nanocrystalline Ni foils for further mechanical tests performed at Purdue University.

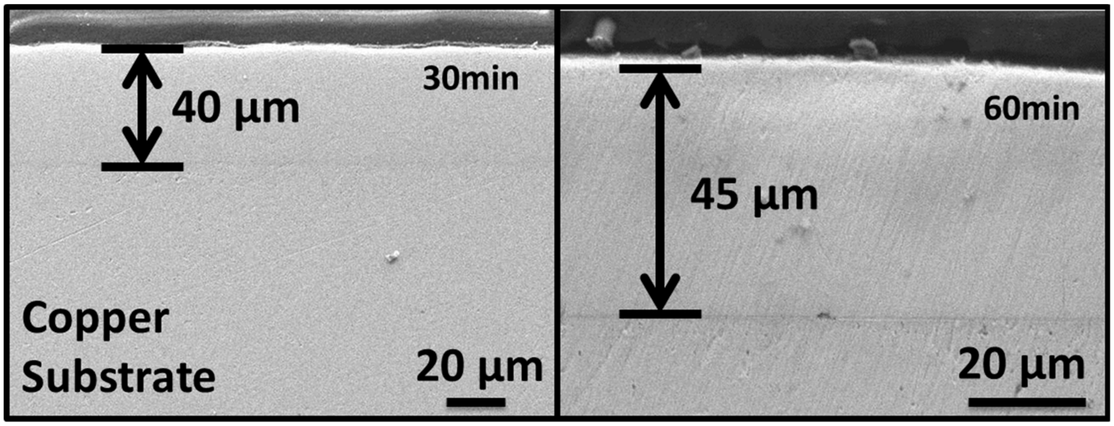

Figure I-9: (A) Cross-sectional SEM micrographs of electrodeposited Ni on Cu substrates; 30 minutes' deposition resulted in a Ni layer of 40 μm. and **(B)** 60 minutes' deposition resulted in a Ni layer of 45 μm

More efforts were devoted to fabricate thicker Ni foils for mechanical tests by optimizing parameters. It was found that the desposition rate slows down dramatically and virtually stops after 30 minutes, which was demonstrated in Fig. I-9. We are currently exploring several possibilities to form new synthesis stragetgies. One possibility is the depletion of Ni^{2+} concentrataion, which slows down the reaction rates. This can be solved by using a flesh bath. Another possibility is surface poisioning, which can be remidated by developing an effective cleaning procedure.

We have successfully prepared thicker nanocrystalline Ni foils (up to 100 μm) after several trials on the different deposition conditions. We found that the key factor is to have sufficient amount of the electrolyte for the electro-deposition. We used 1 L electrolyte (400 ml in prior experiments) and conducted the electrodeposition for 2 hours. Fig. I-10 shows the cross-section of an electrodeposited specimen; the thickness of the deposited layer is around 100 μm.

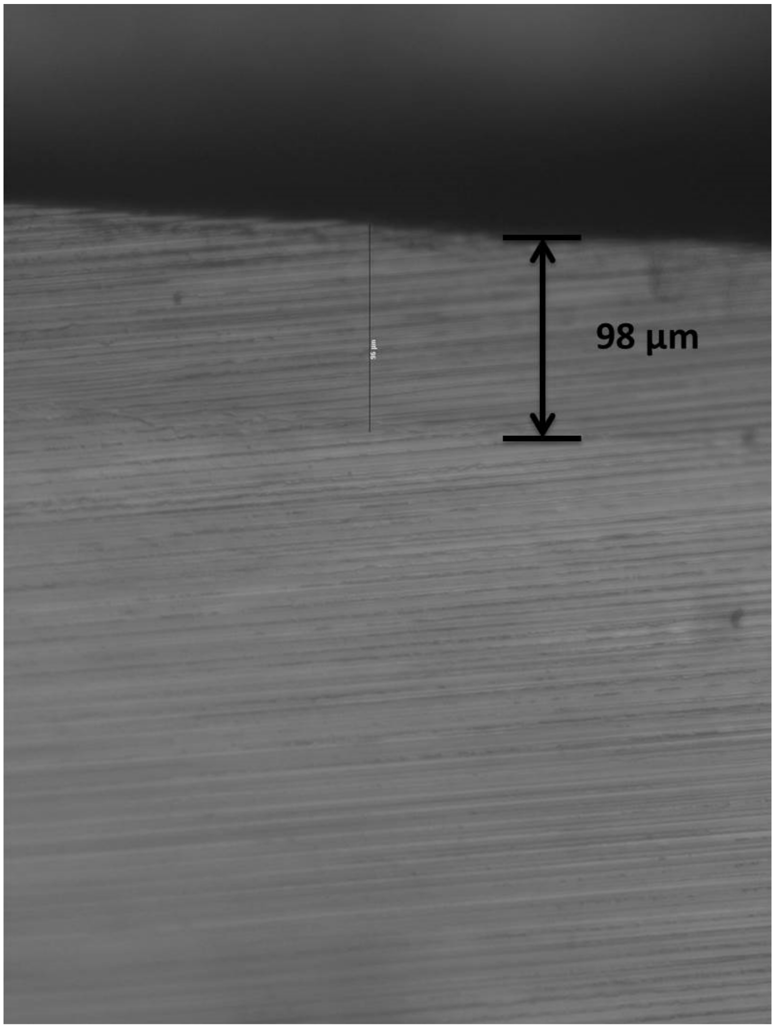

Figure I-10: An optical micrograph of the cross section of an electrodeposited Ni foil that is about 100 µm thick

§TASK 2 – Experiments on Control Samples to Obtain Validating Dataset via New and Unique Creep Testing Capability at Purdue

The task 2.1 focuses on the experimental setup shown in Fig. II.1. Using this setup the indenter tip can be heated to up to 750 ° C. The heated tip can be used to measure temperature dependent elastic and creep properties of the control samples during uniaxial indentation up to 750 °C. It has been shown that indentation creep measurements are strongly correlated to the material bulk creep properties at significantly higher temperatures approaching 1500 °C and above, Li and Ngan (2004; Milhans et al. (2010). Accordingly, the nano- and microindentation creep resistance increase is directly correlated to the bulk creep strength increase of a material. An added advantage of nano- and micron scale creep measurements is the ability to quantify the effect of microstructure tailoring on the overall increase in material performance. As shown in Fig. II.1 (c), a nanoscale resolution surface profile of the indented surfaces can be created along with the quantitative measurements to understand the effect of specific microstructural features on the corresponding elastic creep properties. This setup has recently been used to explore multiscale (nano- and microscale) elastic and creep properties as a function of temperature up to 500 ° C of polymer derived SiCO ceramics, Gan and Tomar (2010). Students are getting trained to perform initial measurements currently.

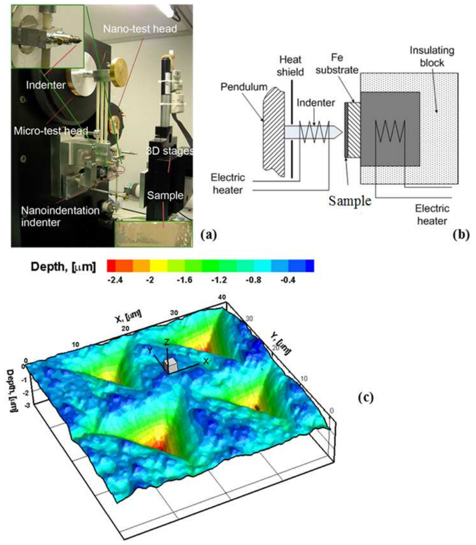

Fig. II.1: Setup of experiments showing **(a)** instrument, **(b)** schematic, and **(c)** a scan of a sample analyzed for nano- and microscale indentation creep properties

Since the control samples have now just been obtained, the experiments on the samples have just begun. The Ni samples in this case are obtained from first electrodepositing Ni on Cu substrate and then dissolving Cu substrate. The samples in this case are of 40 µm thickness and both sides of the samples have mirror like surface finishing. Fig. 2 depicts the sample preparation process and actual sample dimensions. Samples with approximately 1cm X 1cm in dimension were then cut from the original samples and used for thermo-mechanical characterization experiments.

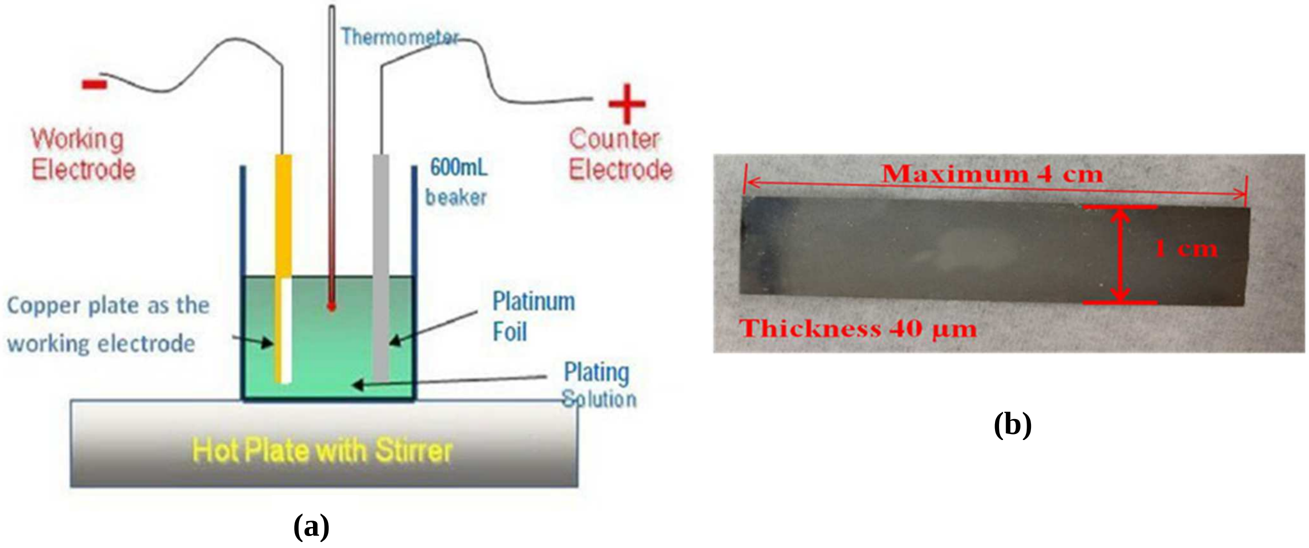

(a)

(b)

Fig. II.2. (a) Sample Preparation Technique, **(b)** Original Sample Dimensions

All tests were performed using a multi-module mechanical tester (Micro Materials Ltd., UK) shown in Fig. 3. Fig. 3 (b) depicts the setup explaining the approach for performing high temperature indentation.

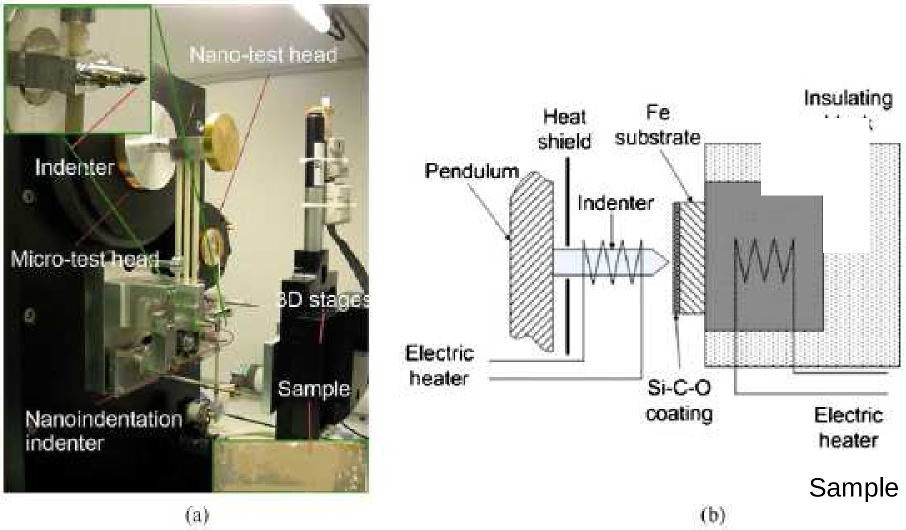

(a)

(b)

Fig. II.3. Experimental Set-up **(a)** Micro and Nano indentation Setup, **(b)** Schematic for high temperature indentation approach

Both the sample and the indenter tip were heated to the required testing temperature which was closely monitored using thermocouples. After reaching the desired temperature the set-up is kept inactive for 2 hours in order to achieve thermal stability. The remaining parts of setup are separated by heat shield in order to maintain them at room temperature. The tests were performed at different temperatures ranging from room temperature to 750 ◦C. In both cases, Berkovich diamond indenter having tip radius approximately 20 nm and 200 nm has been used for nanoindentation and microindentation, respectively. During the tests, the samples were mounted on the indentation stage using glue. The indenter approached the sample in its thickness direction. Indentation locations were selected randomly on sample surfaces. For single data, the tests were performed at different location selected as a 3 by 3 matrix with equal longitudinal and transverse spacing between each indentation spot. The indentation depths and maximum indentation load were chosen to minimize the effect of measurement drift that usually occurs in indentation tests if the depth is too small. The depth calibration and the area function computation has been done for each temperatures using Tungsten and fused silica as reference sample in case of micro-indentation & nano-indentation, respectively. The sample is first loaded from zero to a maximum loading, maximum load is held for 500 s & then the unloading happens. The reduced modulus of the material is calculated from the slope of the unloading curve. Creep characterization data is collected from the dwell period so as to observe the change in depth at constant load. Depending on dwell period, the creep properties changes as the system undergoes transient to steady state creep. It has been explored that 500 s is good enough to achieve steady state creep and yields quite good prediction of the material behavior. During unloading, when the load reaches 10% of the maximum load, the load is kept constant for 60 sec. in order to estimate thermal drift correction and compute the actual creep displacement.

Figure 4(a) represents the typical load displacement curve for an indentation experiment done at room temperature with 500 mN maximum load. In this case, the sample is loaded upto the maximum load, the maximum load is hold for around 500 seconds and then unloading happens. The reduced young’s modulus in this case is computed from the slope of the unloading curve. In this case, the obtained hardness of the material is 374 MPa and the reduced young’s modulus is 7.85 GPa. Creep data is abstracted from the maximum load holding period. Figure 4 (b) shows the extracted creep curve.

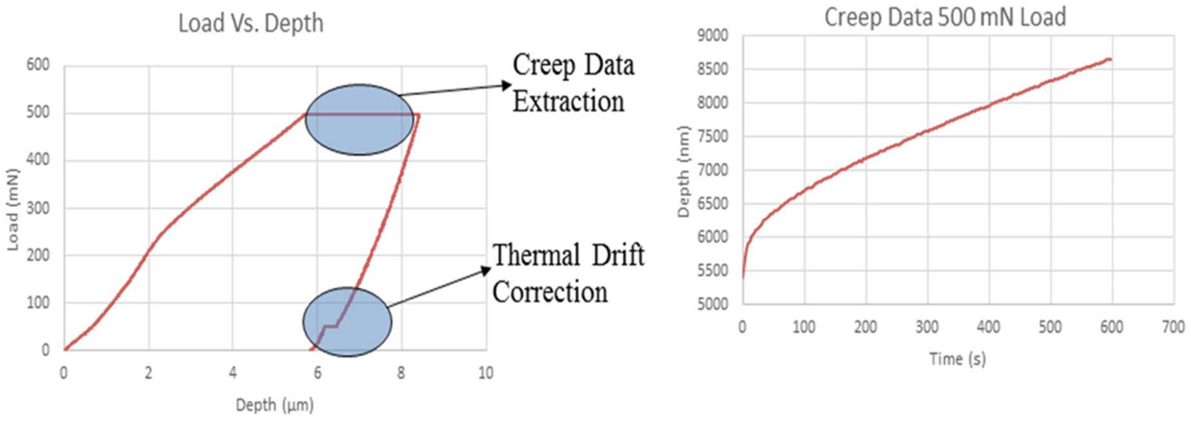

(a) **(b)**

Fig. II.4. **(a)** Typical Indentation Curve, **(b)** Creep Data Extraction

During this hold period, the depth of indentation increases with time while the load remains constant. However, the maximum penetration depth here is 8 µm, which is more than the 10% of the sample thickness. Hence, substrate effect may come into picture. In order to eliminate substrate effect, more experiments at lower load has to be done. Also experiments at high temperature need to be executed. From the extracted creep data the strain rate vs. stress curve has been plotted in logarithmic scale and the creep exponent has been computed. The same has been shown in Fig. 5. The estimated creep exponent is 1 here, which indicates that the creep here is governed by vacancy diffusion mechanism.

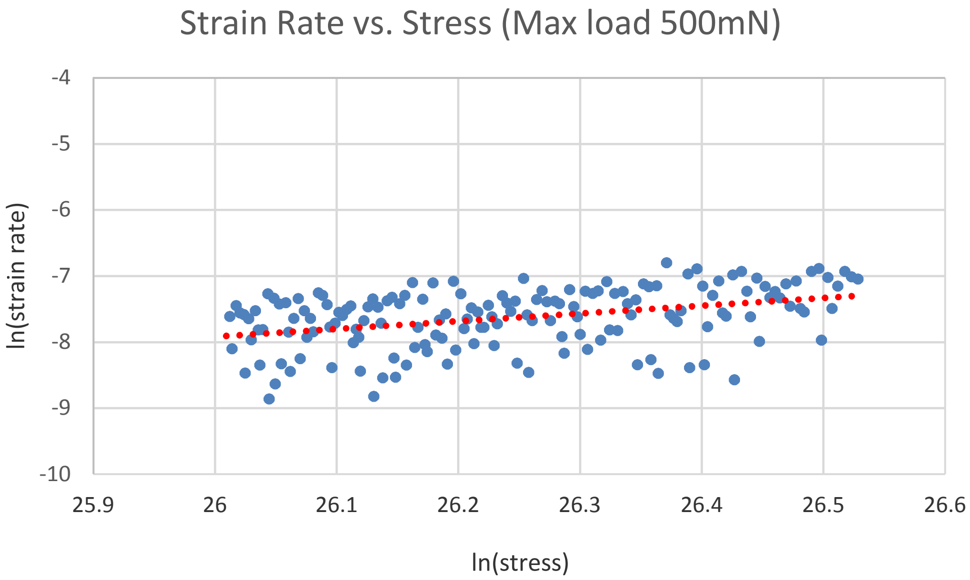

Fig. II.5. (a). Strain Rate vs. Stress during Maximum load holding period (log-log scale)

The data obtained from the current experiment needs validation after correcting the substrate effects. Also the SEM images of the samples needs to be captured to observe the deformation mechanism at microstructure level. More nanoindentation experiments at different temperature range have to be done for proper prediction of the properties. The sample property measurement setup is complete. Based on the new samples that we have gotten, measurements are ongoing.

The measurements include nanoindentation based predictions. However, we cannot observe the samples when the measurements are going on. This results in a lot of guesses regarding the mechanisms behind samples behavior predictions. To alleviate this a new setup was designed. A request was made to DoE-NETL-UCR program regarding the use of funds to purchase a part of setup. The request was approved. The equipment is expected to be installed and working in September 2015. We will be able to observe grain boundary chemistry during deformation using the new setup. Meanwhile, to complete the milestone-3, the controlled creep data was collected.

In the calculation of the reduced modulus and the hardness, the thermal drift was first compensated using the data given by Figure II.4 (c). Then the creep effect was also removed by using the correct elastic stiffness. After correcting for both creep and thermal drift, the reduced young’s modulus of the samples as a function of temperature under different loads and loading & unloading rates are shown in the Figure II.6 (a). Through the results, it is shown that reduced modulus will decrease with temperature. Also the hardness as a function of temperature under different loads and loading & unloading rates are shown in the Figure II.6 (b). And the values of hardness show same trend as reduce modulus, which decrease with the temperature increase. In addition, hardness reduces with increase in the peak indentation load, signifying strain softening of the material. Apart from the influence of strain softening, material pile-up around the indent and indentation creep can also contribute to indentation hardness behavior observed in the present work.

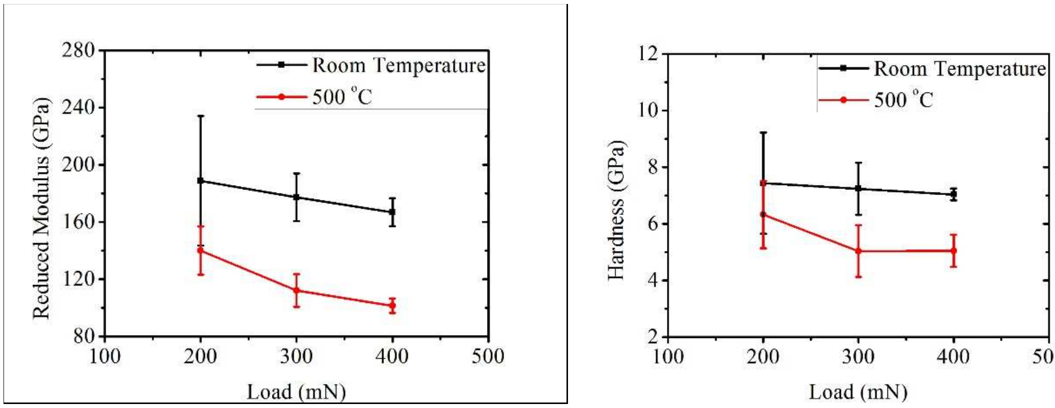

(a) (b)

Figure II.6. Reduced modulus and hardness of the samples as a function of temperature under different loads. (a) Reduced modulus, (b) hardness.

The creep curve of 500s dwell time at room temperature and 500 °C are shown in the Figure II.7.

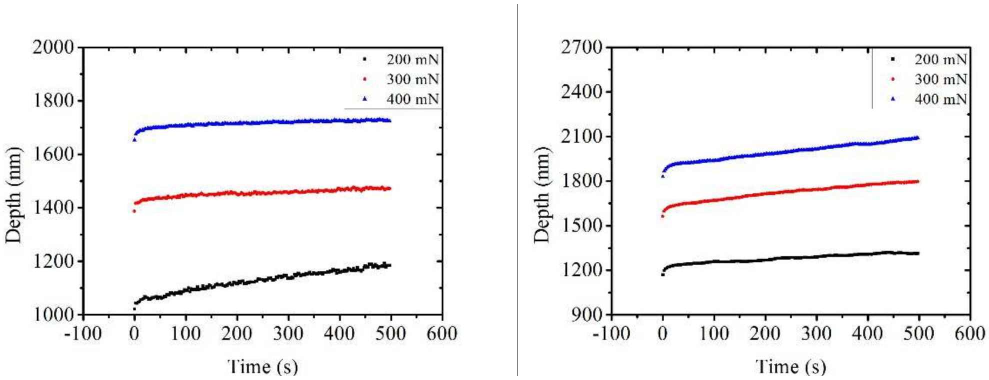

Figure II.7. Creep curve of 500s dwell (a) Room Temperature, (b) 500 °C

§TASK 3: A New Theoretical Framework to Characterize GB Segregation

We extended bulk CALPHAD (Calculation of Phase Diagram) methods to compute "GB diagrams" for binary alloys. The basic feasibility for computing such GB diagram has been demonstrated for binary refractory alloys by the co-PI Luo's group and the correctness of this model and computation results has been verified by direct high-resolution transmission electron microscopy (HRTEM) and Auger electron spectroscopy (AES) measurements as well as indirect probing of GB diffusion via designed sintering experiments Gupta et al. (2007b; Shi and Luo (2009; Shi and Luo (2011). As schematically illustrated in Fig. III-1, a subsolidus quasi-liquid IGF can be thermodynamically stable under solidus temperature if:

$$\Delta G_{\text{amorph.}} \cdot h < (-\Delta\gamma) \equiv \gamma_{gb}^{(0)} - 2\gamma_{cl} \qquad (1)$$

where h is the film thickness, $\gamma_{\text{gb}}^{(0)}$ is the excess energy of a random GB without adsorption, and γ_{cl} is the crystal-liquid interfacial energy Luo and Shi (2008). The volumetric free energy to form an undercooled liquid ($\Delta G_{\text{amorph.}}$) of a binary alloy can be quantified using the bulk CalPhaD methods. A thermodynamic variable λ is defined to represent the thermodynamic tendency of GB to disorder:

$$\lambda \equiv Max\{-\Delta\gamma / \Delta G_{amorph}\} \qquad (2)$$

The actual "equilibrium" thickness of IGF h_{EQ} is related to λ by $h_{\text{EQ}} \approx \xi \cdot \ln(\lambda/\xi)$ where ξ is the coherent length Luo and Shi (2008). The "GB solidus temperature" (T_{GBS}) can then be estimated by $h_{\text{EQ}}(T_{\text{GBS}}) \approx 0$ or $\lambda(T_{\text{GBS}}) = \xi \approx 0.5\text{-}1$ nm .

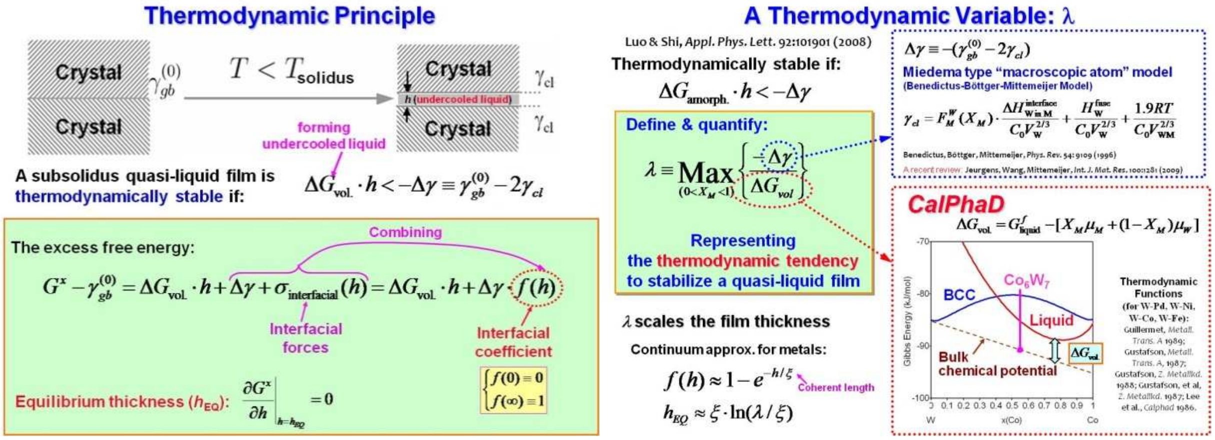

Fig. III-1: Schematic illustration of the proposed thermodynamic model.

We've developed a MATLAB code and applied it to calculate the GB λ-diagram for binary systems. The Mo-Ni GB phase diagram for a certain composition and temperature window (0-5 % Ni; 1200-1450 ^{o}C) is calculated and is shown in Fig. III-2(A). Fig. 2(B) shows the GB diffusivity map of the same temperature-composition region (Shi and Luo 2011). The consistency between the model calculations (Fig. 2(A)) and the experiment measurement (Fig. 2(B)) indicates that our λ model is able to predict the trends in GB diffusivities, thereby Coble creep rate.

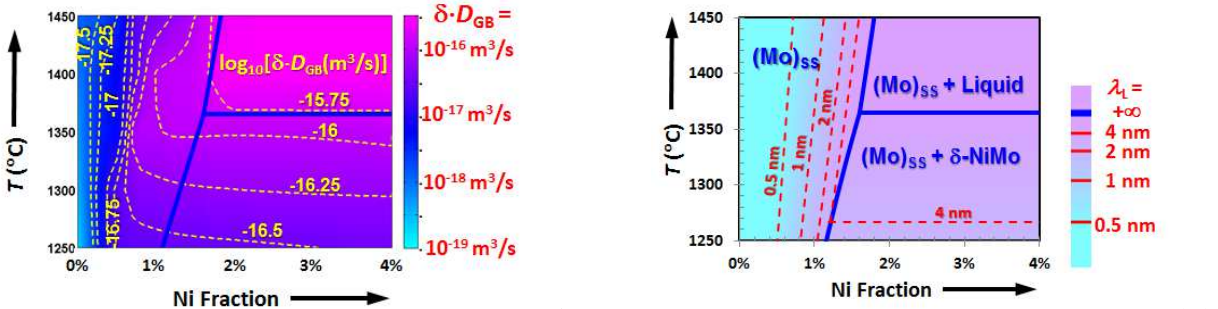

(A) **(B)**

Fig. III-2: (A) Computed GB λ-diagram *vs.* **(B)** measured GB diffusivity map for Ni-doped Mo [reprinted from Shi and Luo (2011)].

We can also use the Wynblatt-Chatain model [Wynblatt and Chatain (2006)] to estimate the effect of alloying on reducing GB energies and stabilizing nanocrystalline alloys. The following expression is derived by simplifying the Wynblatt-Chatain formulism [Wynblatt and Chatain (2006)] for $J_{\max} = 1$:

$$\gamma_{GB} = \min \left\{ \begin{array}{l} (p-1) z_v N \left[2X_{GB}^1 (1 - X_{GB}^1)\omega + X_{GB}^1 e_{BB} + (1 - X_{GB}^1) e_{AA} \right] - 2N \sum_i^{+\infty} \left[X_{GB}^i \Delta E_{els}^i \right] \\ +2N\omega \sum_i^{+\infty} \left[-z (X_{GB}^i - X_C)^2 + z_v (X_{GB}^i - X_{GB}^{i+1})^2 \right] + 2NkT \sum_i^{+\infty} \left[X_{GB}^i \ln\left(\frac{X_{GB}^i}{X_C}\right) + (1 - X_{GB}^i) \ln\left(\frac{1-X_{GB}^i}{1-X_C}\right) \right] \end{array} \right\} \quad (3)$$

where X_{GB}^i is the composition in the i-th layer near the GB core, e_{AA}, e_{BB}, and e_{AB} are bonding energies, $\omega [\equiv e_{AB} - 0.5(e_{AA} + e_{BB})]$ is the pair-interaction parameter, z is the total coordinate number (z = 8 for BCC), z_v is the coordination number above the plane, p (the fraction of reconnected bonds) is set to be 5/6 to represent a "general GB" so that the GB energy is 1/3 of the surface energy for a pure element, N is the number of the lattice sites per unit area, k is Boltzmann constant and T is temperature. ΔE_{els}^i is the elastic energy in the i-th layer which are assessed by the Friedel model Wynblatt and Chatain (2006). The equilibrium GB adsorption profile can be obtained by minimizing Eq. (3) $(\partial \gamma_{GB} / \partial X_{GB}^i = 0)$, leading to a McLean type adsorption equation for each layer:

$$\frac{X_{GB}^i}{1 - X_{GB}^i} = \frac{X_C}{1 - X_C} \exp\left(-\frac{\Delta H_{seg}^i}{RT}\right) \quad (4)$$

Here, $\Delta H_{seg}^{\mathrm{i}}$ is adsorption enthalpy of the i-th layer. Eq. (3) and (4), along with the adsorption profile $(X_{GB}^i)_{i = 1, 2, \ldots}$ that minimizes Eq. (3), can be solved efficiently via an iterative method.

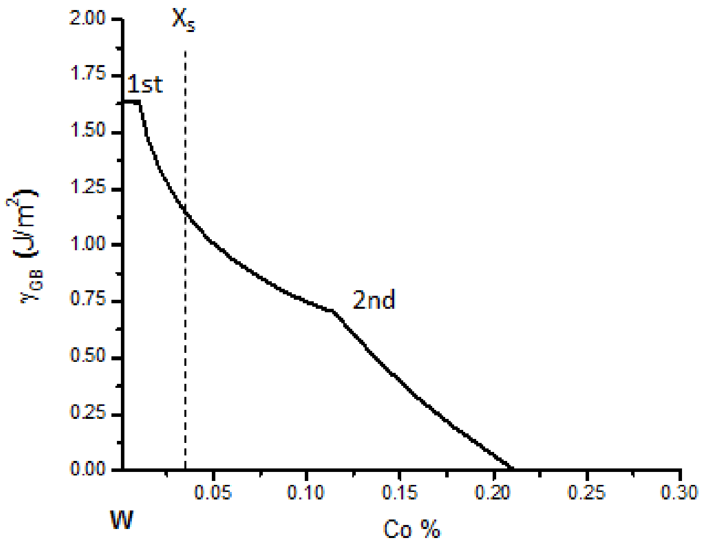

Fig. III-3: Computed grain boundary energy *vs.* Co concentration for W-Co alloys at 973 K.

The GB excess of solute is given by: $\Gamma \approx 2N\sum_i (X_{GB}^i - X_C)$. With this model, we are able to evaluate the effects of segregation on reducing GB energies and stabilizing nanocrystalline alloys.

Fig. III-3 shows computed grain boundary energies *vs.* the atomic fraction of an alloying element (Co as an example) for W-Co alloys. Our preliminary calculations show that adding Co can effectively reduce the grain boundary energy of W and help stabilize the grain size. Theoretically, the alloy will exhibit an "equilibrium" grain size once the effective grain boundary is reduced to zero. Practically, the effect of alloying is limited by the solid solubility (*X*s), beyond which precipitation will occur. Yet, if the precipitation can be inhibited (kinetically), grain boundary energy can be further reduced in the super-saturated region. We also find a discontinuity in the first derivatives of the grain boundary energy, indicating the possible existence of a grain boundary "phase" transition in the super-saturated region. Such computations will help us to select the alloying elements and processing recipes to fabricate stable nanocrystalline alloys in § TASK 1.

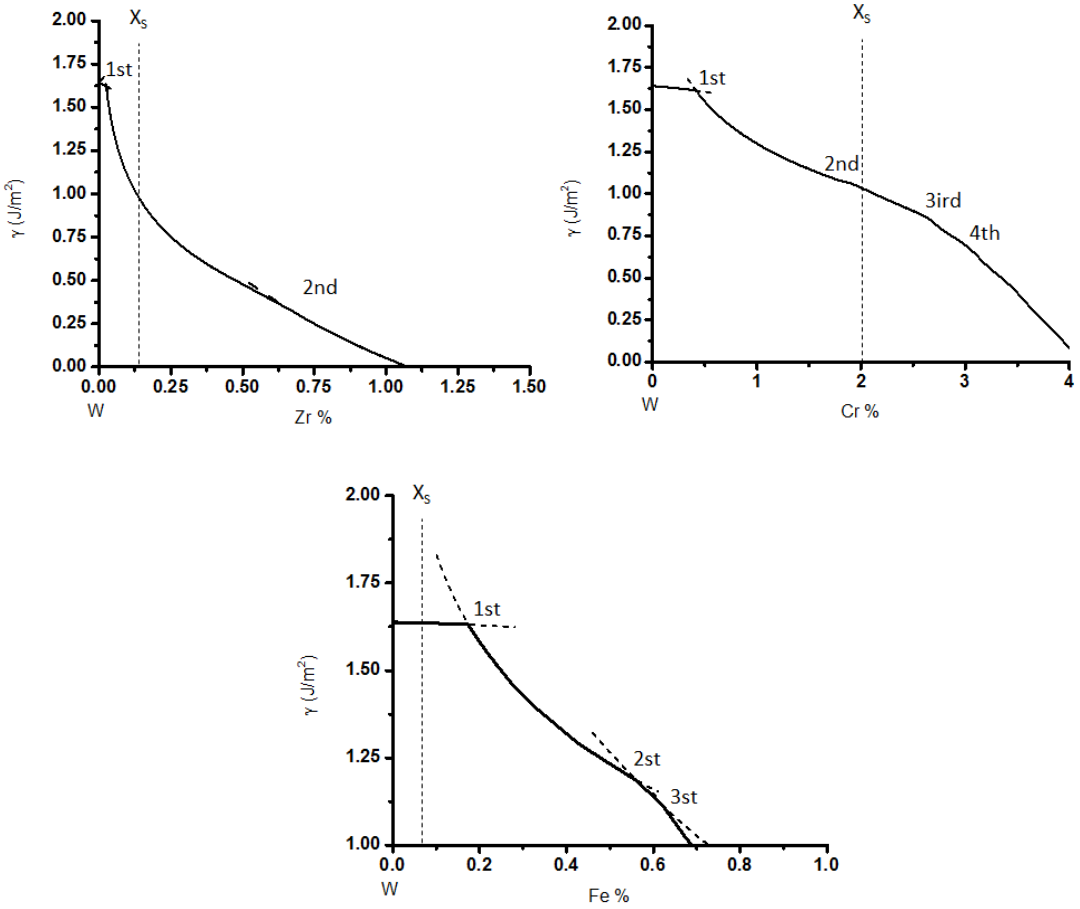

Figure III-4: Computed grain boundary energy *vs.* the solute concentration curves for W-*X* alloys (*X* = Zr, Cr, and Fe) at 973 K. The solid solubility limits (X_S) are also labeled.

Fig. III-4 illustrates three computed grain boundary energy *vs.* the solute concentration curves for W-Fe, W-Zr, and W-Cr, respectively. Similar to the W-Co case, these alloying elements can effectively reduce the grain boundary energies of W via segregation. For example, our computation suggests that adding 1 at. % of Zr can effectively reduce the GB energy to zero (although the solid solubility of Zr in W is < 0.2 at. %), while adding 1 at. % of Cr or Fe can reduce the grain boundary energy by 30% - 40%. In all cases, the solid solubilities of chosen dopants are below the compositions that are required to reach zero grain boundary energy; thus, an equilibrium grain size can be realized only in the metastable region. Before performing systematic numerical experiments, we have summarized (and calculated) the properties of transitional metals related to segregation behavior. Generally, the segregation enthalpy of solute atoms is dependent on its elastic energy ΔE_{el} as the result of the atomic size difference from matrix component and also due to the bonding energy difference between the solute atom and the bonding energy difference between solute, solvent atoms of pure state. Fig. III-5 shows the calculated elastic energy for different elements adding to W matrix. The large size elements causing mismatch are specified as: Zr, Ag, Hf, Bi, Ta and Cd. Fig. III-6 illustrated the estimated bonding energy differences (inside bulk and at grain boundaries) for selected elements. Some elements causing large bonding energy different are found to be Co, Zn, Mg and Cd. These sets of data will allow us to further design and develop numerical and actual experiments to test the effects of different alloying elements in W alloys.

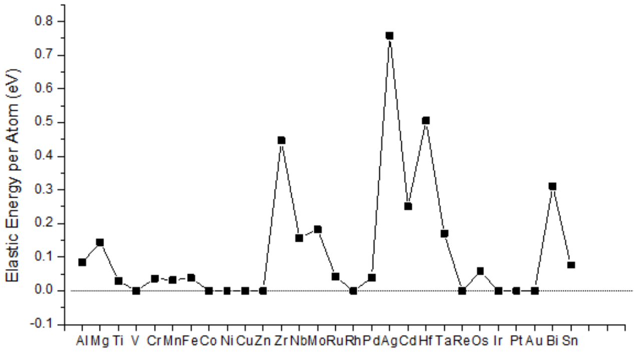

Fig. III-5: Computed elastic energy for different elements doped in W bcc phase.

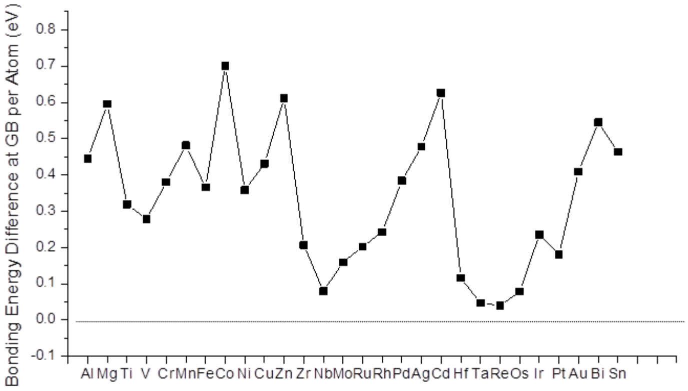

Fig. III-6: Computed bonding energy difference between different elements and W at pure bcc solid state.

Figs. III-7, 8, 9 and 10 plot the calculated GB absorption/GB energy versus the solute concentration for W-Zr, W-Co, W-Cr and W-Fe at different temperatures. It can be seen that with the same bulk composition, the GB absorption is lower at higher temperature which can be attributed to the entropic effect. Such reduction of GB absorption due to the temperature elevation limits the solutes’ ability in reducing GB energy, e.g. 1% of Co is able to reduce 60% GB effective GB energy at 1250K while at 1750k the GB energy reduction is only 20%.

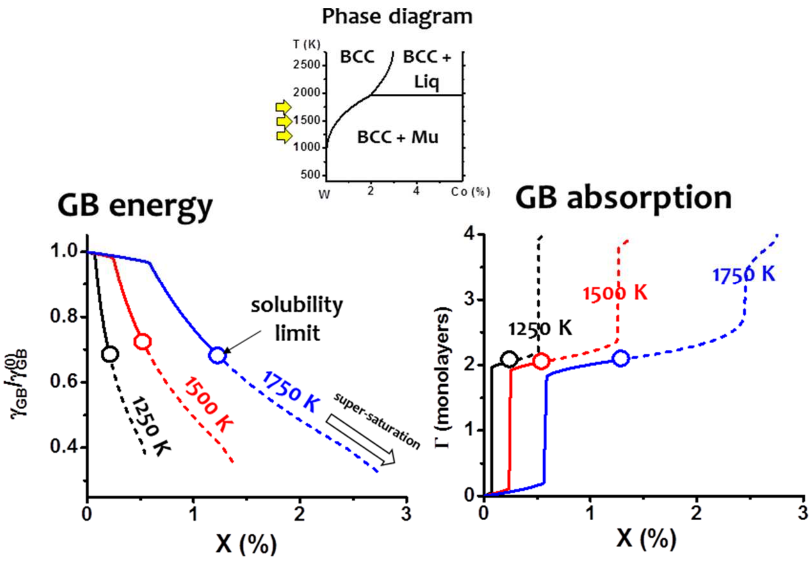

Fig. III-7: Computed GB energy and GB absorption of Co-doped W alloy at three different temperatures. Solid curves are results within the solidus compositions (marked by hollow dots) beyond which the bulk phase is supersaturated. The bulk phase diagram is plotted to show the calculated region.

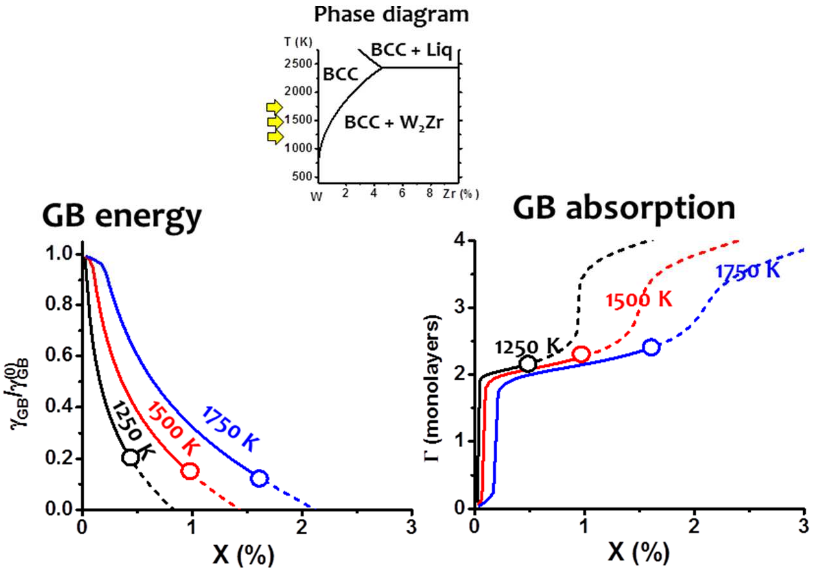

Fig. III-8: Computed GB energy and GB absorption of Zr-doped W alloy at three different temperatures. Solid curves are results within the solidus compositions (marked by hollow dots) beyond which the bulk phase is supersaturated. The bulk phase diagram is plotted to show the calculated region.

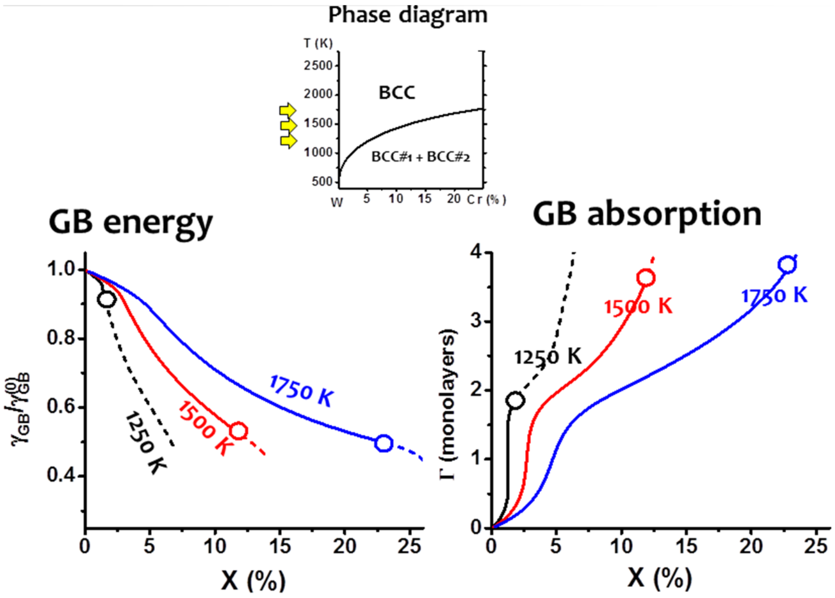

Fig. III-9: Computed GB energy and GB absorption of Cr-doped W alloy at three different temperatures. Solid curves are results within the solidus compositions (marked by hollow dots) beyond which the bulk phase is supersaturated. The bulk phase diagram is plotted to show the calculated region.

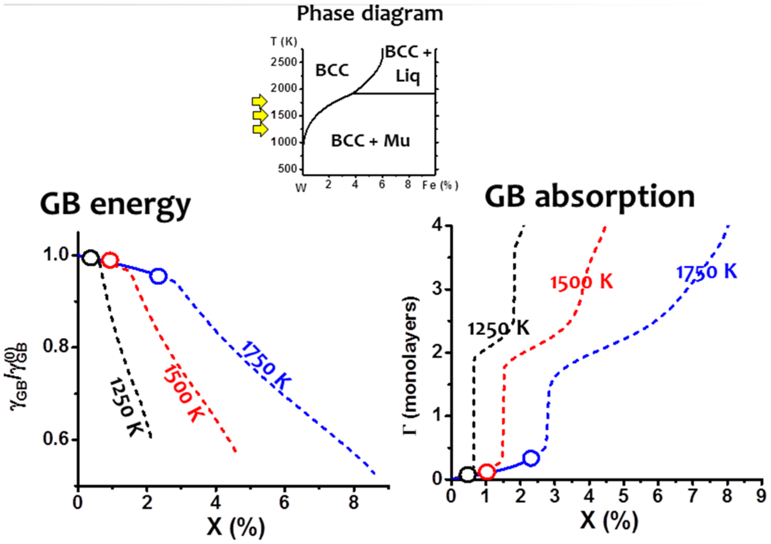

Fig. III-10: Computed GB energy and GB absorption of Fe-doped W alloy at three different temperatures. Solid curves are results within the solidus compositions (marked by hollow dots) beyond which the bulk phase is supersaturated. The bulk phase diagram is plotted to show the calculated region.

Following the early computations, a GB “phase” diagram was calculated for Zr-doped W and shown in Fig. III-11. GBs exhibit several stable phase-like structures and first-order transitions may occur between them with varying composition (chemical potential) and/or temperature. The corresponding GB adsorption vs. bulk composition curves are shown in Fig. III-8 for three selected temperatures, where the first-order transitions are represented by discontinuous changes in GB excess of solute. Such first-order GB transitions can have significant impacts on GB transport properties, thereby changing creep behaviors abruptly.

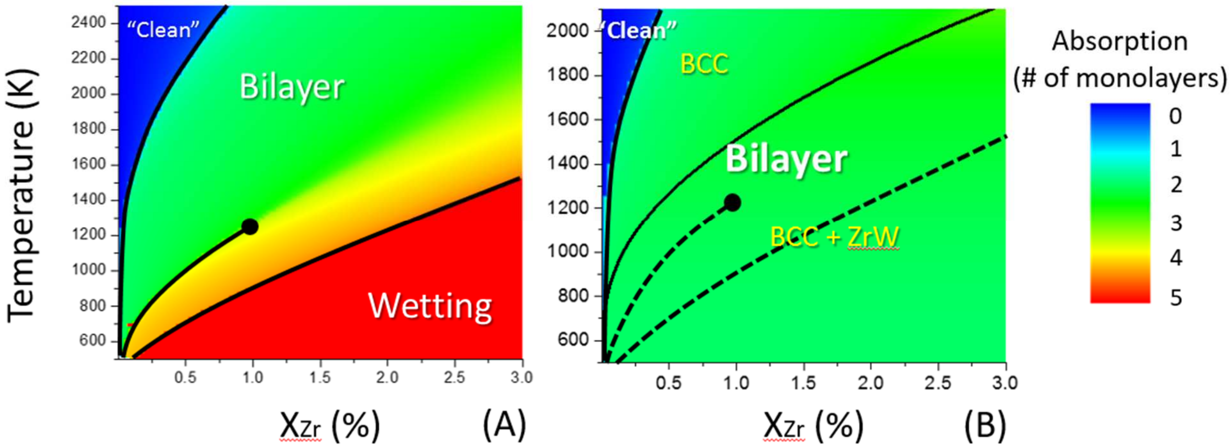

Fig. III-11: Computed GB "phase" diagram using the Wynblatt-Chatain model with **(A)** only BCC phase and **(B)** both BCC phase and secondary bulk ZrW phase (as precipitation) for the Zr-doped W binary system.

GB λ diagram considers the GB adsorption in disordered GB at high temperature, while Wynblatt-Chatain model considers the GB adsorption in ordered GB at low temperature. Different GB adsorption will result in different GB transition in these two models. Therefore, we compared the GB "phase" diagrams in Cr-doped W and Fe-doped W systems calculated by λ diagram and Wynblatt-Chatain model, respectively. In the calculated GB diagrams for Cr-doped W by using λ diagram (Fig. III-12A1), no GB transition were found. This is because no adsorption in the disordered GB at high temperature. Considering the GB adsorption in the ordered GB at low temperature, the Cr-doped W GB "phase" diagram calculated by using Wynblatt-Chatain model exhibited GB transition as shown in Fig. III-12 (A2). Fig. III-12 (B1) showed the calculated GB diagrams for Fe-doped W by using λ diagram. The disordered GB in λ diagram showed the adsorption layer transition. However, the Fe-doped W GB "phase" diagram calculated by using Wynblatt-Chatain model exhibited no transition as shown in Fig. III-12 (B2).

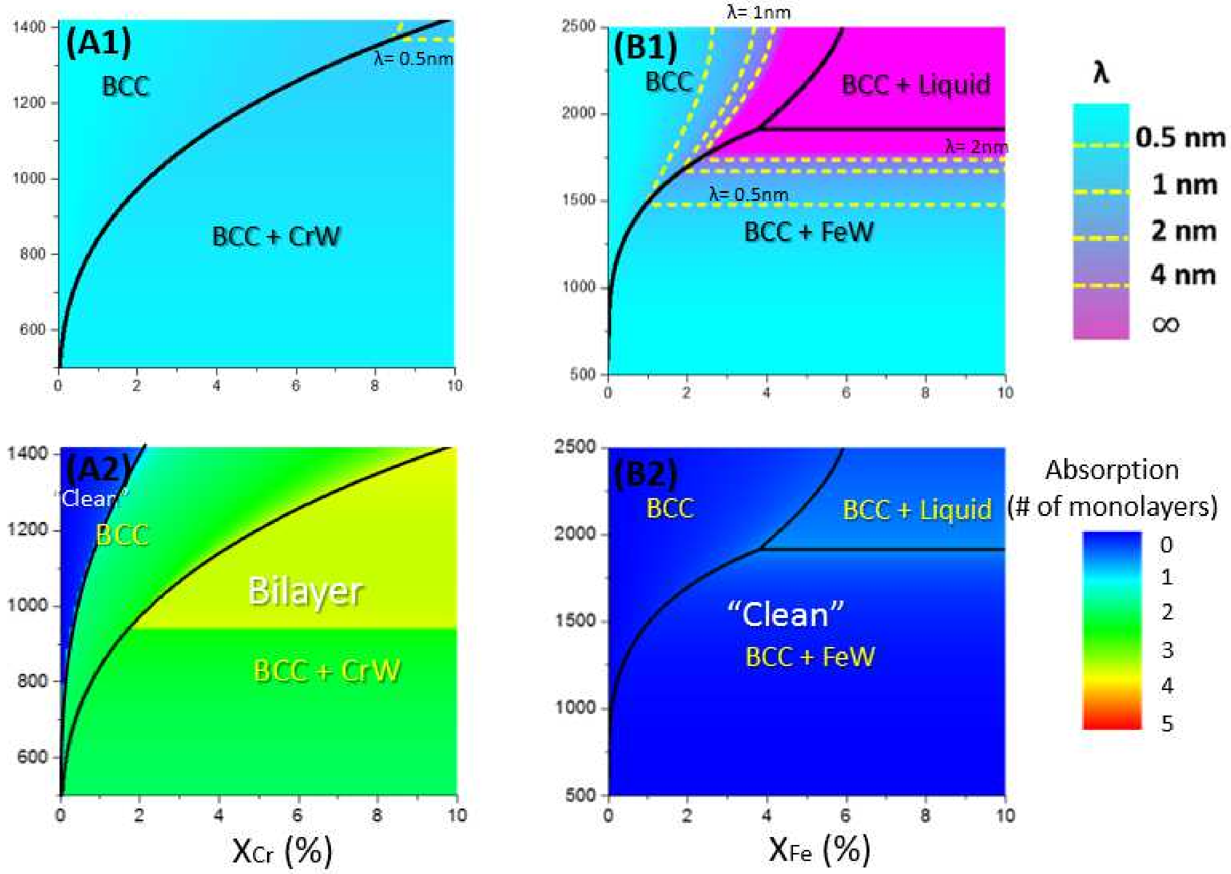

Fig. III-12: Computed GB "phase" diagrams of W-Cr system by using the **(A1)** λ diagram and **(A2)** Wynblatt-Chatain model; W-Fe system by using the **(B1)** λ diagram and **(B2)** Wynblatt-Chatain model

We have previously established a good correlation between our computed λ diagram and the experimentally-measured GB diffusivity map (Shi and Luo (2011); Fig. III-2). Using this Ni-doped Mo system as a 'learning system', we propose and are current working on to first compute a GB λ-diagram (for a doped W system, for example) with our MATLAB code;

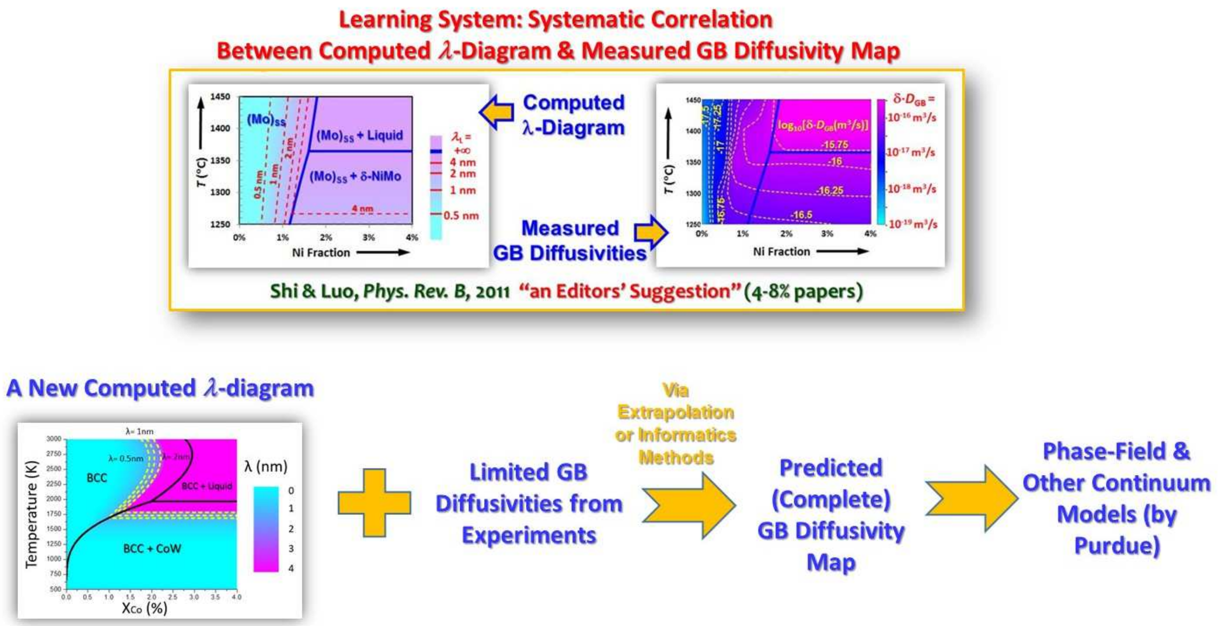

Fig. III-13: Schematic illustration of proposed work of constructing GB diffusivity map via extrapolation and informatics methods that are in progress

To start with the Ni-Mo 'learning system', measured diffusivities and computed λ data for each sintering-temperature/Ni-doped composition group were obtained in above-mentioned publication (Shi and Luo 2011). Within each sintering-temperature group, measured diffusivities and computed λ data were normalized to pure Mo system (i.e. $X_{Ni} = 0$), as shown in Fig. III-14.

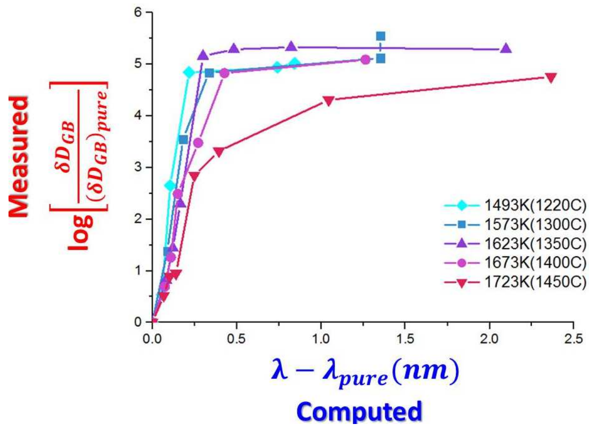

Fig. III-14: Computed λ values *vs.* measured GB diffusivities for the Mo-Ni system

The result implies normalized measured diffusivities can be correlated with normalized computed λ by using following exponential equation:

$$\ln\left[\frac{\delta D_{GB}}{(\delta D_{GB})_{\boldsymbol{pure}}}\right] = 4.958 * \left\{1 - \exp\left[-\left(\frac{\lambda-\lambda_{pure}}{0.1928}\right)^2\right]\right\} \qquad (5)$$

Here, we can reproduce the Mo-Ni diffusivity map from Mo-Ni GB λ diagram by using the correlation equation above. As shown in Fig. III-15, GB diffusivity map has been calculated from computed GB λ diagram for Mo-Ni system, while *juxtaposing* measured GB diffusivity map for comparison. This success in forecasting/reproducing GB diffusivity map verifies our original correlation assumption between λ calculations and corresponding GB diffusivities.

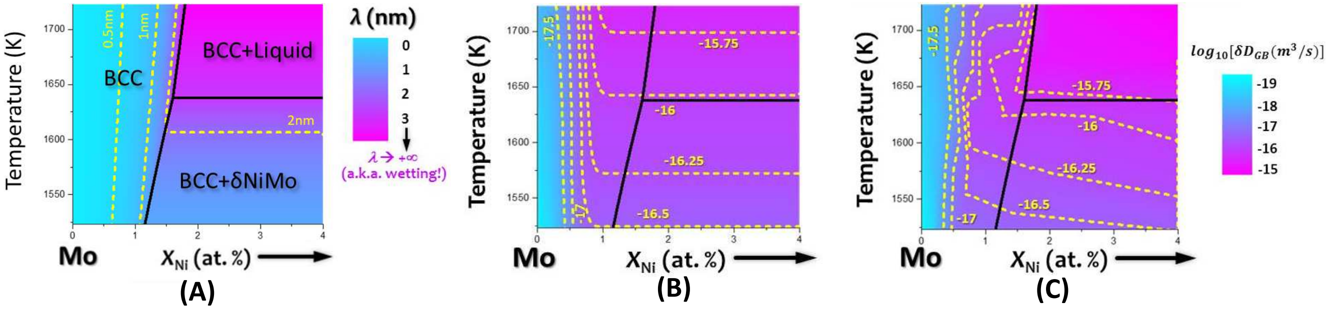

(A) (B) (C)

Fig. III-15: Mo-Ni system **(A)** computed GB λ diagram, **(B)** calculated GB diffusivity map and **(C)** measured GB diffusivity map

In addition, we also reproduced the W-Co diffusivity map from Mo-Ni GB λ diagram by using the correlation equation above. As shown in Fig. III-16, GB diffusivity map has been calculated from computed GB λ diagram for W-Co system.

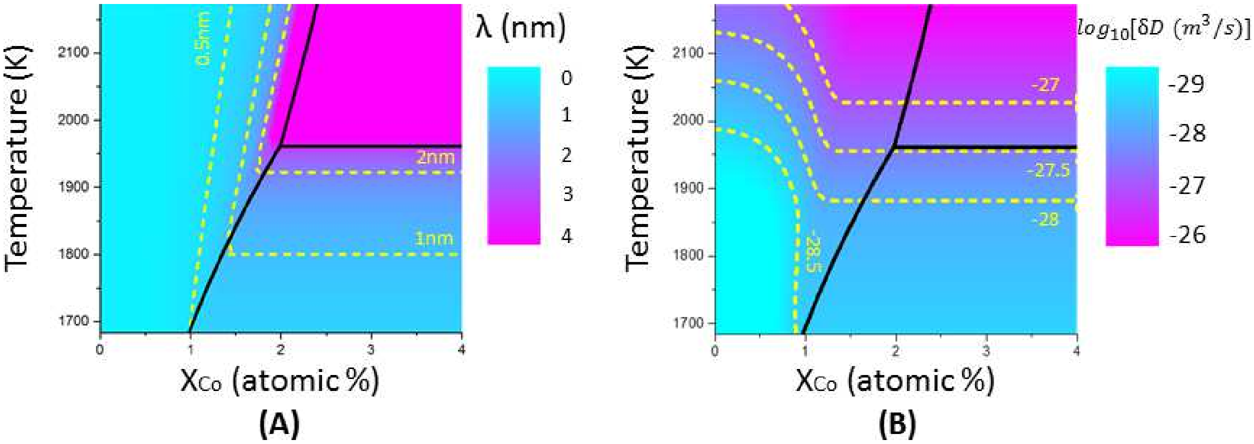

(A) (B)

Fig. III-16: W-Co system **(A)** computed GB λ diagram, **(B)** calculated GB diffusivity map

§ TASK 4 – Multiscale Modeling to Characterize Microstructure Dependent Creep Resistance:

Task 4.1 focuses on incorporating the thermodynamics and creep experiment data in the multiscale simulation setup as shown in Fig. IV.1. QM calculation and atomistic simulation can provide bond energy values as well as crystal liquid interfacial energy values to refine thermodynamic and statistical models (to be integrated with Task 4.1). Because of the computational cost and the amount of simulation time involved, a continuum microstructure cannot be analyzed with concurrent use of an atomic level simulation method. Accordingly, it is needed that material behavior information from the mesoscale atomistic analyses be transferred to the continuum analyses. In the proposed research, MD in combination with the quantum mechanical computations will be used to characterize mechanical deformation, interfacial fracture strength, and high temperature stability properties. The CFEM will be used to scale the material deformation information gathered using MD to the continuum length and timescales, Tomar (2007; 2008b; a), in order to obtain creep resistance properties. The atomistic deformation analyses and continuum analyses will be based on the past work done by the PI, Tomar et al. (2004; Zhai et al. (2004; Tomar and Zhou (2005; 2006; 2007; Tomar (2008c; b; a). Recently established MD simulation procedures to analyze temperature dependent thermal stability in refs Catellani et al. (1996; Tsai and Fang (2007) and temperature dependent oxidation in ref. Furukawa and Nitta (2000) will be incorporated in the co-PI's MD method for understanding mechanical properties of near equilibrium GB structures. MD method will make use of the combined QM and kinetic Monte Carlo (kMC) based procedures described in refs Gillespie (1977; Mei et al. (2006; Chatterjee and Vlachos (2007; Gillespie (2007; Voter (2007; Li et al. (2008) for a more accurate description of chemical reactions. Multiscale simulations will use properties measured in experiments to fine-tune the simulation results.

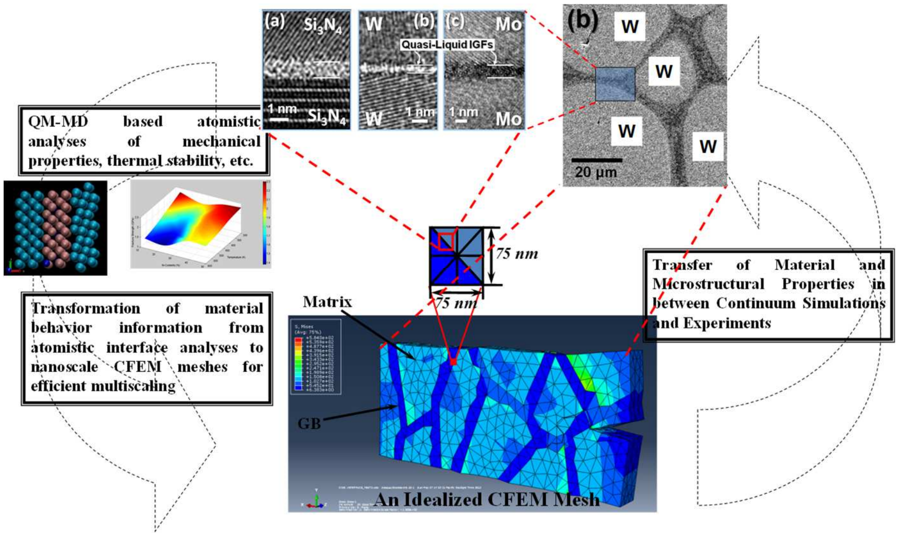

Fig. IV.1: A pictorial representation of the multiscale modeling approach

The simulation model is constructed based on the realistic W-Ni alloy GB from a HRTEM image, Gupta et al. (2007a). In the case of fully saturated GB, it has thickness about 0.6 nm. However, the neighboring region of GB has been taken as interface of W GB when calculating mechanical properties in Lee and Tomar (2014). Thus, the real thickness of GB in continuum scale should take no smaller than 2nm when modeling. Based on this idea, FE model is constructed with 60nm x 50nm 3D plate with having 2nm thickness for the GB and 20nm for the initial crack while the plate thickness is having 10nm. Plane strain load is fixed with 1μm which is applied from upper and lower surface of the plate as shown in Fig. IV.2.

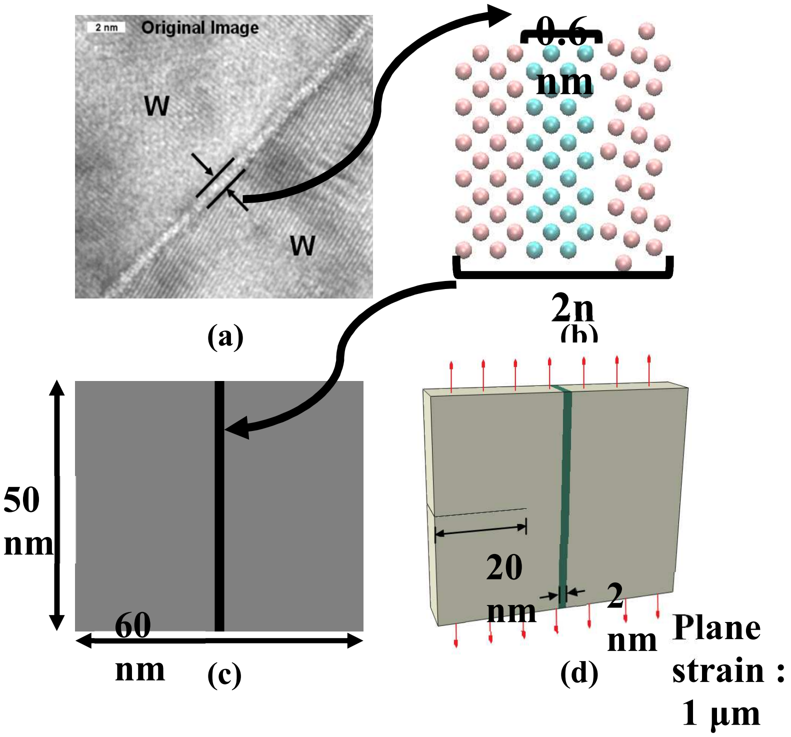

Fig. IV.2: Construction process of W-Ni alloy GB structure (a) HRTEM image, Gupta et al. (2007a), of W-Ni GB (b) atomic structure (c) 2-D dimension of interface, and (d) 3-D interface structure with boundary condition

Table 1 Stress and strain parameters of grain and grain boundary (25 at. Ni%)

	Grain	**Grain boundary (25 at. %Ni)**
Young's modulus, E	**390 GPa**	**390 GPa**
Poisson's ratio, v	**0.27**	**0.27**
Maximum principal stress, T	**4000 MPa**	**3600 MPa**
Stress with corresponding strain 1	**1400 MPa (strain = 0)**	**1400 MPa (strain = 0)**
Stress with corresponding strain 2	**2900 MPa (strain = 0.06)**	**2500 MPa (strain = 0.06)**
Stress with corresponding strain 3	**4000 MPa (strain = 0.12)**	**3600 MPa (strain = 0.12)**
Stress with corresponding strain 3	**3500 MPa (strain = 0.2)**	**3000 MPa (strain = 0.2)**

Mesh size for the 0.06 μm x 0.05 μm model is chosen to be 0.004 μm after the series of mesh size tests for convergence issue. Mesh size of 0.04 μm and 0.4 μm are used for 0.6 μm x 0.5μm model and 6 μm x 5μm model, respectively. Eight-node linear element type has been used and total number of 585 elements is created to represent crack propagation. No re-meshing technique has been used during the crack propagation since XFEM discretization allows the model to add degrees of freedom for those cracked elements with enrichment.

RESULTS

The GBs of W, which can be in various forms, have been taken to crack propagation simulation to find the characteristics of GB failure. It is found that there are two main factors that influence the crack propagation of GB. Firstly, geometrical property such as GB thickness is known to be greatly affecting the crack propagation characteristic. GB thickness can be controlled by the level of saturation during the sintering process and GBs act as a barrier for stress concentration during crack propagation. To characterize the fracture of GB, fracture parameters such as fracture toughness needs to be defined. However, the fracture toughness is scale dependent parameter which the model needs to be large enough to measure. Different length scales are taken account to visualize the effect of simulation model's dimension to the crack propagation and the appropriateness of defining fracture toughness of small scale GBs is discussed. Another factor is chemical formation of GBs. Crack propagation of W-Ni alloy is found to be affected by the percentage of Ni in the GB. Strain energy, plastic energy dissipation, and damage progress of different Ni percentage containing GBs are calculated and compared. Using the stress near the vicinity of cracks the stress intensity factors are calculated along the crack propagation path. The fracture toughness of each simulation is gathered to find the relation between the fracture strength and the fracture toughness. The brittleness index of W-Ni GB is defined to numerically characterize the GB embrittlement of W-Ni alloy as a function of Ni percentage and GB thickness.

- Effect of interface thickness to the fracture of GB

The GB thickness of W can be controlled by the level of saturation during the material manufacturing process. Although the volume of GB is relatively small when considering the whole model, the thickness of GB can greatly affect the material’s crack propagation. Models with GB thickness of 2nm, 4nm, and 8nm have shown significantly different crack propagation rate. As shown in the Fig. IV.3, thin layer of GB is playing a role which can be seen as a barrier or an accelerator to the propagation of a crack which changes the rate of the propagation.

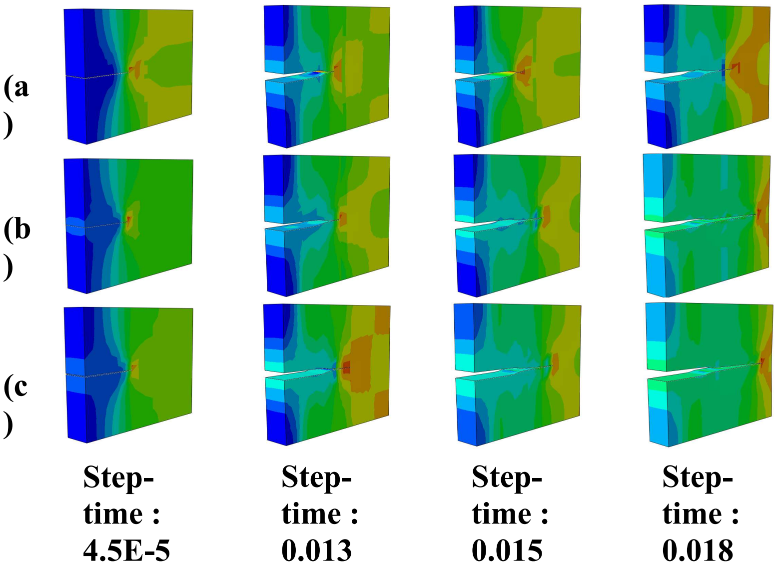

Fig. IV.3: Crack tip position as a function of loading increment for (a) GB thickness of 2nm, (b) GB thickness of 4nm, and (c) GB thickness of 8nm

The crack propagation rate is not only varying the GB failure speed but also influencing the rate of releasing strain energy during the segregation. In Fig. IV.4, the effect of GB thickness to the crack tip position and the strain energy release are shown. By having different thickness of GBs, the rate of crack propagation varies from the initial crack position and this indicates possible fracture toughness change for the entire model, not just GB.

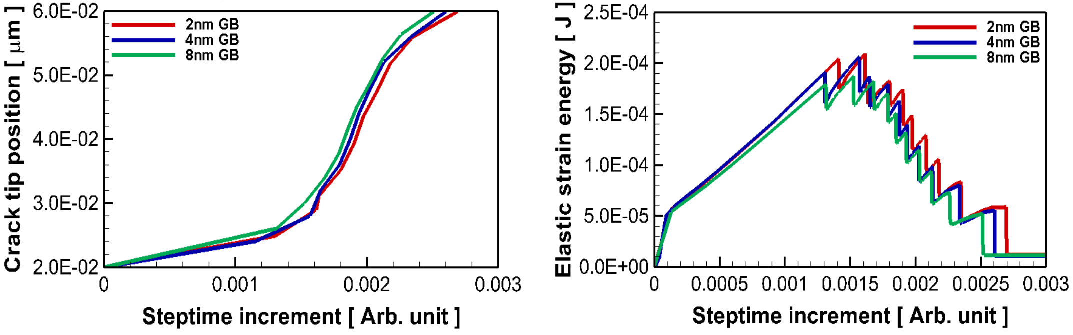

(a) (b)

Fig. IV.4: Effect of GB thickness to the (a) crack tip position and (b) strain energy release with respect to the time-step increment

- Effect of simulation length scale

Since this study is mainly focusing on the sub-micrometer scale, the result may possibly be apart from the realistic value due to length scale effect. To check the validity of the length scale appropriateness, the energy dissipation and the strain energy release per unit volume are tested and confirmed that the effect of length scale is in reasonable range which indicates that the stress intensity factor for sub-micrometer scale can be considered in same manner as micrometer scale. The effect of length scale to the energy dissipation and the strain energy release are shown in Fig. IV.5.

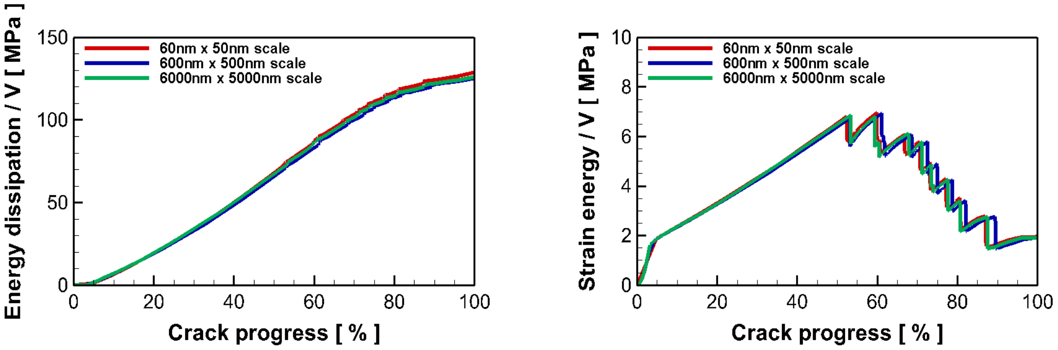

(a) **(b)**

Fig. IV.5: Length-scale effects to (a) the total energy by the volume and (b) the strain energy by the volume of the 3-D model

As shown in Fig. IV.5, the effect of length scale is found to be trivial with perspective of energy dissipation from the crack propagation. This indicates that the fracture mechanism of GB in sub-micrometer scale and its parameters can be treated as those of larger scale.

The role of GBs formation in crack propagation

In W-Ni alloy, amount of Ni addition is another factor that influences the fracture properties of GB. In the previous reports, it is found that in the process of adding Ni impurity the Ni atoms tend to segregate along the GB region and cause GB embrittlement. To investigate such effect, GBs with different Ni percentages are considered in crack propagation and analyzed. When the crack is passing through GB the speed of crack is influenced by Ni percentage and damage dissipation energy is also showing different patterns as shown in Fig. IV.6.

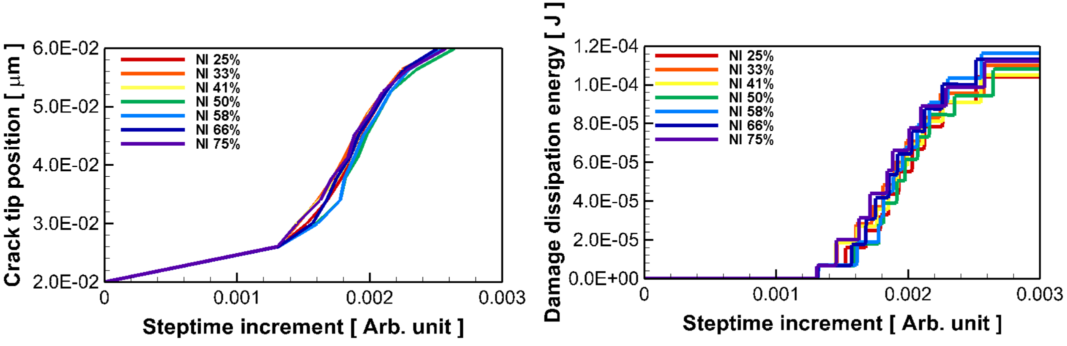

(a) **(b)**

Fig. IV.6: Effect of Ni percentage to the (a) crack tip position and (b) damage dissipation energy with respect to the time-step increment

Stress intensity factor calculation from the presented simulation results

During the crack propagation through the interface, mode I stress component near the vicinity of crack is taken to calculate the stress intensity factor along the path of crack. The points of interest are in the initiation of the crack propagation and within the GB region. It is found that the GB thickness change does not influence much on the stress intensity factor within the GB region. However, it gives significant effect on the stress intensity factor in the crack initiation as shown in Fig. IV.7 (a). On the other hand, an effect of Ni percentages shows opposite trend from that of GB thickness effect. Ni percentage gives great influence on the stress intensity factor within the GB region as shown in Fig. IV.7 (b). These findings indicate that the geometric property and chemical property of GB formation are influencing the GB fracture differently. The thickness of GB is closely related to the overall materials' fracture behavior as shown in previous literatures while the Ni percentage is related to the local fracture property of GBs.

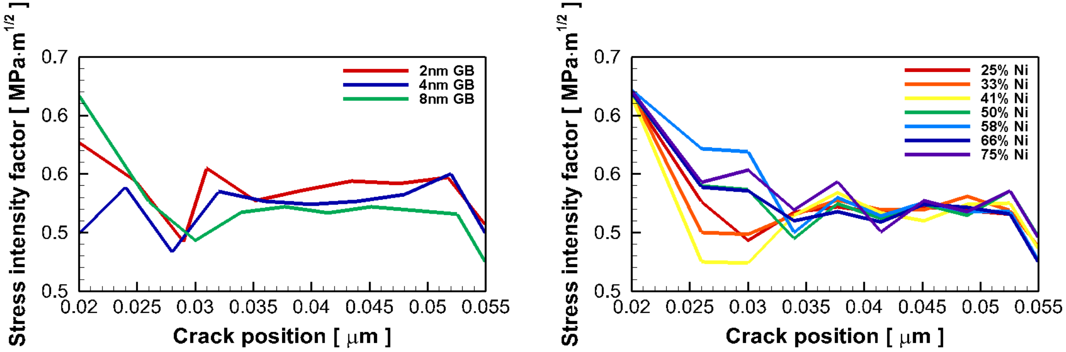

(a) **(b)**

Fig. IV.7: Stress intensity factor verses crack position as a function of (a) GB thickness and (b) Ni percentage

Fracture toughness and brittleness index calculation

Obtaining the fracture toughness in experiment requires specific methods which need certain specimen size and it has to be large enough to ensure plane strain condition. However, requirements from fracture toughness test can't be applied to GB model due to the limitation of length scale. Using the definition of the stress intensity factor that the critical value of the stress intensity factor is equivalent to the fracture toughness, GB model's fracture toughness has been obtained and analyzed. The fracture toughness of whole model and GB local is considered separately to characterize only for GB region. The fracture toughness of simulations with different length scale is calculated and mapped with respect to the GB thickness and the Ni percentage as shown in Fig. IV.8.

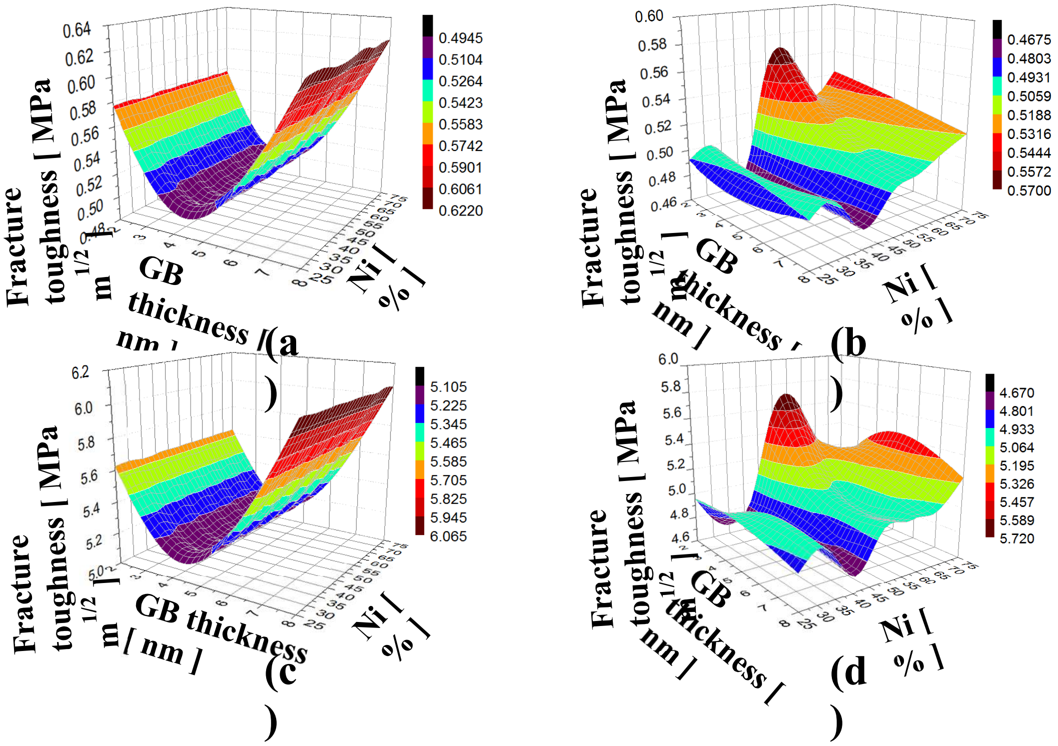

Fig. IV.8: Fracture toughness with respect to GB thickness and Ni percentage in (a) the initial crack propagation (60nm x 50nm scale), (b) within the GB region (60nm x 50nm scale), (c) the initial crack propagation (6000nm x 5000nm scale), and (d) within the GB region (6000nm x 5000nm scale)

As it was mentioned earlier, the fracture toughness value is lower than the realistic values due to finitely thin model thickness. Using the micrometer scaled model the fracture toughness of W-Ni alloy is compared with experimental values, Gludovatz et al. (2010). The range of the fracture toughness for W and W alloys are known to be 4.7~6.5 MPa·m$^{1/2}$ as shown in Fig. IV.9.

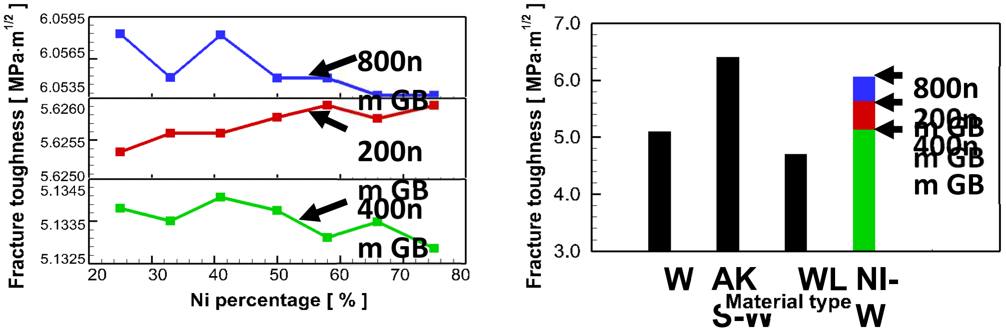

(a) (b)

Fig. IV.9: (a) Fracture toughness of 6000nm x 5000nm scale with respect to Ni percentage as a function of GB thickness, and (b) comparison of fracture toughness of W and W alloy material, Gludovatz et al. (2010), with presented result

The brittleness index, which is defined to be a ratio between the hardness and the fracture toughness, of GB is calculated using the hardness relation and obtained fracture toughness in fig. 8. Then, the brittleness index of GBs is compared with that of grains to characterize the GB embrittlement caused by Ni addition with respect to different length scale and GB thickness as shown in fig. 10.

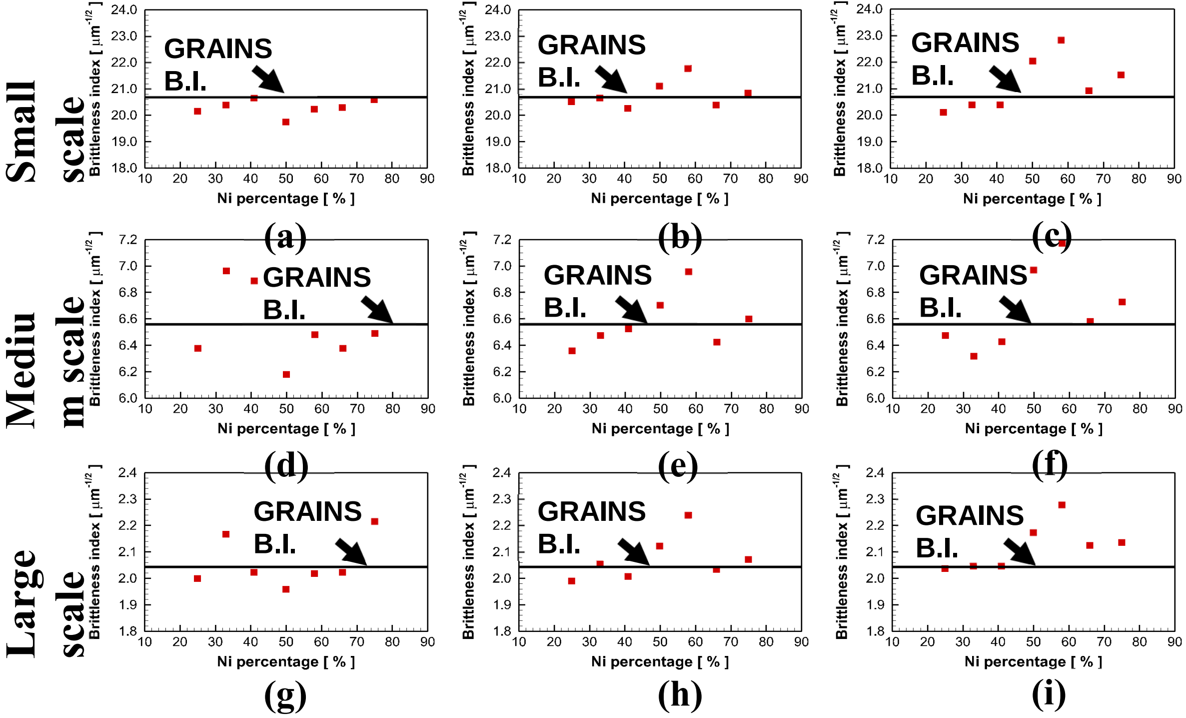

Figure IV.10 Brittleness index of simulations with respect to the Ni percentage for (a) GB thickness of 2nm, (b) GB thickness of 4nm, (c) GB thickness of 8nm in 60nm x 50nm dimension, (d) GB thickness of 2nm, (e) GB thickness of 4nm, (f) GB thickness of 8nm in 600nm x 500nm dimension, (g) GB thickness of 2nm, (h) GB thickness of 4nm, and (i) GB thickness of 8nm in 6000nm x 5000nm dimension

It is observable that there are big gaps in the brittleness index for different length scale due to the scale dependent fracture toughness which is in the formulation of the brittleness index. This length scale dependence makes it difficult to directly compare the brittleness of materials, especially in small scale. Calculated brittleness indices are taken to a curve fitting to find the tendency of the brittleness of index as a function of length scale and it is found to be in a relation of $B = \alpha L^{-1/2}$, where L is length of the total crack and α is a coefficient for describing weight of the length scale for specific material. The curve fitting of length scale dependence is shown in fig. 11 (a). In W-Ni alloy, it is found to be $\alpha = 3.7$. As it was mentioned in the work of Lawn and Marshall (1979), the brittleness index has unmatched dimension which leaves (μm)$^{-1/2}$ for the for the dimension. The brittleness length scale relation developed by curve fitting explains the incompleteness of the brittleness index. Using the brittleness length scale relation by multiplying to the original brittleness index formulation, a modified brittleness index definition is introduced as

$$B^* = \frac{H}{K_c}\cdot\alpha\sqrt{L}\,.$$

The modified brittleness index is dimensionless and could be used for direct comparison without the limitation of length scale as shown in fig. 11 (b).

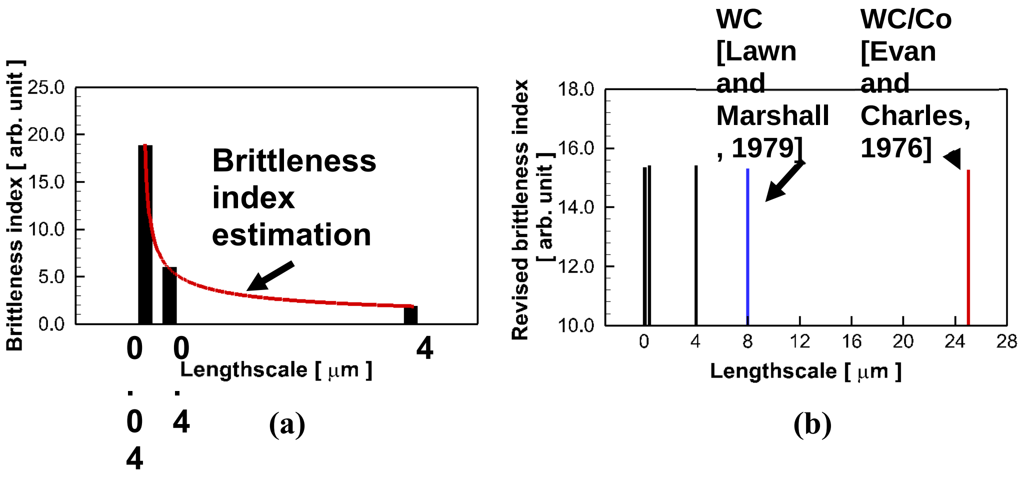

(a) (b)

Figure IV.11 (a) Length-scale effect on the brittleness index and the estimation, and (b) revised brittleness index as a function of length-scale

The brittleness characteristics for GB embrittlement with different length scales and Ni percentages are recalculated with modified brittleness index for direct comparison as shown in fig. 12. Impurities in GB were known to be a main reason of embrittlement effect in GBs, but quantitative support was not available. From this comparison, it is clear to see that the nickel percentages of 50% ~ 60% are giving the GBs the most GB embrittlement effect to the crack propagation.

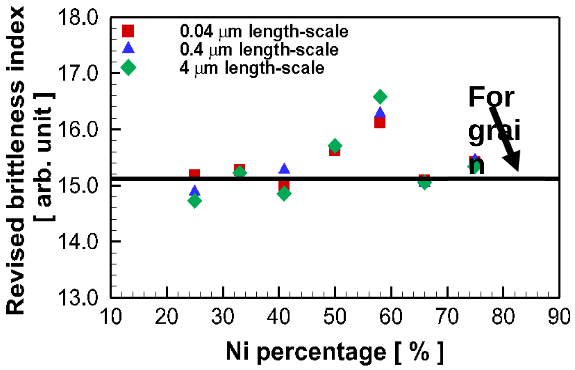

Figure IV.12 Comparison of the revised brittleness index for different types of GB as a function of Ni percentage

While brittleness of bi-granular GB models can be generalized as a function of geometry, multi-granular model makes it difficult to find relation between GB geometry and brittleness index due to geometrical complexity. However, different microstructural morphologies have shown to hold specific level of brittleness index as shown in Fig. IV.13.

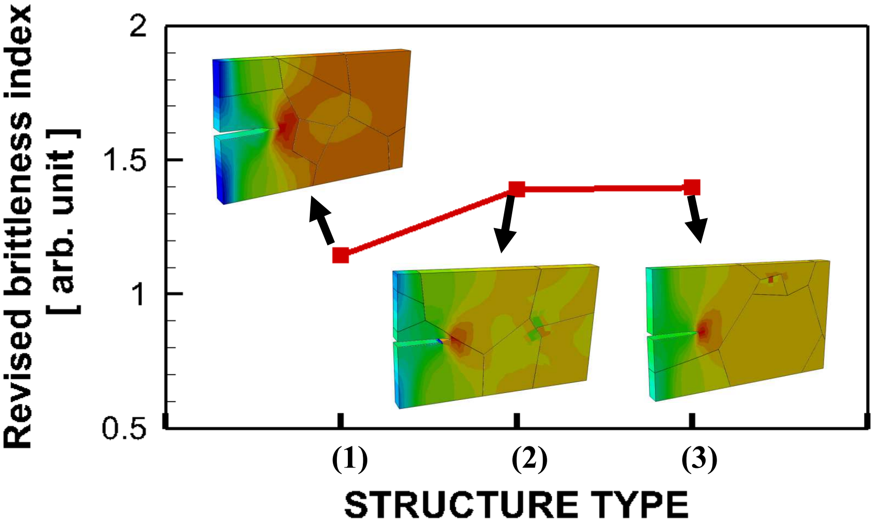

Figure IV.13 Effect of microstructure morphology to the brittleness index

While complicate combination of GB interfaces can be evaluated in terms of brittleness in microstructure, it is difficult to find reason behind it. That is because, as shown from the fracture of bi-granular models, every GB interface hold failure characteristic as a function of GBs' angle and strength property. In order to accurately analyze and predict failure of microstructure, every GB interface along the crack path has to have a general guideline for determining failure behavior. It is important to note that although the GB embrittlement is mainly caused by impurity and its segregation, geometrical factor of GBs also plays significant role.

Presented study includes failure simulations with considering the GB angle in a range of -90 ° ~ 90 °and the maximum tensile strength in a range of 3500MPa ~ 4200MPa. Due to symmetric property of GB angle, such range of GB angle can cover all possible GB interfaces in morphologies of polycrystalline materials. In order to numerically represent inter-granular and trans-granular failure, values of 1 and -1 are assigned for inter-granular and trans-granular failure, respectively. In this study, failure type that is represented in the range between 1 to -1 is denoted as failure index. In Fig. IV.14 (a), failure type as a function of GB angle and maximum tensile strength is converted to failure index and illustrated in 3-dimensional surface plot. Considering that mechanical properties of grains can vary depending on the orientation, it is required consider not only GBs maximum tensile strength but also grains' maximum tensile strength. Developing an optimized solution for obtaining the failure index from the bi-granular fracture simulation, formation of the relation can be described as

$$FI = a + b\frac{T_{GB}}{T_{Grain}} + c\theta^2.$$

Here, FI is the failure index, T_{GB} and T_{Grain} are maximum tensile strength for GB and grain, respective, and θ is GB angle. In the case of W-Ni alloy, constants a, b, and c are 4.45, -4.2, and 0.00024, respectively. By correlating the ratio of maximum tensile strength of GBs and grains with angle of interface, the relation for failure index considers both mechanical and geometrical property. Based on this relation a criterion of failure index is described as shown in Fig. IV.14 (b).

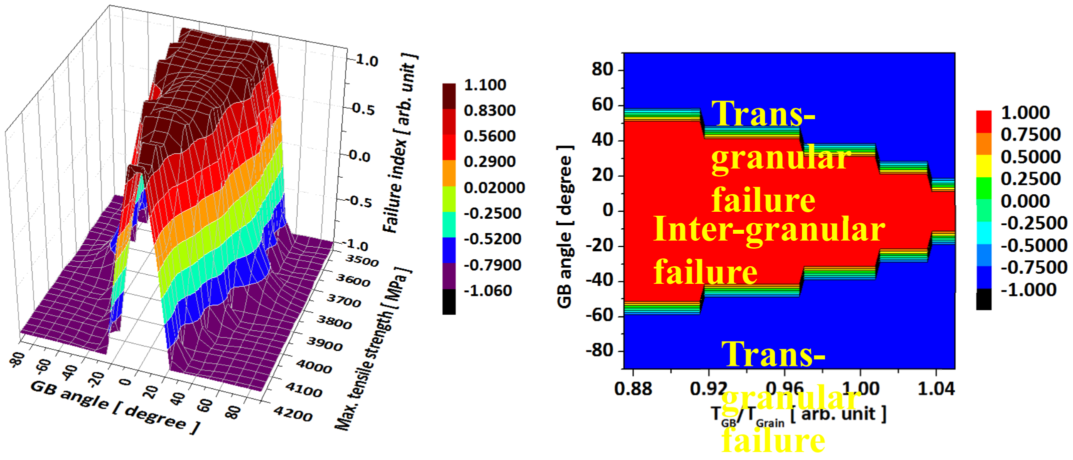

Figure IV.14 (a) Failure index as a function of GB angle and maximum tensile strength, (b) prediction criteria derived from the developed relation

Failure process of polycrystalline microstructure involves complicate geometrical properties which includes numerous grains and GBs. Considering the fundamental theory that crack tends to propagate toward the direction of the mechanically weakest point in inhomogeneous material, GBs can be potential failure region. However, crack propagation of GB depends both on the geometrical and mechanical properties, thus, development of a relation which integrates effect of both properties is necessary. Once such relation can be used to explain crack propagation of polycrystalline W-Ni alloy, it can be reversely used to predict GBs' maximum tensile strength. While calculation of GBs' mechanical maximum tensile strength needs computationally expensive atomic scale quantum simulation, it is possible to predict a rough value of GBs' maximum tensile strength if a failure index criterion is once available for specific material of interest.

Although there are several possible factors which could influence trend of crack propagation of polycrystalline materials, the geometry of GB interface is one of the most critical factors along with strength properties of GB. A number of simulations in this study revealed the trend change of crack propagation as a function of both geometry and strength properties of GBs. Besides the investigation of failure type as a function of GB angle, polycrystalline morphologies of W have been undergone failure simulations with having various maximum tensile strength of GBs. Upon the given morphology of polycrystalline W, crack propagation has been simulated with different strength properties applied GBs. This provides an indication of GB strength properties' importance to the failure of polycrystalline material, and at the same time, confirms the result of failure index criteria. As shown in Fig. IV.15, microstructures having different maximum tensile strength for GBs show propagation of cracks in different path. Perfect inter-granular failure can be observed in Fig. IV.15 (a), where having GBs' maximum tensile strength of 3500MPa. Greater percentage of trans-granular failure can be observed as GBs' maximum tensile strength becomes greater. In Fig. IV.15 (c), (d), a branching of the crack can be seen in low angled GB, which implies the uncertainty of crack path in the case of T = 4200 MPa. And this can be explained from the findings that dissipation of internal energy in lower angle has high uncertainty as maximum tensile strength varies.

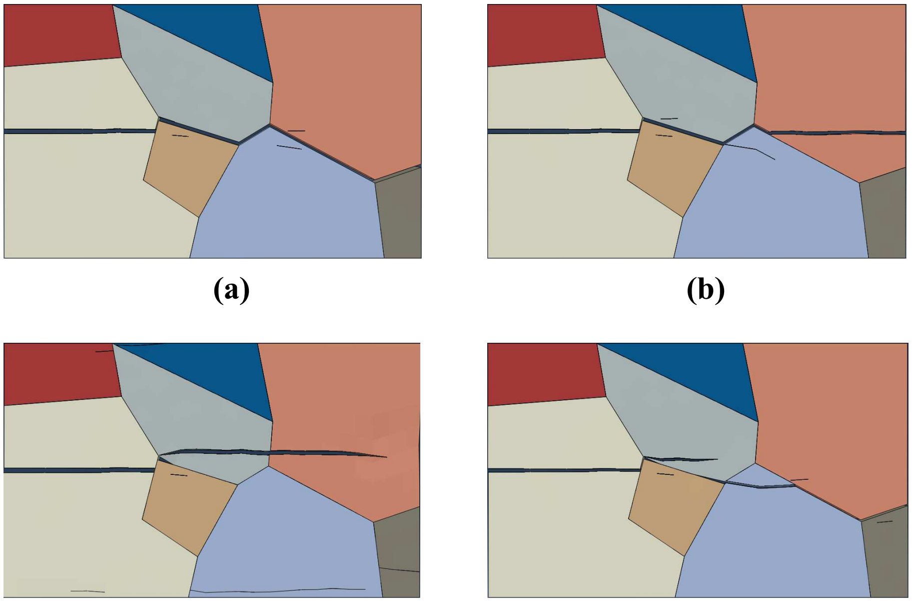

(a) (b)

(c) (d)

Figure IV.15 Crack propagation path as a function of the maximum tensile strength when (a) T = 3500 MPa, (b) T = 3700MPa, (c) T = 4100MPa, and (d) T = 4200MPa

Plastic energy dissipation and internal energy dissipation as a function of maximum tensile strength are shown in Fig. IV.16 (a) and 11 (b), respectively. Magnitude of both energy dissipations is in the similar range and this implies that most of the energy is dissipated in the form of plastic deformation. From fig. 10, lower GB's maximum tensile strength produced high percentage of inter-granular failure and energy dissipation result shown in fig. 11 describes lower energy dissipation with lower GB's maximum tensile strength. It may be seen as an obvious result when considering the fundamental fracture theory that crack propagation path tends to follow a route where needs less energy to generate crack surfaces, however, it is interesting to observe that in lower GB's maximum tensile strength, mostly in inter-granular failure, the length of the crack path is greater.

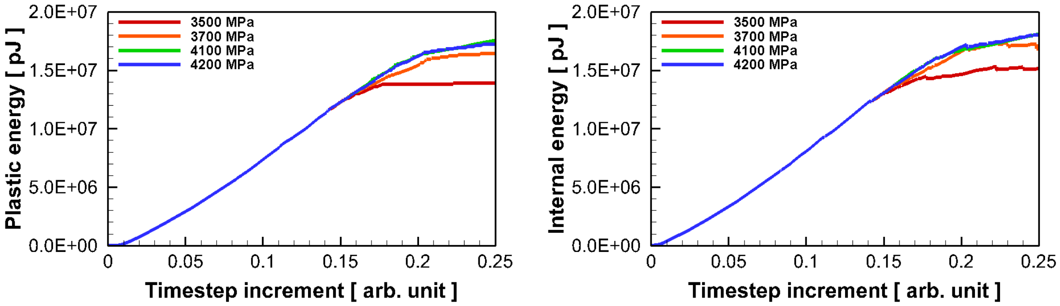

(a) (b)

Figure IV.16 Dissipation of (a) plastic energy and (b) internal energy for microstructure fracture with different GBs

Figure IV.17 shows crack propagation path of polycrystalline W microstructure, which contains GBs having different maximum tensile strength. It is important to note that grains shown here are having fixed mechanical properties. With having same geometrical properties of grains and GBs, it is observed that the maximum tensile strength of GB interface can affect significant change in failure type of the material. In order to confirm the validity of failure index criterion shown in fig. IV.14, crack propagation path of various polycrystalline morphologies have been undergone failure simulations and compared with the predicted crack path from failure index. Such comparisons of crack propagation path and actual result from experiment are shown in Fig. IV.17.

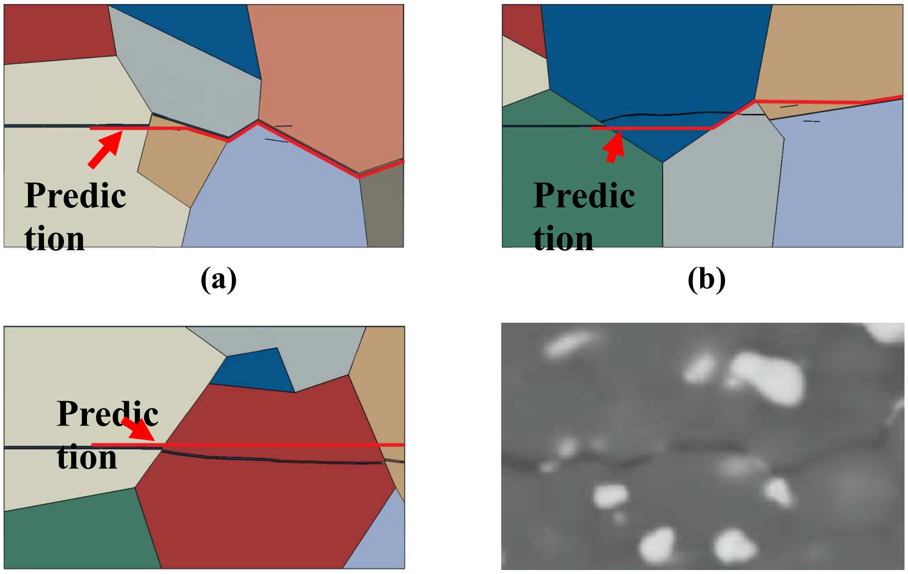

(a) (b)

(c) (d)

Figure IV.17 Comparison of crack path in polycrystalline W with the predicted crack path from failure index for different morphologies (a), (b), and (c). (d) Actual crack propagation image from experiment, Pędzich (2012)

Summer of 2014 focused on incorporating microstructure evolution prediction under applied load to the above performed simulations. Such simulations can then be combined with microstructure dependent simulations performed so far and with the creep experiments in tasks 1 and 2. The following sections describe tasks. Phase field approach is sued for performing such simulations.

Phase Field Modeling to Predict Long Time Phase Evolution: Once such information is available, microstructure evolution will be coupled with microstructural failure resistance prediction described above.

Phase field modeling (PFM) is a thermodynamic modeling approach to capture microstructural evolution under different thermo-mechanical conditions. This process assigns different phase field variables to different microstructural features of a material and then aims at capturing the numerical changes in the assigned variables which in turn signifies the alteration in the microstructure. The equations for the evolution of the phase-field variables are derived based on general thermodynamic principles.Moelans et al. (2008) The phase field variables considered in this study are density of the powder particles. It also takes into account the evolution of an order parameter defined as the crystallographic orientation of each particles.

The driving force for microstructural evolution in PFM is the prospect to reduce the free energy of the system. The total energy E in PFM is formulated as a function of the set of phase-field variables and order parameters, which are functions of time and spatial coordinates. Total free energy can be represented as,

$$E = \int \left[F(\rho(r,t),T) + \frac{\kappa}{2} |\nabla \rho(r,t)|^2 + \frac{\beta}{2} |\nabla \eta|^2 \right] dV \, ,$$

where $F(\rho(r,t),T)$ being the free energy of the material, κ is the gradient co-efficient, ρ the phase field variable & η being the order parameter.Moelans et al. (2008) The 2nd and the 3rd term in Eq. 3 denotes the gradient free energy from the surface & grain boundaries, respectively.

The free energy F consists of bulk free energy (F_{bulk}), interfacial energy (F_{int}), elastic strain energy (F_{el}), and energy terms due to magnetic or electrostatic interactions (F_{fys}). It is represented as,

$$F = F_{bulk} + F_{\text{int}} + F_{el} + F_{sys} \, .$$

The bulk free energy (F_{bulk}) determines the composition and volume fractions of the co-existing phase at equilibrium condition. The interfacial energy (Fint) and strain energy (Fel) represents effect of the equilibrium compositions and volume fraction of the coexisting phases. They also determine the domain, shape and mutual arrangement of the phases.

In PFM, the temporal evolution of the phase-field variables is given by a set of coupled partial differential equations, one equation for each variable. The equations are derived according to the principles of non-equilibrium thermodynamics. They are formulated such a way that total free energy decreases monotonically and mass is conserved for all components. Solution of the partial differential equations yields the temporal and spatial evolution of the phase-field variables, which is a representation of the morphological evolution of the microstructure.

The layout of the current work has been designed as follows,

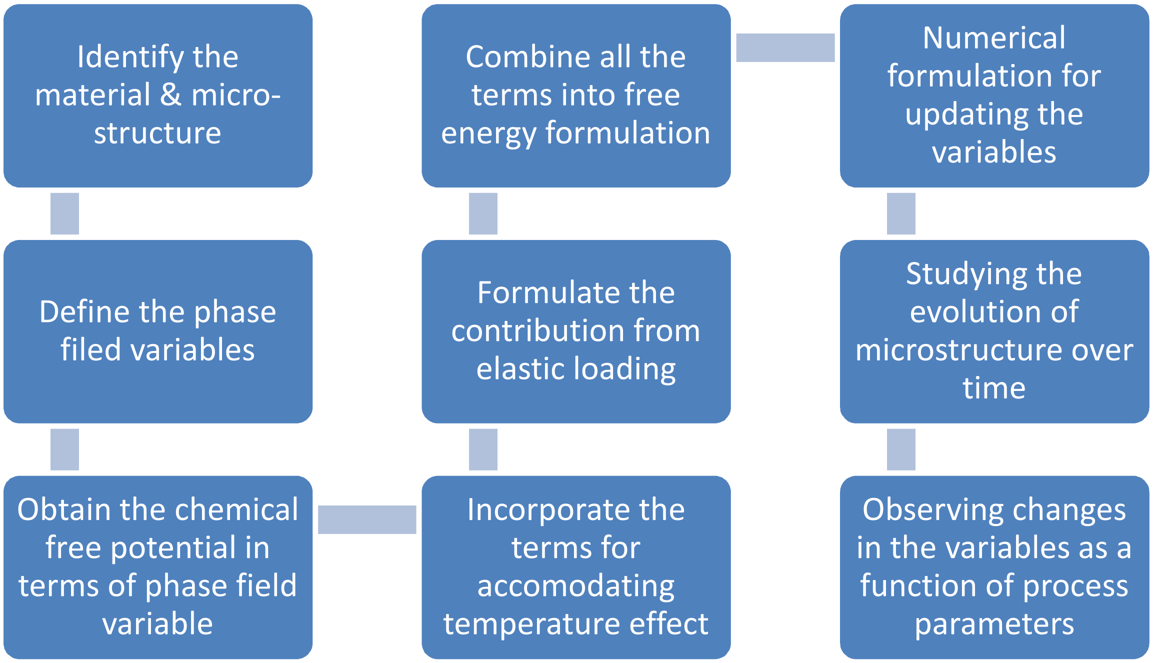

Figure IV.18 Schematic Layout of the Work

The work here starts with obtaining a microstructure and assigning initial phase field variable values to each component of the microstructure. Then total energy is formulated & evolution of the phase field parameters is studied. The material under consideration for the preliminary study is Tungsten. Moose framework will be used as simulation tool for the current problem. This tool is efficient enough to create initialized phase field structure given a microstructural image. It has a separate phase field module with inbuilt kernels and solver. It can also combine phase field and finite element method, which will be beneficial while incorporating the effect of external elastic loading. All these features motivated us to choose moose framework as our simulation tool.

Chemical Free Energy:

Bulk free energy is the main component of the free energy potential of the materials under consideration for phase field modeling. This is the chemical free energy inherited by the material. This can be obtained from molecular dynamics or quantum simulations. However, in the current work, the basic chemical free energy has been taken from Wang, 06 Wang (2006). Also additional terms have been added in order to capture the effect of temperature. Chemical free energy is represented as,

$$F(\rho,T) = A\rho^2(1-\rho)^2 + B\left[\rho^2 + 6(1-\rho)\sum\eta^2 - 4(2-\rho)\sum\eta^3 + 3\left(\sum\eta^2\right)^2\right]$$
$$+ \mathrm{RT}[(1\text{-}\rho)\ln(1\text{-}\rho) + \rho\ln\rho]$$

where, R is the universal gas constant in kJ/mole-K, ρ is density of material , η is crystallographic orientation, T is process temperature in K, A & B are constants.. The last term in Eq. (5) is added to consider the entropy contribution due to temperature. It has been observed that similar formulation is used in different phase filed problems with temperature Hu and Henager Jr (2010; Li et al. (2014). Fig. IV.18 depicts the chemical free energy used for the simulation.

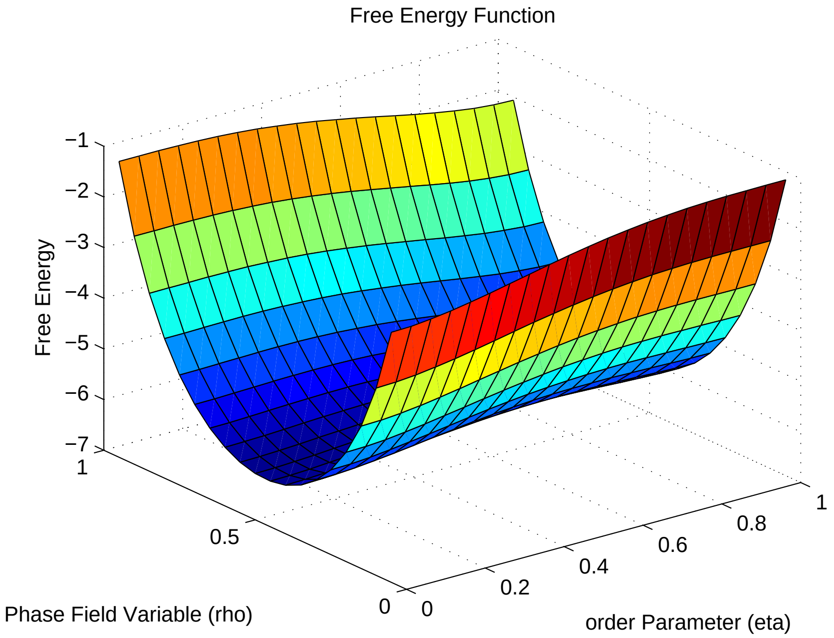

FigureIV.18. Chemical Free Energy (at T = 1000 C) for the Simulation.

The effect of temperature on the free energy has also been shown separately in Fig. IV.19.

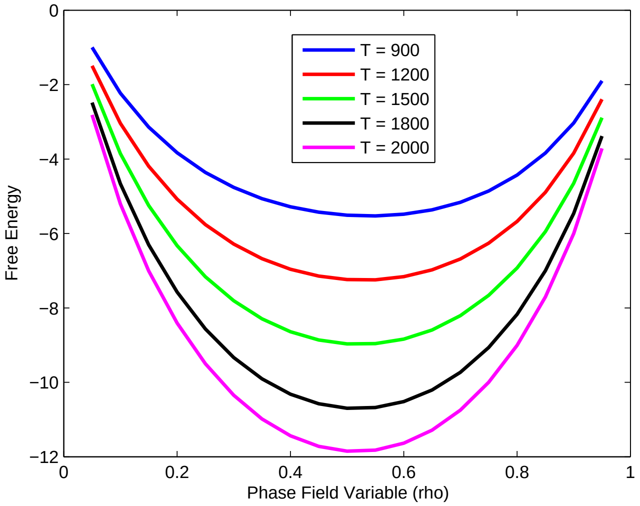

Figure IV.19. Effect of temperature on Chemical Free Energy

As observed from Fig. 12, with temperature the chemical free energy decreases. It can also been seen that the free energy is maximum at each of the pure particle or void phase, whereas being minimum at the interface. The energy formulation is constructed in a way that mass density ρ = 0 in voids and ρ=1 in solid particles. The equilibrium value of the multicomponent order parameter vanishes in pores, i.e., $\{\eta\}_{\rho=0} = \{0,0,0........0\}$ and is reached in solid at $\{\eta\}_{\rho=1} = \{1,0,0........0\} = \{0,1,0........0\} = ... = \{0,0,0.......1\}$.

Elastic Energy:

During phase transformation in case of solids, elastics stresses are being induced into the material. The transformation strains are related to the phase field variables as,

$$\varepsilon_{ij}^{0} = \varepsilon_{ij}^{\rho}\delta\rho(\vec{r}) + \sum_{k}\varepsilon_{ij}^{nk}\eta_{k}^{2}(\vec{r})$$

where, the composition field, $\delta\rho(\vec{r},t) = \rho(\vec{r},t) - \rho_0$ with reference composition, ρ_0 , is taken over the overall composition of the alloy. ε_{ij}^{xB} is the lattice expansion co-efficient which follows Vegard's law, $\varepsilon_{ij}^{\rho} = \frac{1}{a}\frac{da}{d\rho}\delta_{ij}$ with *a* being the stress free lattice parameter. ε_{ij}^{nk} represents the lattice mismatch between the daughter & parent phases.

	Grain
Young's modulus, E	390 GPa
Poisson's ratio, v	0.27
Maximum principal stress, T	4000 MPa
Stress with corresponding strain 1	1400 MPa (strain = 0)
Stress with corresponding strain 2	2900 MPa (strain = 0.06)
Stress with corresponding strain 3	4000 MPa (strain = 0.12)
Stress with corresponding strain 4	3500 MPa (strain = 0.2)

Now, the elastic strain is defined as the difference between the total strain & the stress free strain,

$$\varepsilon_{ij}^{el} = \varepsilon_{ij}^{total} - \varepsilon_{ij}^{0}$$

Thus, the elastic stress as computed from the Hook's law is,

$$\vec{\sigma}_{ij}(r) = C_{ijkl}(\vec{r})\varepsilon_{kl}^{el}(\vec{r})$$

Where, $C_{ijkl}(\vec{r})$ are the components of the elastic modulus tensor. Considering the fact that mechanical equilibrium is obtained much before the chemical equilibrium, strain is obtained by solving the equilibrium equation,

$$\frac{\partial\sigma_{ij}}{\partial r_j} = 0$$

In order to simplify the solution, total stress is assumed to consist of a homogeneous macroscopic strain & a heterogeneous local strain components,

$$\varepsilon_{ij}^{total} = \bar{\varepsilon}_{ij} + \delta\varepsilon_{ij}(r)$$

Where, the homogeneous strain is related as,

Table 2. Elastic Properties of the Material

$$\int_{V}\delta\varepsilon_{ij}(r)d^{3}r = 0$$

and the heterogeneous component can be computed from the local displacements,

$$\delta\varepsilon_{kl}(r) = \frac{1}{2}\left[\frac{\partial u_k(r)}{\partial r_l} + \frac{\partial u_l(r)}{\partial r_k}\right]$$

where, u_i is the component of the displacement vector $\vec{u}$. Finite element coding is to be done for calculating the displacement & corresponding strains. After obtaining the strains, the elastic energy is computed as,

$$F_{el} = \frac{1}{2}\int_V C_{ijkl}(\vec{r})\varepsilon_{ij}^{el}\varepsilon_{kl}^{el}d\vec{r}$$

When the effect of the external forces are also taken into consideration, the strain energy expression becomes,

$$F_{el} = \frac{1}{2}\int_V C_{ijkl}(\vec{r})\varepsilon_{ij}^{el}\varepsilon_{kl}^{el}d\vec{r} - \int_V \sigma_{ij}^{a}(\vec{r})\varepsilon_{ij}^{el}d\vec{r}$$

This elastic strain energy is accounted into the total free energy equation of the phase field model and the combined effect of the external load along with the other process parameters can be examined. A separate finite element module has to be built in moose to calculate the elastic energy. The elastic properties to be used for the elastic energy formulation are tabulated in Table1.

Numerical Formulation:

After formulation of the overall free energy, the numerical formulation is developed to capture the spatial & temporal evolution of the phase field variables. Cahn-Hilliard equation Cahn and Hilliard (1958) is used in this regard,

$$\frac{\partial\rho}{\partial t} = \nabla.\left[D\nabla\frac{\delta E}{\delta\rho}\right]$$

Similarly, the evolution of the order parameter is defined using Allen-Cahn equation,

$$\frac{\partial\eta_i}{\partial t}(\vec{r},t) = -L\frac{\delta E}{\delta\eta_i}$$

where, E is the total free energy of the system as defined in Eq.3. D is the diffusion coefficient which is defined as,

$$D = D_{vol}\varphi(\rho) + D_{vap}[1-\varphi(\rho)] + D_{surf}\rho(1-\rho) + D_{gb}\sum\eta_i\eta_j$$

where $\varphi(\rho) = \rho^3(10-15\rho+6\rho^2)$ and D_{vol}, D_{vap} D_{surf}, D_{gb} are the coefficients for diffusivity in solid bulk, vapor, along surface & grain boundaries Wang (2006). The constant values used for the present phase-field study are summarized in Table. 2.

Table 3. Constants Coefficients used in Current Study

β	**κ**	**A**	**B**	D_{vol}	D_{vap}	D_{surf}	D_{gb}	**L**
1	10	16	1	0.01	0.001	4	0.4	10

Numerical solution of Eq. (15) gives the temporal evolution of the phase-field variable which represents the changes in density of the system. In this case the diffusion coefficients are considered to be scalar. Deng Deng (2012) has shown that direction dependence of the diffusion mechanisms can also be implemented in the same formulation. The modified relation is,

$$D = D_{vol}\varphi(\rho)I + D_{vap}[1-\varphi(\rho)]I + D_{surf}\rho(1-\rho)T_s + D_{gb}\sum \eta_i\eta_j T_g$$

where, I is identity tensor and T_s, T_g are projection tensor that constraint the direction of diffusion along surface & grain boundaries defined as

$$T_s = I - n_s \times n_s \qquad \text{and} \qquad T_g = I - n_g \times n_g$$

with $n_s = \dfrac{\nabla\rho}{|\nabla\rho|}$ and $n_g = \dfrac{\nabla\eta_i - \nabla\eta_j}{|\nabla\eta_i - \nabla\eta_j|}$. The same relation will be used in current study. The domain for the simulation is to be discretized with uniform grids, and periodic boundary conditions to be imposed. Using moose framework the set of equations are solved by explicit finite difference method.

For the initial geometric modelling we will start with two particles in 2D and gradually we will move to 3D powder configuration with realistic microstructural images. Fig. IV.20 shows initial conditions to be used for preliminary study,

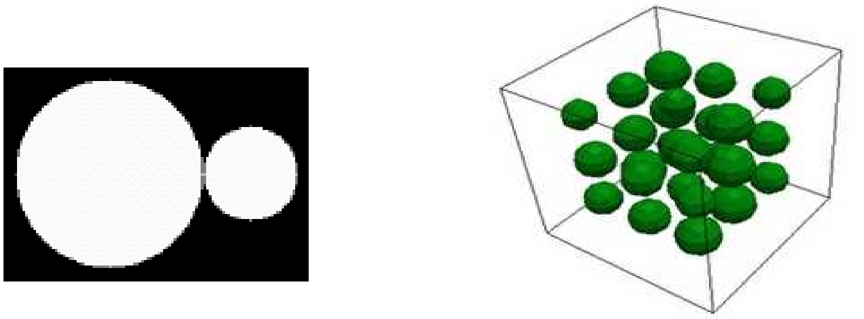

(a) (b)

FigureIV.20. Initial Conditions a) Circular particles in 2D b) Multiple particles in 3D

The initial values of the phase filed variables will be assigned as described earlier and evolution of microstructure will be studied to get the consolidation kinetics of powder. Periodic boundary condition is to be used in all 3 directions. This assumes that evolution of phase field variable repeats itself for material with higher dimension. This implies that the compaction mechanisms & dynamics predicted from the model can be applied to materials and structure with any size and dimension.

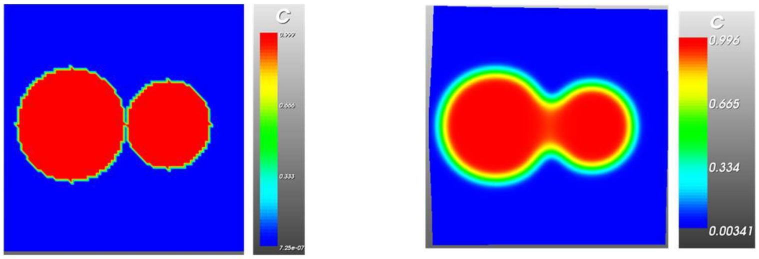

Initial Condition

Time = 0.5

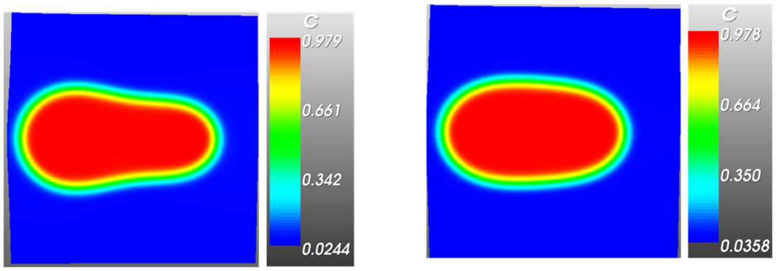

Time = 20.5

Time = 60.0

FigureIV.21. Evolution of necking microstructure without pressure in two particles

Microstructural Evolution During Sintering

The primary objective of the current study is to observe the consolidation kinetics related to compaction of powder materials undergoing sintering. Hence, as outcome of the study we will see how density of the material changes over time during the process. The simulation, thus, starts with microstructure of a powder materials and ends with the final polycrystalline configuration of the material. The microstructural images at different time steps will be presented.

Initial test runs have been performed to check the particle evolution over time. For initial runs we have built a two particle model to capture the process behavior. Images from test runs has been shown in Fig. 21. It shows the microstructure evolution during sintering process for two particle model. As preliminary validation of our model we will compare our results to previous works from literature. Going forward we will also compare the results to experimental outputs as a validation of the simulation technique & the formulation. For next step we will also use actual microstructure of materials to observe the consolidation kinetics and it’s temporal evolutionTemporal progression of volume fraction of particles has also been presented which depicts the consolidation kinetics undergoing inside the material. This has been shown in Fig. 22.

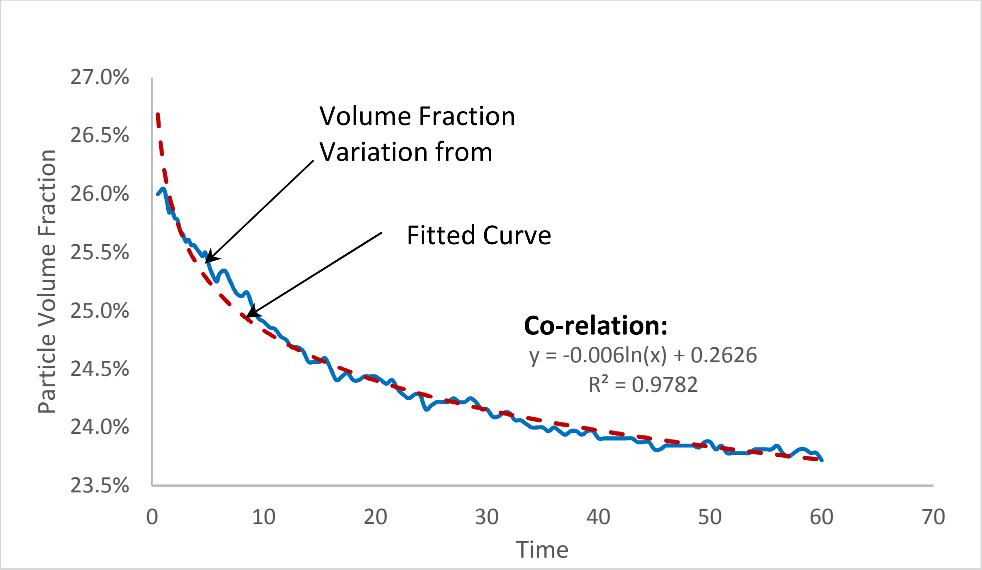

Figure IV.22 Change in particle volume fraction with time

As observed from Fig. 22, particle volume fraction decreases with time which in turn indicates that particle density increases with time. Rate of decrease in volume fraction is more in initial stages and it reduces as time progress. We have fitted curve to obtain the co-relation between particle volume fraction and time, logarithmic relation has been established between the two. The obtained co-relation is shown as,

$$\%volume = -0.006\log(t) + 0.2626$$

where, t represents the time. This also justifies the reason for different rate of change in volume fraction over time. This co-relation is obtained based on preliminary runs only, so it needs further verification. We will use actual experimental data to validate the co-relation. Effect of process parameters such as temperature & pressure is to be studied as well. Further, plots depicting variation of phase field variable as a function of temperature & pressure will be presented. Consolidation kinetics can also be quantified using effective viscosity Clarke and Jo´ nsson (1993) demarcated as

$$\eta = \frac{P}{\dot{\varepsilon}}$$

where, P is applied pressure and $\dot{\varepsilon}$ is the strain rate defined as , $\dot{\varepsilon} = \frac{d}{dt}\left(\frac{\Delta h}{h}\right)$, h being the spatial dimension of elements. Given the temperatures, the kinetics is defined using the Arrhenius law,

$$\eta = \eta_0 \exp\left(\frac{Q}{RT}\right)$$

where, Q is the activation energy and η_0 is the pre-exponential factor. Also the deformation mechanisms at a given temperature can be predicted using Arrhenius law. Dahl Dahl et al. (2007) has sintered yittria stabilized zirconiam using different sintering technique. They have reported how density & grain size of the material changes over time depending on the experimental condition such as temperature, pressure etc. Outcome of the study has been presented in Fig. IV.22.

From experimental study of SPS sintering it has been observed that density of the final structure increases with time and also with increased temperature and pressure. We expect to produce similar results from our simulations. We can select the sintering method of our interest from the different methods presented in the paper, and use it to validate our results. Although magnitude of density & other parameters might change we expect to see similar trend for tungsten from our analysis. The transformation in grain size will also help us to estimate effect of initial grain size on the consolidation kinetics of the material. We will analyze powder microstructures with different grain sizes in this regard. These results will help us validate our model for verified microstructure evolution experiments. Once the model is validated we will use model for predicting long term creep evolution.

Fig. 23 shows evolution of necking process in particles as a function of applied pressure. In comparison to what is shown in Fig. 21 earlier, the necking is now significantly evolved.

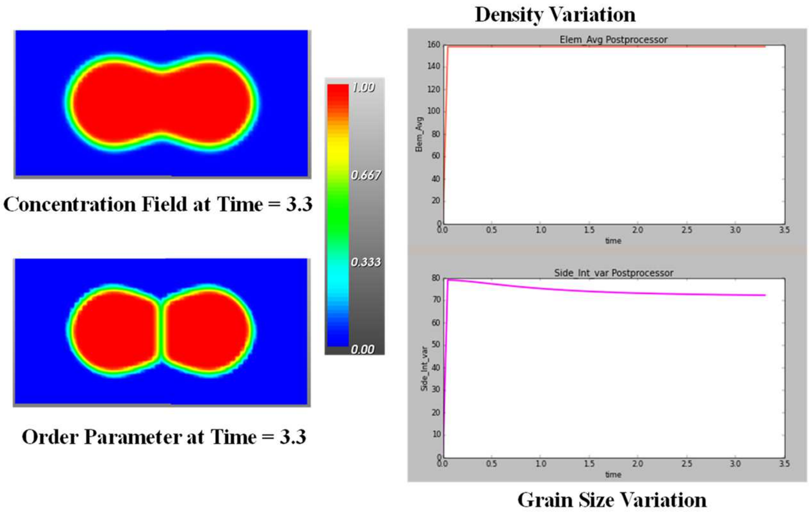
Density Variation

Concentration Field at Time = 3.3

Order Parameter at Time = 3.3

Grain Size Variation

Figure IV.23 Evolution of necking microstructure with pressure in two particles

Based on two particle simulations necking evolution in multiple particle fields was simulated. Fig. IV.24 shows microstructure evolution in multiparticle fields as microstructure evolves.

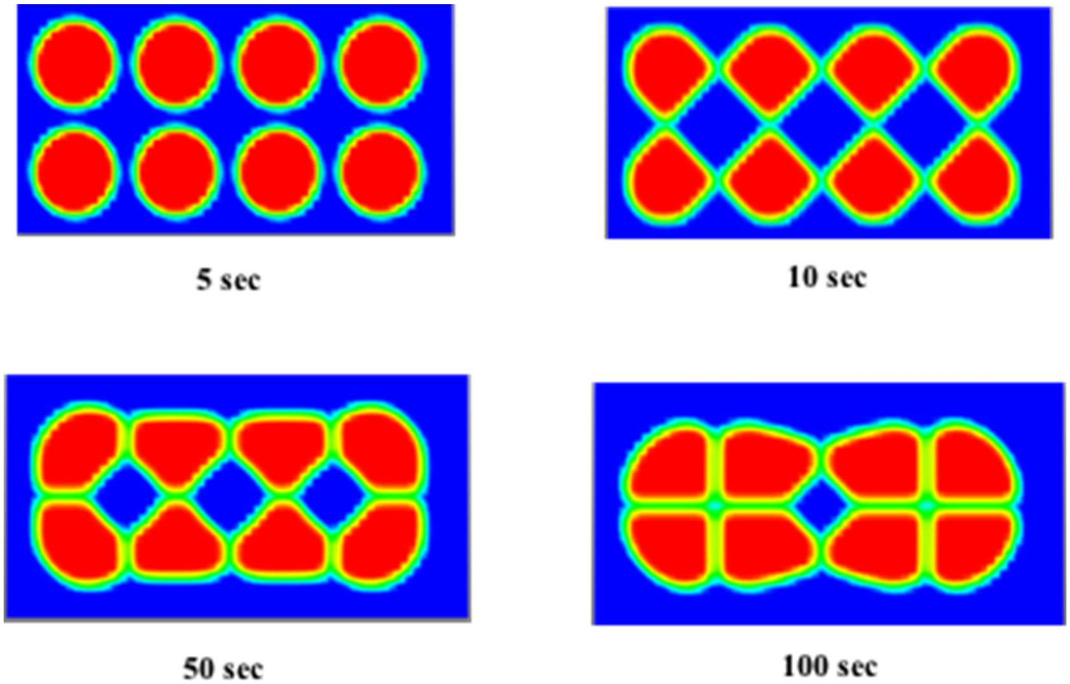

5 sec

10 sec

50 sec

100 sec

Figure IV.24 Evolution of necking microstructure with pressure in multiple particles

Simulation Units for Long Term Microstructural Evolution

While phase field models are often nondimensionalized, the inherit equations are dimensional. Thus, it is critical to understand and correctly implement the units, especially when coupling multiple physics and solving equation s for long term microstructal evolution. Unit analysis has been executed in order to relate simulation time to actual time using units as l for length, t for time, e for energy and mol for moles. The free energy equations are represented in terms of energy per molar volume (e/l^3). The co-efficient of the gradient terms are in units of energy per lattice site (e/l). Mobility connects spatial evolution to the temporal evolution of the phase field variables. The Cahn-hilliard equation takes mobility M in units of l^2mol/et and for Allen-Cahn the mobility L is in l^3/et units. By altering the mobilities and using proper time scale, we can change the simulation time units to years and thus can execute long term evolution of microstructures easily.

Simulation Tool

MOOSE (**M**ultiphysics **O**bject **O**riented **S**imulation **E**nvironment) frameworks has been leveraged for the current simulation. MOOSE is an open source codes developed by Idaho National Lab (INL). It has finite element based solver to solve partial differential equation of any kind and order. It has a libmesh sub module and uses nonlinear solvers from Petsc. It also has automatic time and mesh adaptivity. Additionally, it has inbuilt modules providing capability of phase field, solid mechanics, heat conduction etc. to name some. All these modules can be combined and run together for any specific simulation. MOOSE codes are based on C++ which can handle complicated mathematical formulations/operations. In this case we have primarily used the phase field module along with heat conduction. Since the basic equations are already modeled in MOOSE, all we needed was to model the free energy function and the material properties/characteristics corresponding to specific problem we are solving.

Plasticity Formulation

In order to incorporate plasticity along with microstructural evolution, total strain is considered to have contribution from elastic strain, eigen strain and plastic strain,

$$\varepsilon_t = \varepsilon_0 + \varepsilon_{el} + \varepsilon_p \qquad .$$

Eigen strain here is represented as,

$$\varepsilon_0 = \varepsilon_{ms} \Delta c(r) I$$

where, I is the identity matrix and ε_{ms} is the lattice mismatch co-efficient. The contribution of each strain in the free energy is discussed below.

For a material subjected to external loading elastic energy is expressed as,

$$F_{el}(\varepsilon_{el}) = -F_{ex} + \frac{1}{2}\int_V C : \varepsilon_{el} : \varepsilon_{el} dV \qquad ,$$

where, C is the elasticity moduli tensor, F_{ex} is the homogenous energy term which depends on the boundary conditions. F_{ex} is proportional to applied stress for a material subjected to uniform axial stress and zero for strain controlled boundary condition. ε_{el} is the small elastic strain generated in the material.

Rate dependent visoplastic model has been implemented along with the phase field model. Incorporation of plastic deformation enables us to consider the long term creep due to diffusion and plastic flow. Plastic energy is calculated based on two internal variables related to kinematic and isotropic hardening Moelans et al. (2008). The viscoplastic energy contribution is formulated as follows,

$$f_{vp}(\alpha,\ p) = \int_V \frac{1}{3} C\alpha : \alpha + \frac{1}{2} Hp^2 + \frac{1}{2} A \left|\nabla p\right|^2 \ dV$$

Where, *α* and *p* are the hardening parameters. The last term in above equation introduces intrinsic length scale into the plastic model.
In order to develop the flow rules, the viscoplastic potential for the rate dependent plastic model has been used Chaboche (2008).

$$\Omega = \int_V \tilde{\Omega} \left[J_2(\utilde{\sigma} - \utilde{X}) - R_0 - R + \left(\frac{D}{2C} J_2^2(\utilde{X}) - \frac{2DC}{9} J_2^2(\utilde{\alpha}) \right) \right] dV$$

Here, definition of *J₂(σ), X* & *R* are given as follows,

$$J_2(\underset{\sim}{\sigma}) = \sqrt{\frac{3}{2}\underset{\sim}{\sigma}' : \underset{\sim}{\sigma}'} with \underset{\sim}{\sigma}' = \underset{\sim}{\sigma} - \frac{1}{3}Tr(\underset{\sim}{\sigma})\underset{\sim}{I}$$

$$\underset{\sim}{X} = \frac{2}{3}C\underset{\sim}{\alpha} \text{ and } R = Hp - A\Delta p$$

Linear isotropic hardening is defined as,

$$\dot{p} = \left\langle \frac{J_2(\underset{\sim}{\sigma} - \underset{\sim}{X}) - R_0 - R}{K} \right\rangle^N ,$$

And is related to plastic strain as,

$$\dot{p} = \sqrt{\frac{2}{3}\dot{\varepsilon}_p : \dot{\varepsilon}_p}$$

P, here, represents the cumulative plastic strain or the viscoplastic strain. Plastic strain rate is estimated as,

$$\dot{\underset{\sim}{\varepsilon}}^p = \frac{3}{2}\dot{p}\frac{\underset{\sim}{\sigma} - \underset{\sim}{X}}{J_2(\underset{\sim}{\sigma} - \underset{\sim}{X})}$$

Kinematic hardening is captured by the change in the internal variables,

$$\dot{\underset{\sim}{\alpha}} = \dot{\underset{\sim}{\varepsilon}}^p - D\underset{\sim}{\alpha}\dot{p}$$

Viscoplastic energy introduces additional term to the total free energy and eventually impacts the microstructural evolution,

$$F = f_0(c, \eta_i) + f_{el}(c, \eta_i, \varepsilon_{el}) + f_{vp}(\alpha, p).$$

The elasticity tensor, yield stress, as well as the internal variables and eigen strains varies with phase concentration and the crystallographic orientation of the grains. We will be performing a detailed analysis on this formulation to obtain components of the viscoplastic energy and co-relate this to the microstructural evolution.

Particle Rigid Body Motion:

During creep deformation the whole powder particles can translate and rotate on top of each other. The rigid body motion of particles has been implemented in current model using advection velocities of individual grains. In this regard first the force density acting on each grain has been computed using,

$$dF_i = k\sum_{j \neq i}(\rho - \rho_0)\langle \eta_i \eta_j \rangle [\nabla \eta_i - \nabla \eta_j] d^3r$$

where, k is stiffness constant relating to force magnitude due to mass density variation at grain boundaries and ρ_0 is the equilibrium density. $\langle \eta_i \eta_j \rangle$ is defined as,

$$\langle \eta_i \eta_j \rangle = \begin{cases} 1, for \eta_i \eta_j \geq c_{gb} \\ 0, otherwise \end{cases}$$

c_{gb} is the threshold concentration value for grain boundaries. The force density takes care of the reaction forces between two particles as they interact with each other during the compaction process. The volumes and centers of each grain has been calculated so that the total force and torque acting on each grain can be estimated. Here grain center is the center of mass of the ith particle,

$$r_{ci} = \frac{1}{V_i}\int_V r\eta_i d^3 r \qquad \text{with} \qquad V_i = \int_V \eta_i d^3 r$$

Similarly, the forces and torques acting on the particles are calculated,

$$F_i = \int_V dF_i$$

$$T_i = \int_V [r - r_{ci}] \times dF_i$$

Finally, the grain advection velocity corresponding to each grain is calculated as,

$$v_{ti} = \frac{m_t}{V_i} F_i \eta_i$$

$$v_{ri} = \frac{m_r}{V_i} T_i \times [r - r_{ci}]\eta_i$$

$$v_{adv_i} = v_{ti} + v_{ri}$$

Advection velocity terms are used to modify the traditional phase field equations to implement rigid body motion of the particles. This model has been adopted from Wang (2006). The method of coupling rigid body motion with phase-field will be discussed in details in the following numerical implementation section.

Numerical Formulation

The kinetic equation for the spatial and temporal evolution of conserved phase field variable, *c*(**r**,t), is defined using the Cahn-Hilland (CH) equation Cahn and Hilliard (1958) as follows:

$$\frac{\partial c}{\partial t} = \nabla . \left[M_v \nabla \frac{\delta E}{\delta c} \right]$$

where $E(c)$ is the total free energy; M_{v} is the vacancy mobility which is defined as

$$M_{\mathrm{v}} = \frac{D_{\mathrm{v}} c}{k_B T},$$

where D_{v} is the vacancy diffusivity. Liu and co-workers Liu et al. (2010b) calculated the vacancy diffusivities in tungsten as a function of temperature using *ab initio* simulations. These values are used for the present phase-field study. Numerical solution of Cahn-Hilliard gives the temporal evolution of the phase-field variable which represents the phase concentration in the system. For evolution of non-conserved variable Allen-Cahn(AC) equation has been used,

$$\frac{\partial \eta}{\partial t} = -L_\eta \frac{\delta E}{\delta \eta}$$

where, L_η is the free surface mobility corresponding to voids. In order to get the plastic strain additional coupled equation needs to be solved,

$$\frac{\partial \varepsilon}{\partial t} = -L_{\varepsilon} \frac{\delta E}{\delta \varepsilon}$$

L_{ε} being the mobility corresponding to plastic strain evolution. The domain for the simulation was discretized with uniform grids, which are 256 x 256 mesh points in x and y direction, respectively. Periodic boundary conditions were imposed into the simulation domain for concentration field and order parameters. Uniaxial tensile load is applied on for the elastic and plastic energy contribution.

Numerical solution of Cahn-Hilliard gives the temporal evolution of the phase-field variable which represents the changes in phase concentration in the system. For finite element formulation, is further derived into weak forms for implementation. In order to develop the weak form, first the strong form equation is expressed in terms of all the energy contributions. AC equation can be expressed in strong form as,

$$\frac{\partial \eta_i}{\partial t} = -L\left(\frac{\delta f_0}{\delta \eta_i} + \frac{\delta f_{el}}{\delta \eta_i} + \frac{\delta f_{vp}}{\delta \eta_i} - k_{\eta_i} \nabla^2 \eta_i \right).$$

Further, the weak form is,

$$\left(\frac{\partial \eta_i}{\partial t}, \psi_m \right) = -L\left(\frac{\delta f_0}{\delta \eta_i} + \frac{\delta f_{el}}{\delta \eta_i} + \frac{\delta f_{vp}}{\delta \eta_i}, \psi_m \right) + L\left(k_{\eta_i} \nabla \eta_i, \nabla \psi_m \right) - L\left\langle k_{\eta_i} \nabla \eta_i . \vec{n}, \psi_m \right\rangle.$$

Details of the mathematical modeling and numerical scheme for solving these equation have been provided by Tonks et. al. We consider part of the microstructure as our simulation domain. The initial domain has been chosen to be 100µ m X 100 µm. Initial values of the phase filed variables are assigned as described in section 2.1 and the evolution of microstructure is studied. Periodic boundary conditions have been used for all phase field variables, i.e., for concentration field and order parameters. The displacement of the bottom edge has been constrained in the x & y direction

Preliminary Results

For the preliminary study, we have considered a bi-crystalline model having single grain boundary and constant vacancy concentration. Currently MOOSE does not have capability of incorporating plasticity and creep with phase field modelling. We are working towards extending the capability of MOOSE in order to evaluate long term microstructural evolution. Well defined initial conditions are also to be built to replicate the process conditions. This past three months we specifically added rigid body motion to MOOSE. Viscoplastic energy addition is ongoing. The key in connecting experiments with simulations based on interface diffusivity calculations connected to GB diagrams of Dr. Luo. Those calculations are also ongoing.

Grain Growth during Sintering:

The governing densification mechanism - such as diffusion, rigid body motion, grain growth - is determined by the parameters used for simulation. The co-efficients *A*, *B* and the interfacial properties play an important role in this case. Figure IV.25 shows the grain growth in case of two unequal size particles.

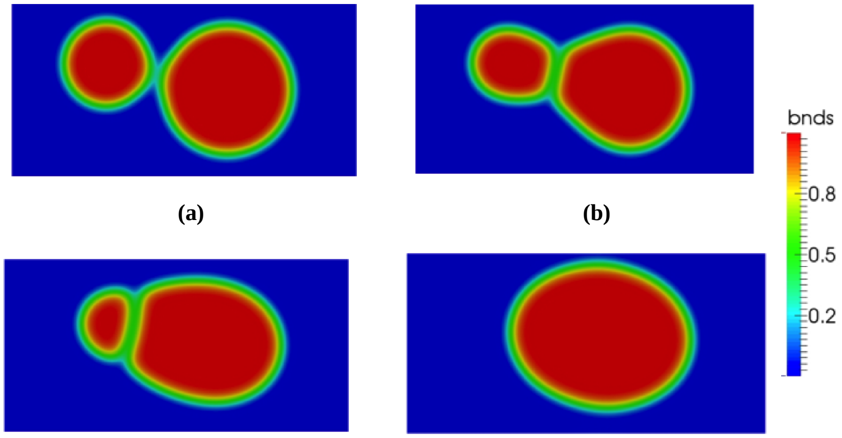

(a) (b)

(c) (d)

Figure IV.25. Grain Growth for model with two unequal size particles at a) 0 sec b) 10 sec c) 50 sec d)100 sec

Variation of average grain size is shown in Fig. (8). As observed in Fig. (8), as energy ration increases, rate of grain growth also increases. Higher grain growth rate also indicates that the densification is governed by volumetric bulk diffusion. Figure IV.26 shows grain growth as a function of energy ratio and time.

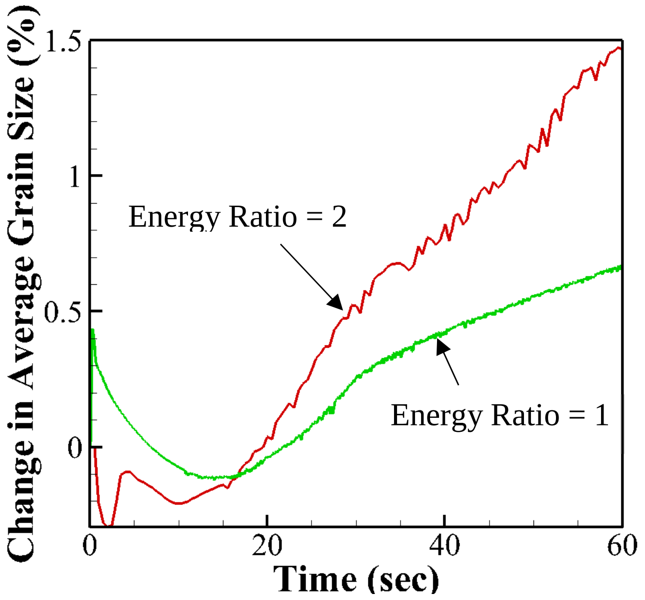

Figure IV.26. Effect of energy ratio on grain growth rate of particles during sintering

Grain growth is quantified as,

$$D^n(t) - D_0^n = kt ,$$

where, D(t) is average grain size at time t , D_0 is the average initial grain size and k is rate constant. The value of the growth exponent is dictated by the predominant diffusion mechanism. Theoretical correlation between neck growth and grain growth exponents with the densification mechanism is provided in Table 3.

Table 4. Correlation of exponents to the densification mechanisms Liu et al. (2010a)

Neck Growth Exponent	**Sintering Mechanism**	**Grain Growth Exponent**	**Sintering Mechanism**
5	Volume Diffusion	4	Volume Diffusion
6	GB Diffusion	5	GB/Surface Diffusion
7	Surface Diffusion		

For the case with energy ratio 1, the grain growth exponent was found to be 4, which indicates the dominant densification mechanism is surface diffusion. Prediction from both neck growth and grain growth examination, point to the same densification mechanism at initial stage of sintering, i.e., surface diffusion. The effect of initial grain size and grain size distribution on the overall grain growth is shown in Fig. IV.27. For the same size particles rate of increase in average grain size is higher at initial stage as compared to that of unequal size particle distribution case. However, at later stages as equilibrium is achieved grain size stabilizes. In the case of unequal particle size, larger particles absorbs the smaller one due to bulk diffusion and grain growth continues even at the later stage. Even though grain growth rate is slower, final average grain size is higher for unequal grain distribution.

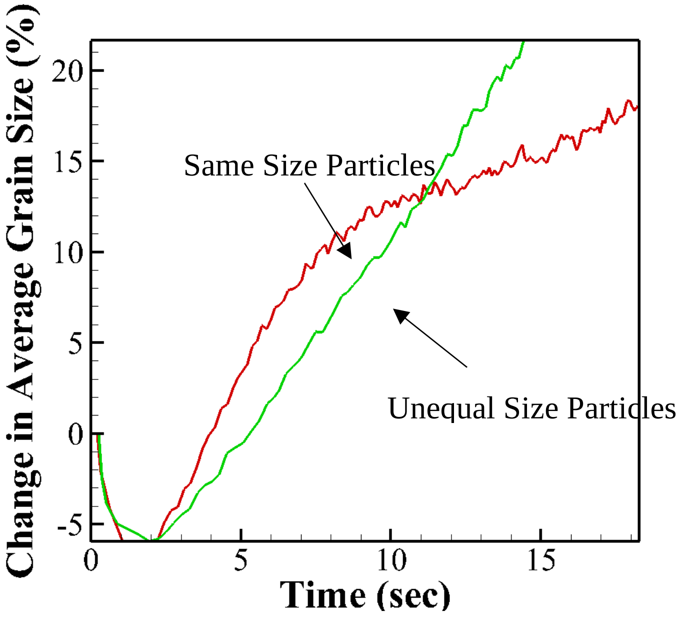

Figure IV.27. Effect of grain size distribution on the grain growth

As observed, for equal size particles, at initial stage individual grain increases in size until it reaches adjacent grains. Once grains start interacting with each other, grain boundary diffuses and the rate of grain growth reduces. In the case of unequal grain size distribution, smaller grains merge into larger grains. Therefore, some grains become larger and some grains reduce in size and eventually disappear. It order to restrain grain growth during sintering, it is advisable to use powder particles with approximately same average size. It is also observed that increasing the loading rate decreases the probability of grain growth.

Evolution of multi particle model:

Current simulations were extended further to multi particle sintering. The simulations, here, start with microstructure of a powder materials having multiple circular particles and ends with the final polycrystalline configuration of the material. The microstructural images at different time steps are presented in Fig. IV.28.

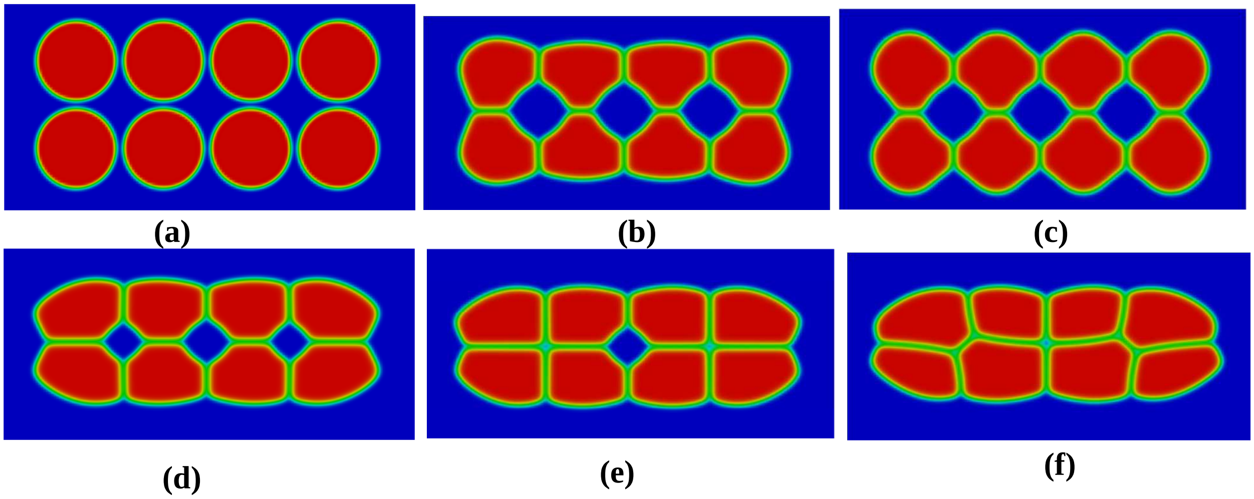

Figure IV.28. Microstructural evolution of multiparticles during sintering process at time a) 0 sec b) 2 sec c) 20 sec d) 100 sec e) 125 sec f) 156 sec

Figure IV.28 depicts the temporal evolution of particles during sintering process. The particle compaction in this case is governed by the surface and grain boundary diffusion. Porosity of the material decreases over time. The final density of the compacted structure improves with higher applied loading. For the current model, only small strain elastic deformation has been considered. Hence, particle density changes linearly over time until it reaches a maximum value. Changes in density are proportional to applied maximum pressure and deformation. Density change in this case is governed by the reduction in overall volume. This is in agreement with what Dahl Dahl et al. (2007) observed during sintering of yttria stabilized zirconium using a different sintering technique.

Microstructure Evolution Under Creep:

For preliminary studies for microstructure evolution under creep, grain boundary migration due to elastic deformation has been evaluated. Along with GB migration grain growth also takes place in the material. These two phenomenon, coupled with each other, result in a two way process impacting microstructural changes which eventually governs the deformation mechanisms and the mechanical properties of the material. Different grain orientation is considered for each grain and it is assumed that the elastic properties of the material changes with grain orientation. Fig. IV.29 shows the schematic of the models developed along with the elastic properties, loading details and boundary conditions. Structural symmetry is considered for the indentation creep analysis.

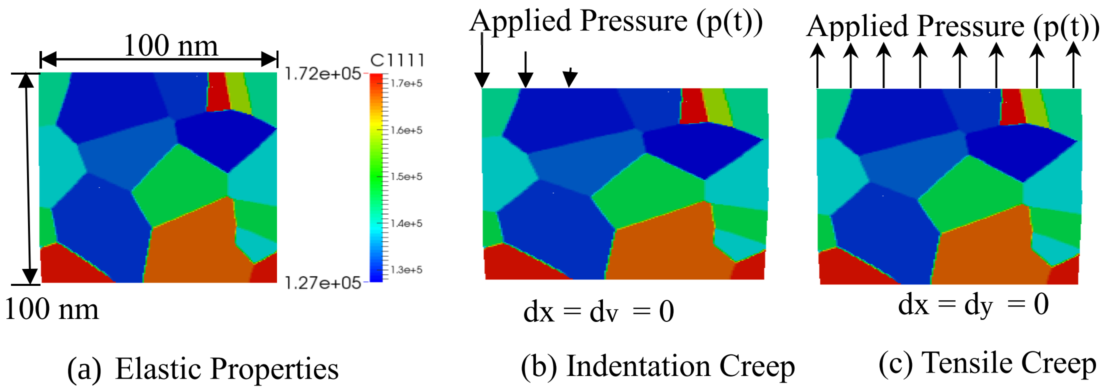

Figure IV.29 Schematic of the models with different loading conditions. (a) Elastic Constants; (b) Indentation creep; (c) Tensile creep

Figure IV.30 shows elastic stress driven grain growth over time.

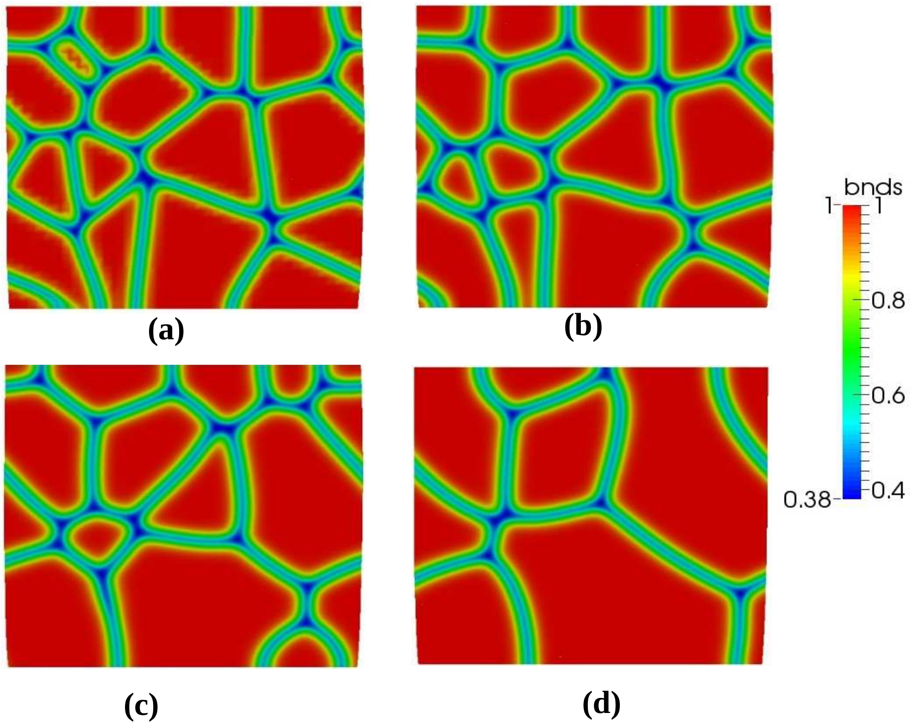

Figure IV.30. Grain growth in a polycrystalline structure at a) 0.2 sec b) 5 sec c) 25 sec d) 50 sec

It is noticed that as time progress, average grain size increases and total no. of grains decreases. Here, initially large grains absorb smaller grains and continue to grow. Grain growth in this case is dominated by the bulk and grain boundary diffusion. Figure IV.31 represents the reduction in total no. of grains over time corresponding to different interfacial width and energies.

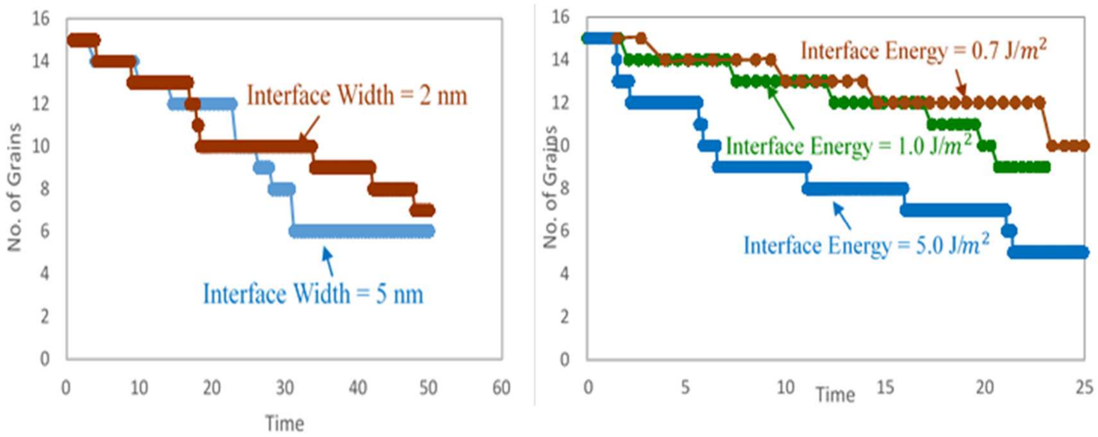

Figure IV.31. Variation of no. of grains over time for a) different interface width b) different interface energy

For initial few seconds, rate of grain growth is independent of interfacial with as well as energies. Afterwards, rate of grain growth increases with increase in interfacial width as well as interface energy over time. Time to reach final equilibrium grain configuration reduces with increase in interfacial width and energy. Further, effect of the interfacial properties on the mechanical behavior of the material has been evaluated. Figure IV.32. depicts the stress variation in the material due to microstructural changes over time.

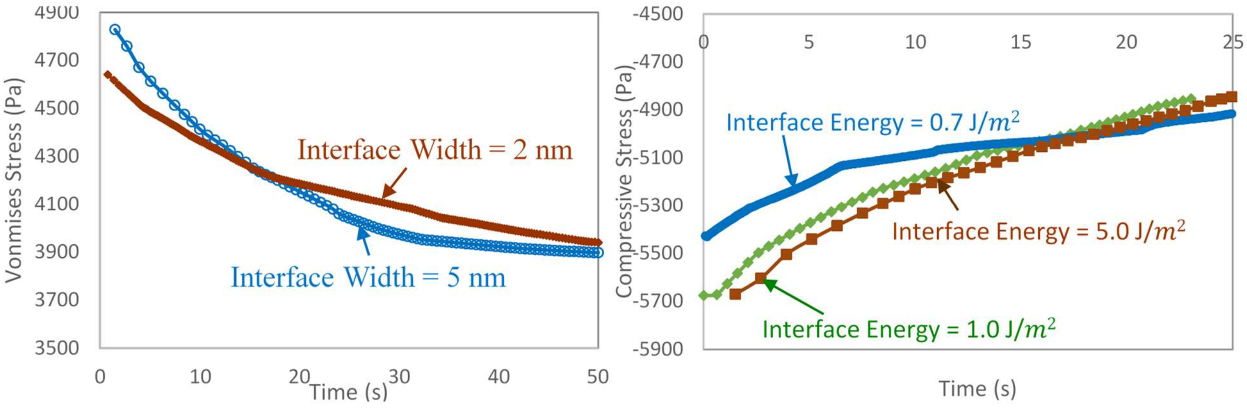

Figure IV.32. Stress Variation over time for a) different interface width b) different interface energy

Figure IV.32(a) represents the variation of average vonmises stress over time for two different interface width. Initial stress value as well as rate of reduction in average stress is higher for higher interface with. Over time as the microstructure approaches equilibrium, both cases reaches same equilibrium stress values. Figure IV.32(b) shows variation of average compressive stress over time for three different interfacial energies. Variation of stress this this case follows the same pattern as figure IV.32(a). Initial stress value and rate of change increases with increase in interfacial energy.

Eventually, as the microstructure approaches the equilibrium condition equilibrium stress value is obtained irrespective of the interface with and interface energies.

Role of Viscoplastic Deformation

For preliminary implementation the viscoplastic model has been simplified and applied to different phase field scenarios. Linear isotropic hardening with no kinematic hardening is considered for the time being. First a grain growth model with and without viscoplasticity studied for a bicrystal material. The elastic constants of the material are considered to be different on grain boundaries and inside grains. Even within grains the properties vary from grain to grain depending on the grain orientation. Figure IV.33 shows the grain orientation considered got the bi-crystal model.

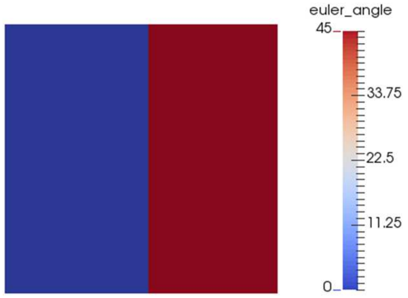

Figure IV.33. Grain orientations considered for the model

One grain with 0^o orientation and the other with 45^o orientation has been considered here. Figure IV.34 shows the grain boundary diffusion and grain growth in a bicrystalline material under elastic stress.

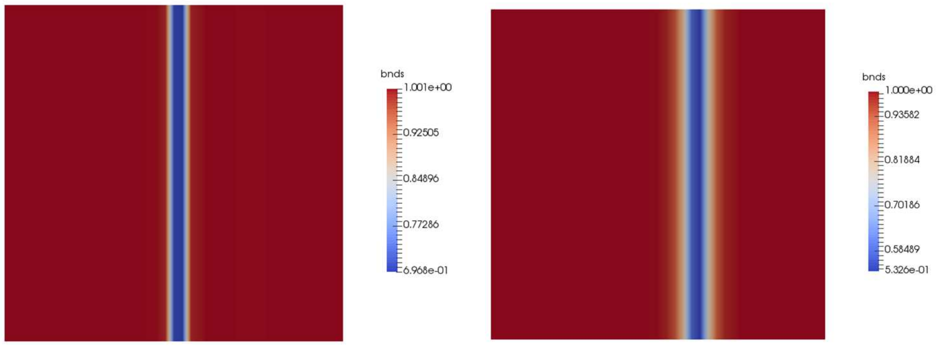

(a) (b)

Figure IV.34. Grain boundary diffusion and grain growth under elastic loading at time a) 0.02 sec b) 4 sec

The shift in grain boundary noticeable in above figure is due to growth in one grain and shrinkage in the other. Figure IV.35 shows the same model ran with rate dependent viscoplasticty and finite strain, the load is considered to be a function of time.

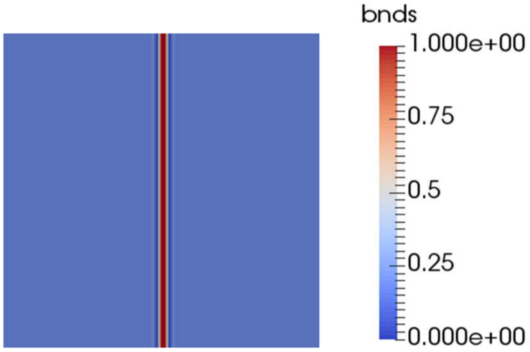

Figure IV.35. Grain boundary diffusion and grain growth under plastic loading

Grain growth is limited by plastic deformation in this case, and the phase concentration is higher near the grain boundaries. More rigorous studies are required to specifically quantify the impact of the plastic deformation on the grain growth and grain boundary diffusion. Different phase transformation models along with different loading will be developed in future to observe the impact of creep deformation on microstructural evolution.

Diffusion Creep

Next, a specific simplified case for creep is studied for diffusion driven creep. A bicrystaline structure with a tensile loading is simulated at fixed temperature of 500 K. Only grain boundary diffusion is considered in the model and no gradient energy contribution is accounted for here. The loading is proportional to time and elastic properties are considered to vary on grain boundaries. Figure IV.36a shows the initial grain boundary configuration and Figure IV.36b shows the maximum applied load at final time step of the simulation.

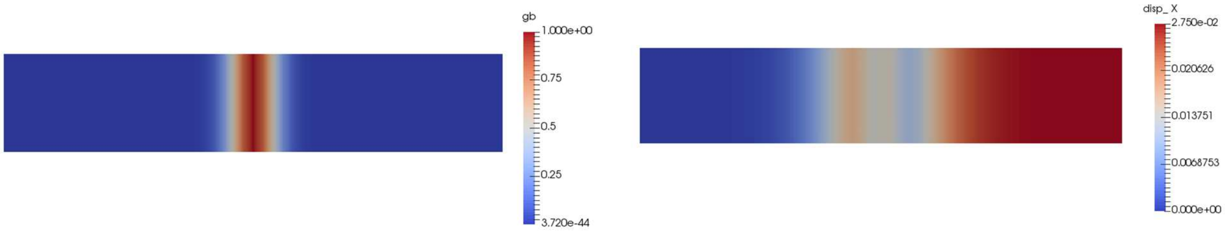

(a) (b)

Figure IV.36. a) Initial configuration with grain boundary b) Maximum displacement leading to creep deformation

Figure IV.37 represents the creep strain over the simulation domain at 10 sec and 200 sec. The creep strain are driven by the diffusion flux near the grain boundaries. Creep strain is maximum in the region adjacent to the grain boundaries due to dislocation climb.

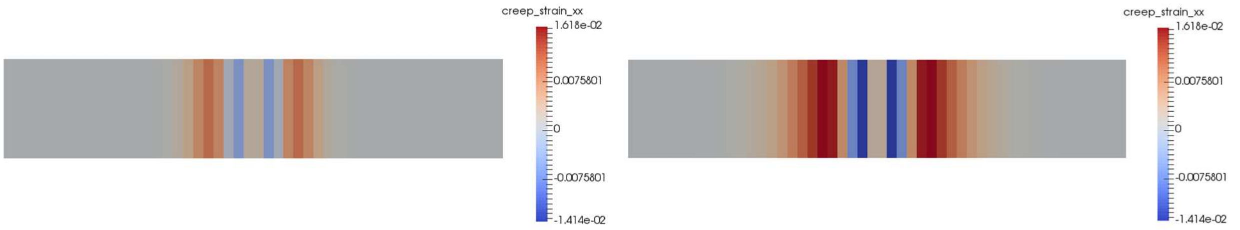

(a) (b)

Figure IV.37. Creep strain a) 10 sec b) 200 sec

Figure IV.38 shows the stress variation over the simulation time at 10 and 200 sec. The grain boundaries are the weaker spot in the microstructure and experience maximum stress. Stress reduces in side grains as the stress relaxation occurs due to accumulated creep strain adjacent to the grain boundaries.

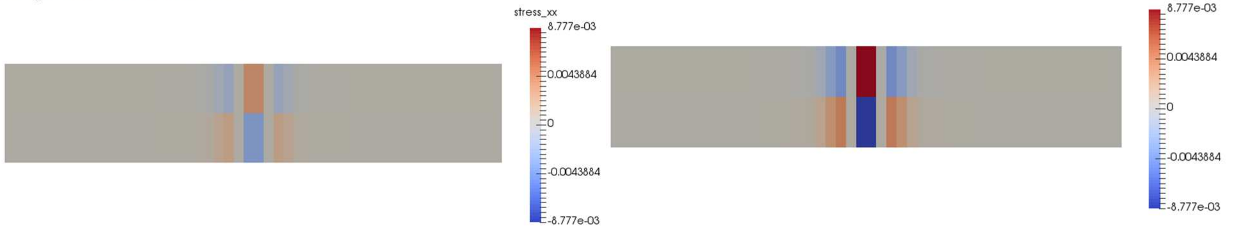

(a) (b)

Figure IV.38. Vonmises stress a) 10 sec b) 200 sec

Another diffusion creep case was considered for no external loading. In this case the deformation was driven by the eigen strain generated due to the lattice mismatch between the grains. Different grain orientation leads to generation of eigen strain near the grain boundaries. Figure IV.39 shows that eigen strain generated in x and y direction due to lattice mismatch between grains. The eigen strain here is considered to be a function of phase concentration and grain boundary here is assumed to be a different phase than the grains.

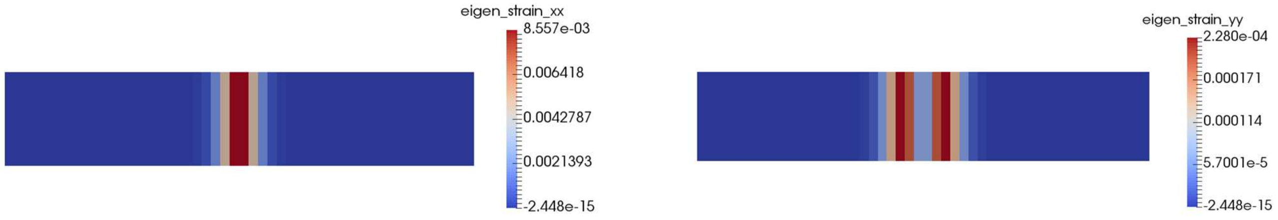

(a) (b)

Figure IV.39. Eigen strain in a) x direction b) y direction

Figure IV.40. shows the stress behavior of over at different time. The stress profile for this case is different from the earlier. The stress reduces over time due to accumulation of creep strain and stress relaxation.

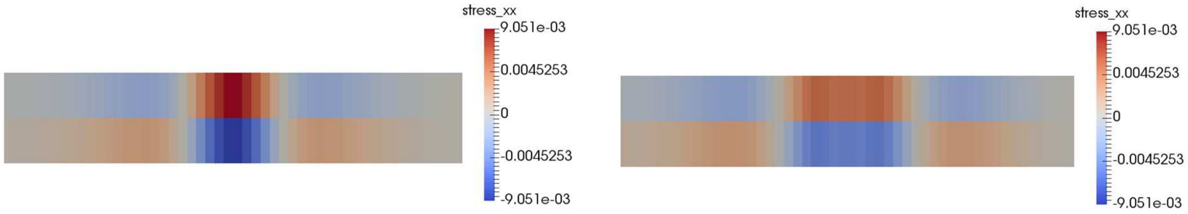

(a) (b)

Figure IV.40. Stress variation in a) x direction b) y direction

As of now only simplified model has been tested for bicrystalline structure at fixed temperature. The model will be extended to capture behavior of a polycrystalline structure under various temperatures capturing different creep mechanisms. Further effort will be put to quantify the impact of creep deformation on the microstructural evolution.

Conclusions

The key achievements and conclusions were made and listed below:

1. Pure and W-X (where X = Cu, Hf, Mn, Nb, Ni, Re, Ti, Ta and Zr) specimens with controlled microstructure have been prepared at UCSD and sent to Purdue University for initial indentation creep experiments (while further iterative optimization expected).
2. Nanocrystalline Ni foils with controlled thickness were fabricated via electro-deposition for creep tests. Nanoindentation creep tests were conducted on such samples.
3. GB energy and adsorption in W-based binary alloys were computed to show the GB segregation behavior. The computed results can also be an input to creep functions for long term microstructure creep modeling.
4. We constructed the GB λ diagram by considering the GB adsorption in disordered GB at high temperature, while we considered the GB adsorption in ordered GB at low temperature by using the Wynblatt-Chatain model in W-based binary systems;
5. We calculated the GB diffusivity map based on the computed GB λ diagram for Mo-Ni and W-Co systems. This success verifies our original correlation assumption between λ calculations and corresponding GB diffusivities.
6. We established a multiscale model that can incorporate interface structures predicted using thermodynamics into polycrystalline material failure strength prediction models.
7. We developed a phase field model that incorporates long term grain boundary diffusivity character to predict long term creep evolution as a function of microstructure.

Publications acknowledged partial support from this grant:

- N. Zhou and J. Luo, "Developing Grain Boundary Diagrams for Multicomponent Alloys," *Acta Materialia*, 91, 202-16 (2015).
- J. Luo, "A Short Review of High-Temperature Wetting and Complexion Transitions with a Critical Assessment of Their Influence on Liquid Metal Embrittlement and Corrosion," Corrosion, 72 (2015) 897-910.
- N. Zhou, T. Hu, J. Luo, "Grain Boundary Complexions in Multicomponent Alloys: Challenges and Opportunities" **(invited review)**, *Current Opinion in Solid State and Materials Science*, in press (2016).
- M. Tang and J. Luo, "Interface Science and the Formation of Structure," a book chapter for Data Analytics for Materials Characterization, ed. J. Simmons, M. De Graef, L. Drummy, and C. Bouman, accepted
- Lee, H., and Tomar, V., 2014, Understanding the influence of grain boundary thickness variation on the mechanical strength of a nickel-doped tungsten grain boundary, International Journal of Plasticity, Volume 53, pages 135-147.
- Biswas, S., Schwen, D., Singh, J., and Tomar, V., 2016, A Study of the evolution of microstructure and consolidation kinetics during field assisted sintering using a phase field modeling based approach, Extreme Mechanics Letters, Volume 7, June 2016, Pages 78–89.

III. Graphical Materials List

Figure III-1: Schematic illustration of the proposed thermodynamic model.

Figure III-2: (A) Computed GB λ-diagram *vs.* **(B)** measured GB diffusivity map for Ni-doped Mo [reprinted from Shi and Luo (2011)].

Figure III-3: Computed grain boundary energy *vs.* Co concentration for W-Co alloys at 973 K.

Figure III-4: Computed grain boundary energy *vs.* the solute concentration curves for W-*X* alloys (*X* = Zr, Cr, and Fe) at 973 K. The solid solubility limits (X_S) are also labeled.

Figure III-5: Computed elastic energy for different elements doped in W bcc phase.

Figure III-6: Computed bonding energy difference between different elements and W at pure bcc solid state.

Figure III-7: Computed GB energy and GB absorption of Co-doped W alloy at three different temperatures. Solid curves are results within the solidus compositions (marked by hollow dots) beyond which the bulk phase is supersaturated. The bulk phase diagram is plotted to show the calculated region.

Figure III-8: Computed GB energy and GB absorption of Zr-doped W alloy at three different temperatures. Solid curves are results within the solidus compositions (marked by hollow dots) beyond which the bulk phase is supersaturated. The bulk phase diagram is plotted to show the calculated region.

Figure III-9: Computed GB energy and GB absorption of Cr-doped W alloy at three different temperatures. Solid curves are results within the solidus compositions (marked by hollow dots) beyond which the bulk phase is supersaturated. The bulk phase diagram is plotted to show the calculated region.

Figure III-10: Computed GB energy and GB absorption of Fe-doped W alloy at three different temperatures. Solid curves are results within the solidus compositions (marked by hollow dots) beyond which the bulk phase is supersaturated. The bulk phase diagram is plotted to show the calculated region.

Figure III-11: Computed GB "phase" diagram using the Wynblatt-Chatain model with **(A)** only BCC phase and **(B)** both BCC phase and secondary bulk ZrW phase (as precipitation) for the Zr-doped W binary system.

Figure III-12: Computed GB "phase" diagrams of W-Cr system by using the **(A1)** λ diagram and **(A2)** Wynblatt-Chatain model; W-Fe system by using the **(B1)** λ diagram and **(B2)** Wynblatt-Chatain model

Figure III-13: Schematic illustration of proposed work of constructing GB diffusivity map via extrapolation and informatics methods that are in progress

Figure III-14: Computed λ values *vs.* measured GB diffusivities for the Mo-Ni system

Figure III-15: Mo-Ni system **(A)** computed GB λ diagram, **(B)** calculated GB diffusivity map and **(C)** measured GB diffusivity map.

Figure III-16: W-Co system **(A)** computed GB λ diagram, **(B)** calculated GB diffusivity map

Fig. IV.1: A pictorial representation of the multiscale modeling approach

Fig. IV.2: Construction process of W-Ni alloy GB structure (a) HRTEM image, Gupta et al. (2007a), of W-Ni GB (b) atomic structure (c) 2-D dimension of interface, and (d) 3-D interface structure with boundary condition

Fig. IV.3: Crack tip position as a function of loading increment for (a) GB thickness of 2nm, (b) GB thickness of 4nm, and (c) GB thickness of 8nm

Fig. IV.4: Effect of GB thickness to the (a) crack tip position and (b) strain energy release with respect to the time-step increment

Fig. IV.5: Length-scale effects to (a) the total energy by the volume and (b) the strain energy by the volume of the 3-D model

Fig. IV.6: Effect of Ni percentage to the (a) crack tip position and (b) damage dissipation energy with respect to the time-step increment

Fig. IV.7: Stress intensity factor verses crack position as a function of (a) GB thickness and (b) Ni percentage

Fig. IV.8: Fracture toughness with respect to GB thickness and Ni percentage in (a) the initial crack propagation (60nm x 50nm scale), (b) within the GB region (60nm x 50nm scale), (c) the initial crack propagation (6000nm x 5000nm scale), and (d) within the GB region (6000nm x 5000nm scale)

Fig. IV.9: (a) Fracture toughness of 6000nm x 5000nm scale with respect to Ni percentage as a function of GB thickness, and (b) comparison of fracture toughness of W and W alloy material, Gludovatz et al. (2010), with presented result

Figure IV.20 Brittleness index of simulations with respect to the Ni percentage for (a) GB thickness of 2nm, (b) GB thickness of 4nm, (c) GB thickness of 8nm in 60nm x 50nm dimension, (d) GB thickness of 2nm, (e) GB thickness of 4nm, (f) GB thickness of 8nm in 600nm x 500nm dimension, (g) GB thickness of 2nm, (h) GB thickness of 4nm, and (i) GB thickness of 8nm in 6000nm x 5000nm dimension

Figure IV.11 (a) Length-scale effect on the brittleness index and the estimation, and (b) revised brittleness index as a function of length-scale

Figure IV.12 Comparison of the revised brittleness index for different types of GB as a function of Ni percentage

Figure IV.13 Effect of microstructure morphology to the brittleness index

Figure IV.14 (a) Failure index as a function of GB angle and maximum tensile strength, (b) prediction criteria derived from the developed relation

Figure IV.15 Crack propagation path as a function of the maximum tensile strength when (a) T = 3500 MPa, (b) T = 3700MPa, (c) T = 4100MPa, and (d) T = 4200MPa

Figure IV.16 Dissipation of (a) plastic energy and (b) internal energy for microstructure fracture with different GBs

Figure IV.17 Comparison of crack path in polycrystalline W with the predicted crack path from failure index for different morphologies (a), (b), and (c). (d) Actual crack propagation image from experiment, Pędzich (2012)

FigureIV.18. Chemical Free Energy (at T = 1000 C) for the Simulation.

The effect of temperature on the free energy has also been shown separately in Fig. IV.19.

Figure IV.19. Effect of temperature on Chemical Free Energy

FigureIV.20. Initial Conditions a) Circular particles in 2D b) Multiple particles in 3D

FigureIV.21. Evolution of necking microstructure without pressure in two particles

Figure IV.22 Change in particle volume fraction with time

Figure IV.23 Evolution of necking microstructure with pressure in two particles

Figure IV.24 Evolution of necking microstructure with pressure in multiple particles

Figure IV.25. Grain Growth for model with two unequal size particles at a) 0 sec b) 10 sec c) 50 sec d)100 sec

Figure IV.26. Effect of energy ratio on grain growth rate of particles during sintering

Figure IV.27. Effect of grain size distribution on the grain growth

Figure IV.28. Microstructural evolution of multiparticles during sintering process at time a) 0 sec b) 2 sec c) 20 sec d) 100 sec e) 125 sec f) 156 sec

Figure IV.29 Schematic of the models with different loading conditions. (a) Elastic Constants; (b) Indentation creep; (c) Tensile creep

Figure IV.30. Grain growth in a polycrystalline structure at a) 0.2 sec b) 5 sec c) 25 sec d) 50 sec

Figure IV.31. Variation of no. of grains over time for a) different interface width b) different interface energy

Figure IV.32. Stress Variation over time for a) different interface width b) different interface energy

Figure IV.33. Grain orientations considered for the model

Figure IV.34. Grain boundary diffusion and grain growth under elastic loading at time

b) 0.02 sec b) 4 sec

Figure IV.35. Grain boundary diffusion and grain growth under plastic loading

Figure IV.36. a) Initial configuration with grain boundary b) Maximum displacement leading to creep deformation

Figure IV.37. Creep strain a) 10 sec b) 200 sec

Figure IV.38. Von Mises stress a) 10 sec b) 200 sec

Figure IV.39. Eigen strain in a) x direction b) y direction

Figure IV.40. Stress variation in a) x direction b) y direction

IV. REFERENCES:

Cahn, J. W. and Hilliard, J. E. (1958). "Free Energy of a Nonuniform System. I. Interfacial Free Energy." The Journal of Chemical Physics **28**(2): 258-267.

Catellani, A., Galli, G. and Gygi, F. (1996). "Reconstruction and thermal stability of the cubic SiC (001) surfaces." Phys. Rev. Lett. **77**: 5090-5093.

Chaboche, J. L. (2008). "A review of some plasticity and viscoplasticity constitutive theories." International Journal of Plasticity **24**(10): 1642-1693.

Chatterjee, A. and Vlachos, D. G. (2007). "An overview of spatial microscopic and accelerated kinetic Monte Carlo methods." J. Computer-Aided Mater. Des. **14**: 253-308.

Clarke, A. S. and Jo´ nsson, H. (1993). "Structural changes accompanying densification of random-sphere packings." Phys. Rev. E **47**: 3975–3984.

Dahl, P., Kaus, I., Zhao, Z., Johnsson, M., Nygren, M., Wiik, K., Grande, T. and Einarsrud, M. A. (2007). "Densification and properties of zirconia prepared by three different sintering techniques." Ceramics International **33**(8): 1603-1610.

Deng, J. (2012). "A Phase Field Model of Sintering with Direction-Dependent Diffusion." MATERIALS TRANSACTIONS **53**(2): 385-389.

Elsherik, A. M. and Erb, U. (1995). "SYNTHESIS OF BULK NANOCRYSTALLINE NICKEL BY PULSED ELECTRODEPOSITION." Journal of Materials Science **30**(22): 5743-5749.

Furukawa, S.-i. and Nitta, T. (2000). "Non-equilibrium molecular dynamics simulation studies on gas permeation across carbon membranes with different pore shape composed of micro-graphite crystallites." J. Membrane Sci. **178**(1-2): 107-119.

Gan, M. and Tomar, V. (2010). "Temperature dependent multiscale creep strength of a class of polymer derived Si-C-O ceramics." Acta Materialia (submitted).

Gillespie, D. T. (1977). "Exact stochastic simulation of coupled chemical reactions." J. Phys. Chem. **81**: 2340-2361.

Gillespie, D. T. (2007). "Stochastic simulation of chemical kinetics." Annu. Rev. Phys. Chem. **58**(35-55).

Gludovatz, B., Wurster, S., Hoffmann, A. and Pippan, R. (2010). "Fracture toughness of polycrystalline tungsten alloys." International Journal of Refractory Metals and Hard Materials **28**(6): 674-678.

Gupta, V. K., Yoon, D.-H., Meyer Iii, H. M. and Luo, J. (2007a). "Thin intergranular films and solid-state activated sintering in nickel-doped tungsten." Acta Materialia **55**(9): 3131-3142.

Gupta, V. K., Yoon, D. H., Meyer, H. M. and Luo, J. (2007b). "Thin intergranular films and solid-state activated sintering in nickel-doped tungsten." Acta Materialia **55**(9): 3131-3142.

Hu, S. Y. and Henager Jr, C. H. (2010). "Phase-field simulation of void migration in a temperature gradient." Acta Materialia **58**(9): 3230-3237.

Lawn, B. R. and Marshall, D. B. (1979). "Hardness, Toughness, and Brittleness: An Indentation Analysis." Journal of the American Ceramic Society **62**(7-8): 347-350.

Lee, H. and Tomar, V. (2014). "Understanding the influence of grain boundary thickness variation on the mechanical strength of a nickel-doped tungsten grain boundary." International Journal of Plasticity **53**: 135-147.

Li, H., Cao, Y., Petzold, L. R. and Gillespie, D. T. (2008). "Algorithms and software for stochastic simulation of biochemical reacting systems." Biotechnol Prog. **24**(1): 56-61.

Li, H. and Ngan, A. H. W. (2004). "Size effect of nanoindentation creep." J. Mater. Res. **19**(2):

513-522.

Li, Y., Pang, Y., Wu, X. and Liu, W. (2014). "Effects of temperature gradient and elastic strain on spinodal decomposition and microstructure evolution of binary alloys." Modelling and Simulation in Materials Science and Engineering **22**(3): 035009.

Liu, L. L., Gao, F., Li, B. and Hu, G. X. (2010a). "Phase-Field Simulation of Process in Sintering Ceramics." Advanced Materials Research **154-155**: 1674-1679.

Liu, Y.-L., Zhou, H.-B., Jin, S., Zhang, Y. and Lu, G.-H. (2010b). "Dissolution and diffusion properties of carbon in tungsten." Journal of Physics: Condensed Matter **22**(44): 445504.

Luo, J. and Shi, X. M. (2008). "Grain boundary disordering in binary alloys." Applied Physics Letters **92**(10).

Mei, D., Sheth, P. A., Neurock, M. and Smitch, M. C. (2006). "First-principles-based kinetic Monte Carlo simulation of the selective hydrogenation of acetylene over Pd(111)." J. Catalysis **242**(1): 1-15.

Milhans, J., Khaleel, M., Sun, X., Tehranic, M., Al-Haikc, M. and Garmestani, H. (2010). "Creep properties of solid oxide fuel cell glass–ceramic seal G18." J. Power Sources **195**: 3631-3635.

Moelans, N., Blanpain, B. and Wollants, P. (2008). "An introduction to phase-field modeling of microstructure evolution." Calphad **32**(2): 268-294.

Pędzich, Z. (2012). "Tungsten Carbide as an Reinforcement in Structural Oxide-Matrix Composites."

Shi, X. and Luo, J. (2011). "Developing grain boundary diagrams as a materials science tool: A case study of nickel-doped molybdenum." Physical Review B **84**(1): 014105.

Shi, X. M. and Luo, J. (2009). "Grain boundary wetting and prewetting in Ni-doped Mo." Applied Physics Letters **94**(25).

Tomar, V. (2007). Multiscale simulation of dynamic fracture in polycrystalline SiC-Si_3N_4 using a molecularly motivated cohesive finite element method. 48th AIAA/ASME/ASCE/AHS/ASC Structures, Structural Dynamics, and Materials Conference (April 23-26, 2007) Honolulu, Hawaii, Paper No. AIAA-2007-2345.

Tomar, V. (2008a). "Analyses of the role of grain boundaries in mesoscale dynamic fracture resistance of SiC-Si_3N_4 intergranular nanocomposites." Eng. Fract. Mech. **75**: 4501-4512.

Tomar, V. (2008b). "Analyses of the role of the second phase SiC particles in microstructure dependent fracture resistance variation of SiC-Si_3N_4 nanocomposites." Modelling Simul. Mater. Sci. Eng. **16**: 035001.

Tomar, V. (2008c). "Modeling of dynamic fracture and damage in 2-Dimensional trabecular bone microstructures using the cohesive finite element method." J. Biomech. Engg. **130**(2): 021021.

Tomar, V., Zhai, J. and Zhou, M. (2004). "Bounds for element size in a variable stiffness cohesive finite element model." Int. J. Num. Meth. Engg. **61**: 1894-1920.

Tomar, V. and Zhou, M. (2005). "Deterministic and stochastic analyses of dynamic fracture in two-phase ceramic microstructures with random material properties." Eng. Fract. Mech. **72**: 1920-1941.

Tomar, V. and Zhou, M. (2006). "Tension-compression strength asymmetry of nanocrystalline α-Fe_2O_3+*fcc*-Al ceramic-metal composites." Appl. Phys. Lett. **88**: 233107 (233101-233103).

Tomar, V. and Zhou, M. (2007). "Analyses of tensile deformation of nanocrystalline α-Fe_2O_3+*fcc*-

Al composites using classical molecular dynamics." J. Mech. Phys. Solids **55** 1053-1085.

Tsai, P.-C. and Fang, T.-H. (2007). "A molecular dynamics study of the nucleation, thermal stability and nanomechanics of carbon nanocones." Nanotechnology **18**: 105702.

Voter, A. F. (2007). Introduction to the kinetic Monte Carlo method. Radiation Effects in Solids-Chapter 1. K. E. Sickafus, E. A. Kotomin and B. P. Uberuaga, Springer, Berlin.

Wang, Y. U. (2006). "Computer modeling and simulation of solid-state sintering: A phase field approach." Acta Materialia **54**(4): 953-961.

Wynblatt, P. and Chatain, D. (2006). "Anisotropy of segregation at grain boundaries and surfaces." Metallurgical and Materials Transactions a-Physical Metallurgy and Materials Science **37A**(9): 2595-2620.

Zhai, J., Tomar, V. and Zhou, M. (2004). "Micromechanical modeling of dynamic fracture using the cohesive finite element method." J. Engg. Mat. Tech. **126**: 179-191.

V. List of Acronyms and Abbreviations

AES: Auger Electron Spectroscopy

CALPHAD: Calculation of Phase Diagram

FIB: Focused ion beam

GB: Grain Boundary

HRTEM: High-Resolution Transmission Electron Microscopy

SEM: Scanning electron microscopy

SPS: Spark plasma sintering

TEM: Transmission Electron Microscopy

XRD: X-ray diffraction

PFM: Phase Field Modeling

FEM: Finite element Modeling